Jet quenching in heavy-ion collisions at LHC with CMS detector

by

Yetkin Yilmaz

Submitted to the Department of Physics
in partial fulfillment of the requirements for the degree of

Doctor of Philosophy

at the

MASSACHUSETTS INSTITUTE OF TECHNOLOGY

April 2013
[JUNE 2013]

Author .....
Department of Physics
March 12, 2013

Certified by .....
Prof. Dr. Gunther M. Roland
Professor
Thesis Supervisor

Accepted by .....
Prof. Dr. John Belcher
Associate Department Head

Jet quenching in heavy-ion collisions at LHC with CMS detector

by

Yetkin Yilmaz

Submitted to the Department of Physics
on March 12, 2013, in partial fulfillment of the
requirements for the degree of
Doctor of Philosophy

Abstract

The collision of highly relativistic nuclei can produce a volume of high energy density which can be used to learn about the behavior of quantum chromodynamics (QCD) at extreme conditions, such as those of the universe at times before and during the formation of hadrons out of quarks and gluons. This thesis presents experimental studies of jet-quenching phenomena in PbPb collisions at $\sqrt{s_{NN}} = 2.76$ TeV, with a focus on the study of the energy-loss, namely the analysis of correlations of jet pairs as measured by the CMS detector at LHC. The implications of the results are discussed by comparison of simple models with data. It is observed that the geometrical configuration of the dijets and the nuclear collision region plays an important role in the correlations between the jets, and the set of CMS results reviewed can illustrate the dependence of the amount of lost energy on the length of the traversed medium.

Thesis Supervisor: Prof. Dr. Gunther M. Roland
Title: Professor

Acknowledgements

I have grown up to pursue a passion for knowledge, only because I had the freedom to maintain an open mind through my childhood and later. This was made possible with a progressive manner of my parents, the way they raised me bold enough to choose a career path that doesn't offer much of material fortune, but rather a wealth of meaning. I owe my existence, not merely my physical presence in the world, but the originality of my soul, to their support.

In the end of a long education, I don't know if I count as a good experimental physicist, but if I do, that's mostly because I ended up working with a clearly exceptional one. I cannot list all the individual items that I have learned by working with Gunther (which would be a good "guide to the experimental scientist" textbook itself), however; in essence, Gunther has taught us how not to easily believe in results that we wish to believe. In particular, I learned how to ask questions and let the questions motivate the course of the study, and always trust real plots rather than vague words.

Of course we did all of the work as a team. This team involved many skilled people. I really appreciated the organizational structure of our group, in which everybody did their best to help everyone. Constantin Loizides was one of the people who watched over my practical education very closely, and thanks to him I found the software challenges of the experimental work to be a bonus in the motivation for the whole job. I am lucky to work with Yen-Jie Lee, who has been a great inspiration. Wit Busza was always there for advice in things that are far beyond the microscopic scope of the daily work, and he kept on ringing the bells when it's time to remember to step back and gaze the picture from the wide perspective. I also enjoyed being his teaching assistant for a semester, mostly because this gave me a good excuse to listen to the wonderful lectures he gave.

We all benefited from the strong team spirit in our group, and went through tough times with mutual support. At times I found it hard to pull myself together, Frank was always there to share his energy with me to create hope for the step forward. With

this team of diverse and motivated people, the winter data-taking ritual eventually became a physics fest.

My friend Erdo was my biggest support in my times in Geneva. Erdo is someone who knows how to face any difficulty in a smart way with a calm spirit, and I could rely on his help whenever I found myself in trouble. If he were a physicist among us at CERN, I am sure he would be of a leading role in the experiment, inspiring others with his will for problem-solving.

At any challenge I have faced, my beloved Melike always gave me the courage, to finish what I start, give myself a chance to succeed. This certainly lead to various achievements, such as the document you are reading. If my supervisors have observed any step-function in my performance with time, that was most likely the time she came into my life.

Finally, I thank all the readers for their interest in this document, some of whom will make studies that turn this thesis obsolete, with many exciting observations the hadron collisions are yet to offer us...

Contents

List of Figures

List of Tables

Chapter 1

Introduction

LHC provides collisions of ions that acquire more energy than ever studied. Results from earlier experiments, of which Relativistic Heavy Ion Collider (RHIC) operating at 200 GeV per nucleon pair had the highest energy, suggest the existence of a new form of matter in collisions of high energy nuclei. At the LHC energies which are more than 10 times higher in energy, while the medium may get more interesting, the tools to study also get stronger. LHC produces a high rate of hard (high transverse-momentum, p_{T}) collisions. Such collisions can provide very clean signals that can probe the behavior of the medium. Dijet events in particular, appear in abundance in collisions at LHC. As a result, the picture inferred by these probes gets a lot clearer.

In the earlier studies of high energy nuclear collisions [9, 10, 11, 12], the energy loss phenomenon was observed via the suppression in the high-p_{T} charged hadron cross-section and the disappearance of the away-side peak in the dihadron azimuthal correlations.

While the hadron-level measurements, on a statistical basis, provide evidence of the phenomena in the dense high temperature medium, a more direct observation can be performed by detecting fully reconstructed jets. In the first PbPb run of LHC in 2010, one of the striking observations was the clear abundance of events in which the transverse momenta of jets were very different, with an example in figure 1-1.

Correlations of back-to-back high-p_{T} dijets provide a collision-by-collision identifiable perspective on the energy-loss effects. The procedure involves tagging events

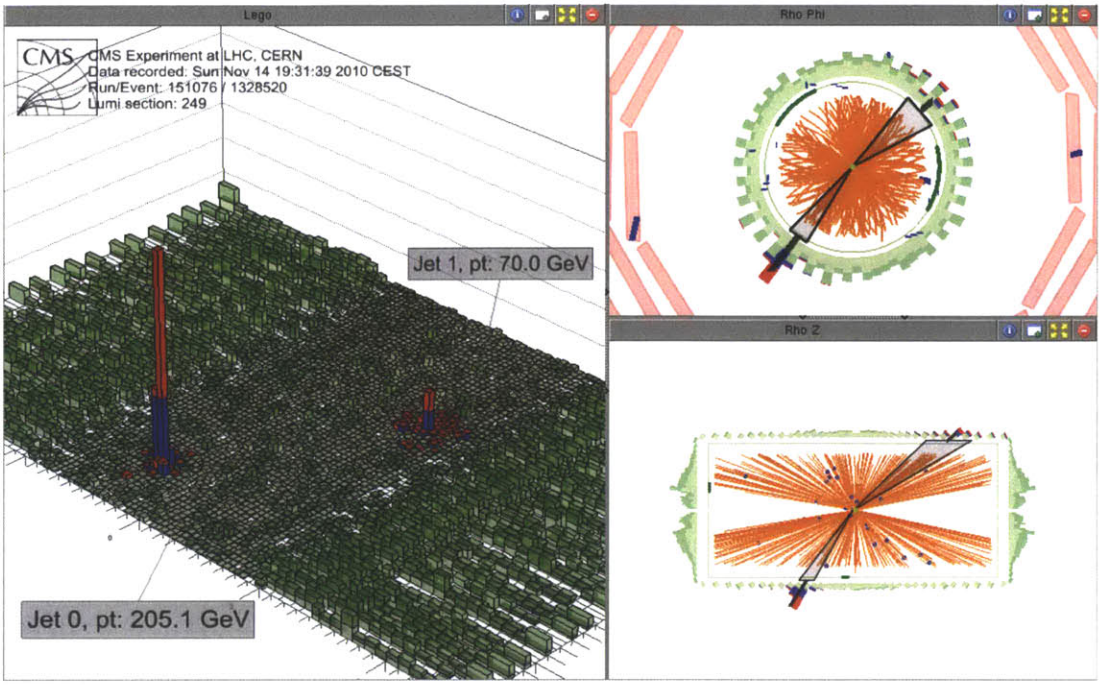

Figure 1-1: Display of a dijet event from the 2010 PbPb run of LHC, recorded by CMS.

with a high-p_{T} jet, and examining the presence or absence of a second jet, its p_{T} and the angular configuration with respect to the first jet. The approach has two important advantages: it does not rely on the exact cross-section (which has uncertainties from the structure of nucleons) and it can quantify the energy loss in event-by-event basis.

The first dijet measurements from the LHC experiments [13, 14, 15, 16, 17] revealed many aspects of the energy loss in medium. There was an enhanced momentum imbalance between the jets, without a significant change in the angular correlation. The jets appeared to be fragmenting the same way as in pp collisions, after having lost energy in the medium [6].

After the initial observations, an interesting questions arises: How does the energy loss depend on the energy of the projectile? This would tell us something about the medium properties, as does the Bethe-Bloch curve when we discuss "daily matter". We do not know the energy of the initial parton in any dijet, however if we vary the thresholds of the selection, we would be indirectly sampling different initial parton

energies. With this attitude we analyzed the dijet p_{T} imbalance with varying leading jet p_{T}. Comparing to the reference, we have observed enhanced imbalance in all leading jet p_{T} bins.

Although the statement on the existence of the energy loss at all p_{T} values is easy based on the experimental results, the exact p_{T}-dependence of the effect is difficult to deduce since the different resolution at different p_{T} can influence the appearance of the underlying energy loss distribution. In addition, the leading jet that is employed to tag the parton information of the events does not precisely represent the actual parton because it may have suffered energy loss by an unknown amount itself. To unfold the effects of the resolution, and of the unknown energy loss in the leading jet, one has to model the energy loss and check for the same p_{T} dependence. This is done for simple models of energy loss and collision geometry. It is observed the the energy loss is likely to have a very weak p_{T} dependence and geometrical configuration of the initial state plays an important role in the imbalance of the dijets.

1.1 Thesis chapters

This thesis discusses the measurement of the dijet imbalance and its implications on the medium induced energy loss. In this chapter, the physics of heavy-ion collisions and key concepts in jet quenching will be introduced.

The discussion will later proceed to the experimental method in chapters 2-5, first describing the CMS detector features. Then the reconstruction methods for the physics objects of interest, namely the jets and hadrons, are explained. The performance of these algorithms, particularly in relation to their effects on the measurement, are examined. The methods for centrality determination and estimation of initial state properties are very important for this study, therefore are discussed in detail.

Chapter 6 describes the analyses and the observations in the 2011 LHC data, focusing on the dijet imbalance studies. The jet R_{AA} and fragmentation studies are also important for the discussion, therefore they are also briefly explained.

Chapter 7 opens the discussion for the interpretations of the results obtained. The comparison of models with very simple assumptions to data are illustrated, emphasizing the need for realistic initial state calculation and consideration of experimental effects. Within the models tested, it is observed that the results are consistent with an energy-loss models that rely on geometrical configurations of medium in the initial state. The conclusions are briefly summarized in chapter 8.

In order to keep the coherence of the discussion in the main body, some supplementary information on QCD theory and simulation methods take place in the appendices.

1.2 QCD in hadron collisions

Quantum chromodynamics, or QCD for short, is the theory that describes the interactions of quarks and gluons, through the strong force. The interactions are described with a Lagrangian of SU(3) symmetry, where the gauge field couples to itself, which allows gluon-to-gluon vertices. The peculiar structure of this Lagrangian yields interesting features, which will be the topic of discussion in the following sections.

1.2.1 Confinement and asymptotic freedom

Baryonic matter is made out of quarks and gluons, which are point-like particles (at least down to very small scales). Quarks are, in fact, stable particles (except the heavy ones), yet we can never speak of a "single quark" interacting with our detector. This would be the case even if we had detectors in so small size that would be able to detect other unstable bosons. This is because the strong force gets stronger in large distances, and at the length scales in question, in fact even in smaller scales ($\tilde{\text{fm}}$) the energy stored in the QCD interaction easily excites the vacuum quark-antiquark pairs and turns any free quark into a hadron.

QCD Lagrangian involves terms of gluon coupling to itself, which resembles one very distinct feature of strong interactions. In the perturbative approach, an interaction involves infinite diagrams with additional gluon-to-gluon couplings, which are not

present, for example, photons of QED. The infinity in the diagrams, also referred to as *ultra-violet divergence*, are separated out of perturbative calculation by treating them in the coupling term and calculate interactions only up to a certain scale in momentum transfer, in the procedure called *renormalization*. This scale also translates to distance scales, where a certain small length scale is treated as a factor in coupling, α_s. When the scale dependence of α_s is examined, as can be seen in figure 1-2, the coupling increases with larger length scales, and converges to zero in small length scales. This property of QCD interactions is called *asymptotic freedom* [18]. Very high energy parton collisions can probe this relatively weakly coupled region, which correspond to perturbative QCD.

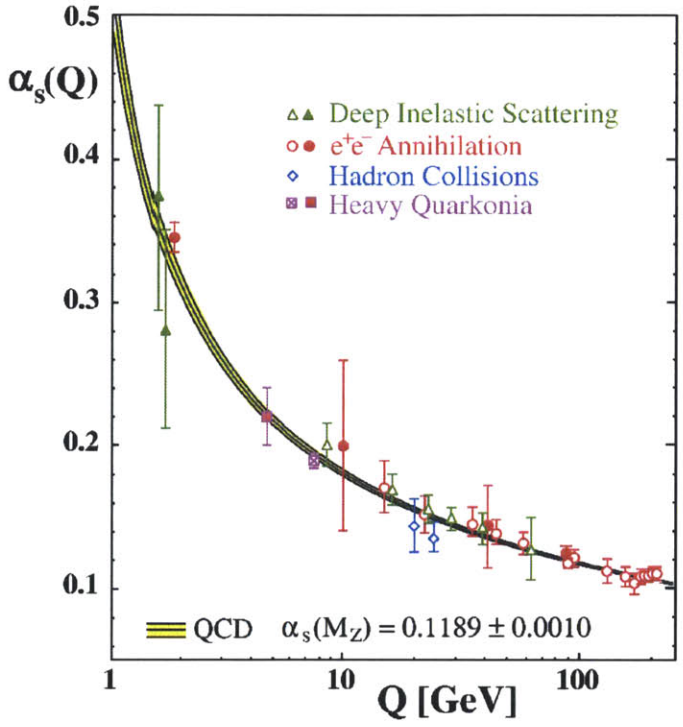

Figure 1-2: Measurements of the strong coupling constant α_s [1].

The scale dependence of the α_s can alternatively be pictured as follows. Since the gluon couples to itself, at larger scales there is more phase space of possible diagrams between two quarks. The gluons act like a Hooke spring between quarks. The energy stored in the spring can excite vacuum quark-antiquark pairs to produce hadrons.

When a quark is kicked rapidly out of a hadron, it turns into a spray of hadrons instead of moving freely as a quark.

In the relativistic heavy ion collisions, however, there is a rather large region covered with a medium of quarks and gluons. A quark with the same kick, in this medium, suffer through interactions with this medium before getting a chance to hadronize. By measuring the resultant hadrons in the detector, we are probing the parton after the medium interactions, and therefore measure the medium properties. As will be discussed in the later sections, the perturbative calculations of interactions between the partons and the medium rely on the coupling being small for highly energetic projectiles. For momentum transfer between soft gluons, however, the coupling is large and alternative methods have to be employed.

1.2.2 QCD Factorization

The collisions of protons is a complex system involving many particles. The valence and sea partons of each proton may interact with one in the other. When we study very high p_{T} interactions, the partons in the hard interaction can be treated independent of rest of the collision, due to small coupling at small distances [19, 20]. The cross section for a 2-to-2 parton scattering process can be expressed as follows:

$$d\sigma_{pp\to hadrons} = f_i(x_1, Q^2) \otimes f_j(x_2, Q^2) \otimes d\sigma_{qq\to qq} \otimes D_i(z_k, Q^2) \otimes D_j(z_l, Q^2) \quad (1.1)$$

The terms on the right hand side represent :

- The probability of finding a parton i in proton (or parton j in proton), called PDF. This is to be summed over all quark types and gluons.
- The hard scattering cross section between parton i and parton j, calculated perturbatively up to some convenient order.
- The probability of a parton i to produce a hadron k, (or parton j to produce a hadron l) called *fragmentation functions*. This is to be summed over all hadron

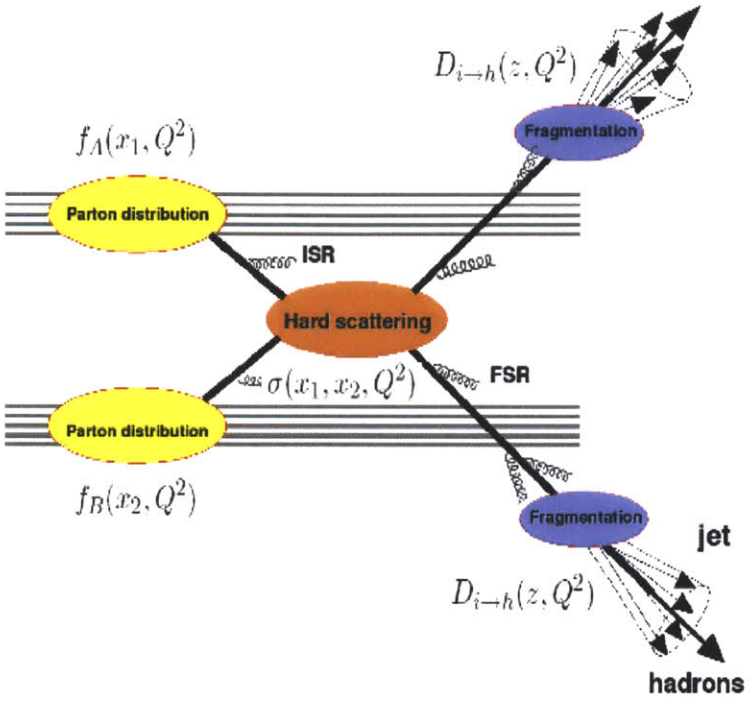

Figure 1-3: Illustration of factorization

types.

The parton distribution functions (PDFs) describe the composition of the proton in terms of valence quarks, sea quarks (quark-antiquark fluctuations) and gluons, as a function of the x variable, which can be considered as the fraction of proton's longitudinal momentum carried by the parton. Figure 1-4 shows the PDFs from the Particle Data Group [2]. As can be seen from these distributions, the contributions of gluons become very dominant at low-x values, and sea quarks start to appear as well, where high-x values are dominated by the light-quarks that define the nucleon.

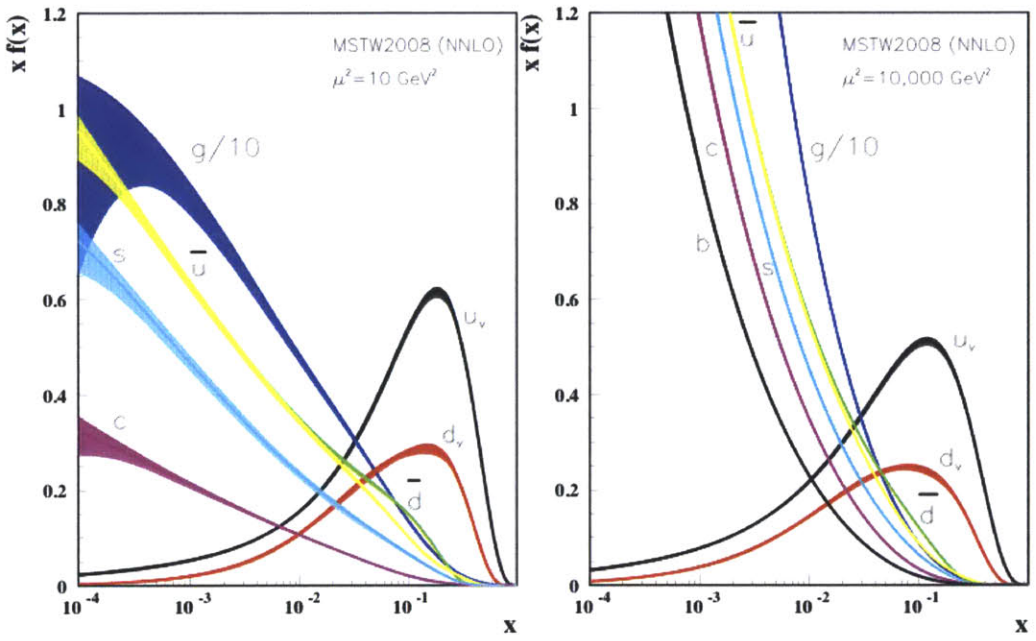

Figure 1-4: Parton distribution functions for protons (multiplied by x) for $\mu^2 = 10$ GeV^2 and $\mu^2 = 10^4$ GeV^2 [2].

1.2.3 Jets

In order to study a variable that can be calculated by the perturbative approach discussed in the previous section, we need to work with final state definitions that integrate out the infinities. The jets, clusters of hadrons, corresponding to the clusters of partons before hadronization, represent such a calculable object. In the experiment, it is straightforward to combine the signals and for clusters of energy. However the rules that define the cluster have a physical importance, since they also define the object of the calculation. If the experimental signal is treated in a way that is not easily incorporated to the theoretical calculation, then it is more difficult to deduce the underlying fundamental physics. As discussed in the previous section, the observable has to be insensitive to the radiation of a parton in very small angle or with very small momentum. The jet definition has to integrate over the region of infinity, and the algorithm in the experimental result should not be affected by any further splitting of the total energy. The jet definition also determines the scale of interaction to be probed. The larger the angular size of the jet definition, the less sensitive it is to soft parton radiation, thus corresponding to earlier time-scales. The choice is however also constrained by experimental challenges, which will be discussed in section 3.4.

1.2.4 Dynamics of jet production in vacuum

Before we get into the attractive discussion on the dynamics of QCD in hot medium, it is already worth noting that jet production in vacuum has interesting features by itself. The partons that recoil from a hard interaction have to undergo the radiation of their virtuality, and the radiated partons have to hadronize in accordance with the color-connections within. Below discussion summarizes these processes and highlights important aspects.

Divergence of radiation amplitudes

A high-momentum elastic parton scattering process results in a final state of hadrons, sprayed out around the initial parton momenta. The sum of momenta of the hadrons

around one parton has a non-zero mass, which results from the dispersion of the initial parton virtuality, Q, along a wide area through radiation of additional gluons. When the leading order contribution to this radiation is considered, as in the left diagram in figure 1-5, one observes that the amplitude diverges in the soft and collinear limits [20, 19]:

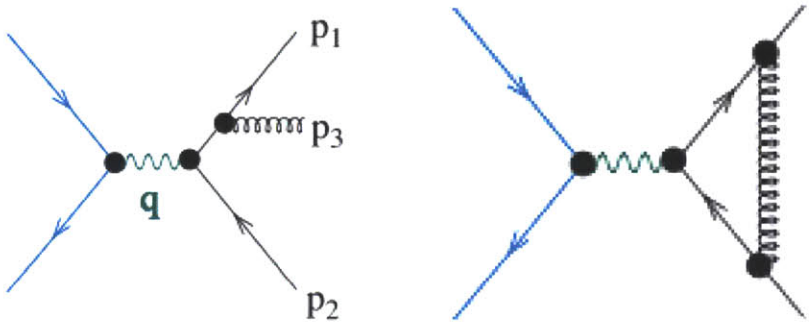

Figure 1-5: The diagram for the gluon radiation and the loop diagram at the next order. When all diagrams are added up, the loop diagram cancels out the divergence at the collinear of soft limit for p_3.

$$M \sim \frac{1}{E(1-cos\theta)} \sim \frac{1}{E\theta} \tag{1.2}$$

where E is the energy of the radiated gluon and θ is the angle between the radiated gluon and parent parton. This is called *infrared divergence*, and enforces the necessity of a cut-off in the integration over the radiated momentum. Due to unitarity, this divergence is in fact cancelled out by the loop terms when all orders of α_s are summed, as in right diagram in figure 1-5. In principle, any measurement that is insensitive to the collinear or soft radiation below a certain cut-off, can be calculated in leading order and can return a finite result. This is called *infrared and collinear safety* of the observable, and jet measurements consist of such observables, as will be seen in section 3.4.

Parton shower method

For realistic description of final states of hadrons, one needs to be take into account features within the collinear region. In Monte Carlo event generators for QCD processes, this is done by the *parton shower* methods. In this approach, the probability of a parton for splitting into two is calculated to all orders by summing up the infrared and collinear-enhanced terms. A parton in an event is allowed to split based on the probability obtained by the Sudakov form factor. The probability of successive splitting may be evaluated as a function of the virtuality of the radiated parton, or the angle of emission, as in figure 1-6. In either case, the shower can be evaluated down to a cut-off scale beyond which the final state is not sensitive to further splittings. The cut-off is typically in the order of a GeV, from which on hadronization takes over. In NLO calculations and beyond, one has to treat the overlap of the parton shower with the high order matrix elements carefully.

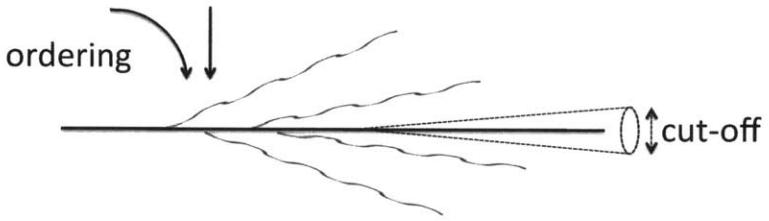

Figure 1-6: The parton shower method involves propagating the initial parton in a given variable, and according to the probability from the collinear enhanced terms in the radiation cross-section, randomly perform radiation of an additional parton.

In addition to the re-distribution of the momentum over a certain area, the color configuration of the partons is formed through the showering process, which responsible for many features related to interference effects, as will be discussed next, and later in the context of quenching.

Color coherence

The concept of color-coherence is useful in understanding the qualitative features of the radiation in QCD. When a highly collinear parton is emitted during the propagation, the has to take a while for the two colored objects to gain distance from each other, and from a larger distance, it is difficult to resolve their individual colors. In the perturbative approach, this means the amplitudes for the radiation to some momentum configurations, particularly those with a large angle, will interfere rather than add incoherently. A simple interpretation of this result is that, at certain angles it is difficult to resolve the individual radiated partons, and their net behavior is rather similar to the radiation from the parent parton, as shown in figure 1-7. This problem becomes simple when the shower is implemented by using the angle of radiation as the ordering variable. In QGP propagation, however, the colors of the partons may be reshuffled through interactions with the medium, which may affect this radiation pattern.

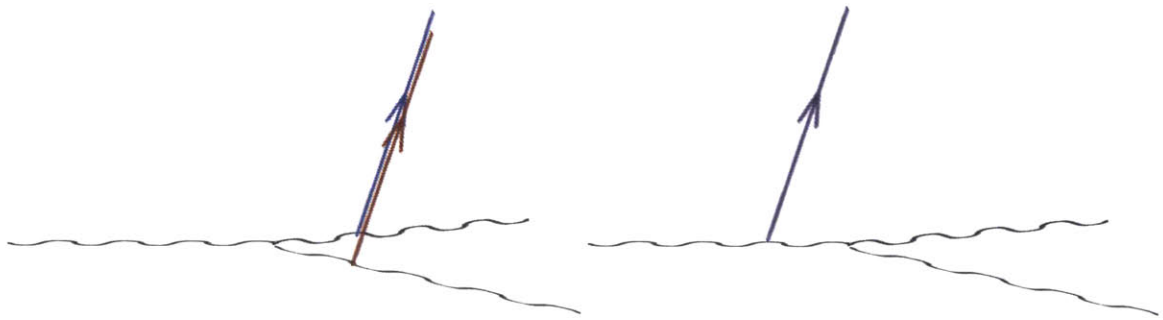

Figure 1-7: Illustration of the color-coherence effect in calculations of the parton-shower. The splitted collinear gluons are difficult to resolve unless they are sufficiently apart (loner time), and for smaller formation times (or large angles) their radiation interferes. In the angular-ordering prescription, the radiation of the splitted partons can be replaced by that from the parent parton whose color is sum of the two.

Hadronization

So far we were interested in how the shower of partons evolve until the time they form hadrons. Hadronization is modeled on top of this parton shower. In most of the discussion involved in this thesis, the effects that are specific to the hadronization

process are largely neglected. This simplification relies on the fact that the studies (and calculations) are only concerned with phenomena down to an infrared cut-off, $O(GeV)$, beyond which the physics is not resolvable. Potential hadronization effects [21] which correlate the physics within this scale to the properties of the shower may spoil this assumption, therefore one has to be careful by keeping in mind the possible hadronization effects in a certain study.

1.3 High density QCD with Heavy Ion collisions

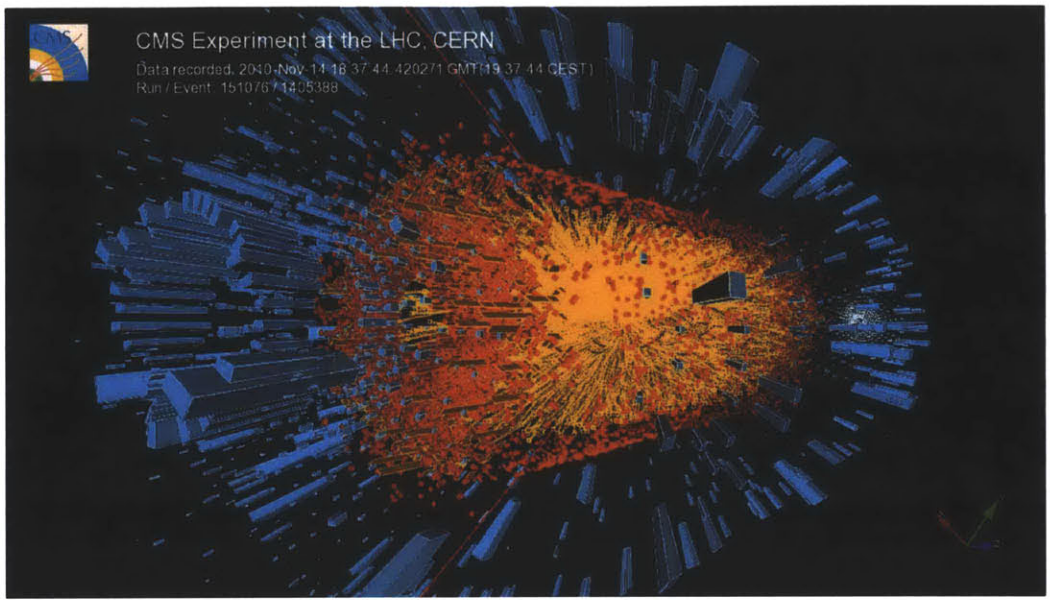

Figure 1-8: Event display of a central collision as observed by the CMS detector.

The properties of a possibly new form of matter at high temperature and high density, referred to as *quark-gluon plasma (QGP)*, is the main focus of the heavy-ion collisions at LHC and earlier similar experiments [10, 9]. These properties may shed light into the behavior of matter in the universe in its very early times, by when it had not expanded enough to let quarks and gluons to freeze into hadrons. When the Lorentz-contracted nuclei plates collide, a temperature in the order of few 100 MeV is achieved, in a small volume. This matter expands towards the surrounding vacuum, through processes that can be formulated by hydrodynamics and characteristics of QCD.

Being one of the most important terms in characterization of any medium, the temperature in the collision system is studied through measurement of energy density (via study of charged hadrons and calorimetry), low-energy (thermal) photon spectra, and the observed rates of quarkonia states. The sequential suppression [] of the excited states of heavy-quark bound states point to characteristic energy scales of the medium.

The initial energy density profile of the medium affects its evolution. In the RHIC

experiments [], it is observed that the angular distributions of the hadrons produced in a heavy-ion collision are directly related to the anisotropy of the energy profile in the overlapping region of the colliding nuclei. The observations are consistent with a hydrodynamic description of the medium expansion, and suggest a fluid behavior with very low viscosity. The measurements involve studies of fourier composition of the angular correlations, of which the strongest one is the second term, v_2, which is a result of the almond-shaped overlap area of two spherical distributions in mid-central collisions. This feature is called the *elliptic flow*, resulting an elliptical azimuthal distribution of particles. Higher-order moments of the initial state shape are also observed to be reflected in higher-order fourrier-components of the hadron correlations.

Having mentioned many of interesting features of the heavy-ion collisions, one other observable property of the medium, which is of main interest in this thesis, is the stopping power for energetic projectiles, or *opacity*. For high energy photons that do not interact by strong interaction, medium is completely transparent, as confirmed by measurements of photon cross-sections 1-14. For hard scattered quarks and gluons, however, the medium shows strong resistance, causing a large energy loss, resulting in *quenched* jets.

1.3.1 Jet-quenching in heavy-ion collisions

Hard parton scattering events may happen in PbPb collisions as well as pp collisions, however, in contrast to vacuum, although the small scale physics is similar, the dynamics of the longer range propagation of partons is be affected by this medium. In the earlier section when we stated that the small coupling at small scales allows the hard interaction to be independent of the surroundings. When the Pb nuclei collide, however, an extended region in space is filled up with a large density of energy, which results in significant effects on the hard scattering. The extent and limitations of this effect can provide information on the structure and properties of the medium. The jets were introduced in the previous section as a good tool to probe parton kinematics. It may as well serve us to probe the mechanics of the propagation in an extended volume. The modifications to the jets, relative to what would be expected

at the small distance scale, can represent the effects in the medium. There can be various scenarios to describe the effects on the jets. The models can be tested against many available observables. The different analysis channels like inclusive jets, dijets, high-pt tracks, photon-jets, inclusive photons all provide a wide perspective on the phenomena.

As will be discussed in the next subsection, the mechanism for quenching may involve different components each contributing to the energy loss by a different amount. Without having to construct the ultimate theory, we can ask the following basic questions on a qualitative level, which can guide the approximations/parameters involved in various approaches:

- How much energy is dissipated outside the jet cone?
- Is there a modification of the structure of the remaining jet?
- What happens to the dissipated energy?

Recent observations from LHC already have good hints to the answers to the above questions. This leads us to more sophisticated questions, which start to scratch the surface of medium properties:

- How does the energy-loss depend on the momentum of the projectile?
- How does the energy-loss depend on the amount of the medium traversed?
- How does the motion of the medium affect the energy loss?
- What are the degrees of freedom of the medium?

These questions motivate the detailed studies of the energy-loss mechanism with jets, their correlations to each other, their correlations to the medium behavior and the hadrons.

1.3.2 Perturbative description of jet-quenching

What we can learn from jet-quenching first relies on our understanding of the perturbative aspect of the phenomenon [22]. If the probes themselves are well under control, then we can make further statements on the nature and behavior of the medium. The probe in discussion, namely the jets, are rather well understood in vacuum with the methods discussed earlier in this section. One naturally attractive goal is then to incorporate the medium effects into this picture. There are different formalisms based on different set of assumptions or approximations, that attempt to implement this calculation. In all cases, the system under discussion involves many particles, which is easier to treat with MC generators, rather than analytical solutions.

A rough classification of the types of energy-loss may be the two components:

- energy transmitted to nearby medium constituents via elastic processes, referred to as **collisional energy loss**,
- medium-induced radiation of partons out of the cone due to decoherence of the parton wavefunction during the interaction with the medium, called **radiative energy loss**,

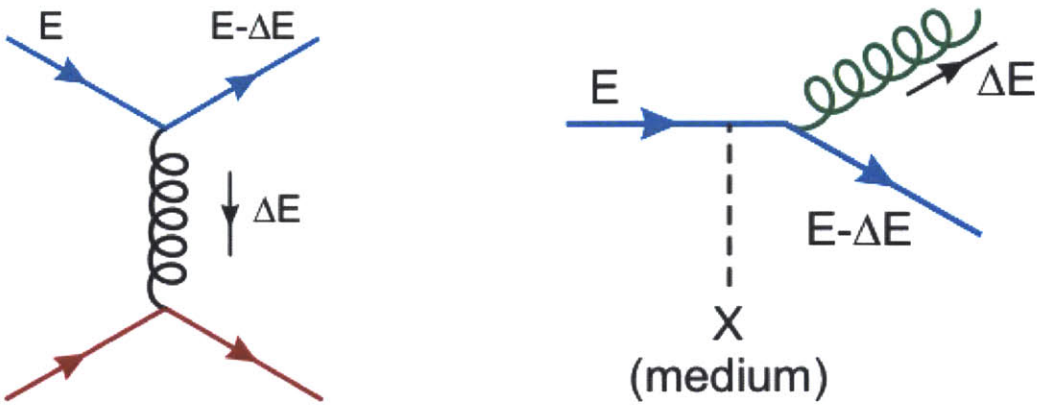

Figure 1-9: Elastic and inelastic processes inside the medium. [3]

The collisional energy-loss is also referred to as energy-loss due to **elastic processes**, since their description with diagrams have the same particles in the initial

and final states, whereas radiative process involve an additional gluon in the final state, thus named **inelastic processes**, sketched in figure 1-9.

Both modes of the energy-loss may have significant contribution to the observed quenching effects, and many theoretical models explore the features introduced by both of these effects. We will discuss the main items involved in calculation of energy-loss; however, the prerequisite is to interface our vacuum description of the jet evolution, which has rather effective tools already, to the medium case.

1.3.3 Formation of a parton-shower in medium

The first question to ask is the validity of the tools for the vacuum prescription of perturbative calculation, namely the parton-shower treatment of radiation. The formation time of a typical parton under study is comparable to the length scales of the medium, therefore one cannot very easily assume the shower to have formed before interacting with the medium, nor after. In section 1.2.4, we had stated that the coherence of collinear gluons suppresses radiation to large angles from partons with long formation time. In the case of the medium propagation, the situation may be different. The simple reason for that is the possibility that a parton can change color through interaction with the medium, breaking the correlation between emitted gluons. In contrast to the vacuum case where the interference of the splitted partons suppresses radiation at large angles, this time such large angle emissions are possible, and may play a role in the dissipation of energy outside the cone that the jet forms. The cartoon in figure 1-10 illustrates this feature.

1.3.4 Collisional energy-loss

Bjorken has performed one of the earliest calculations for energy-loss of a colored projectile [23] in plasma of quarks and gluons. The t-channel cross-sections over the scattering-centers in medium, are added incoherently. The parton is treated as an on-shell particle that multiple-scatters through the medium targets via soft elastic processes. In terms of the medium density, this calculation involved an infrared cut-

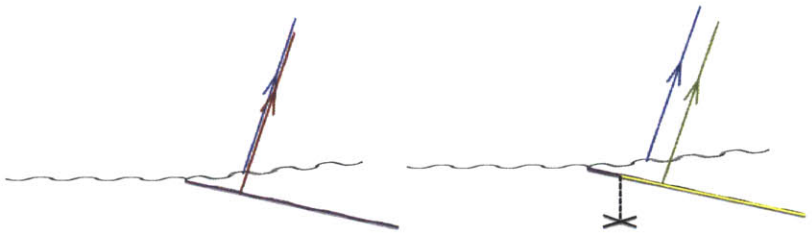

Figure 1-10: In the vacuum evolution of a parton shower, it is observed that the interference of radiation from collinear partons plays a big role in large angle radiation. In the medium scenario, the color of the partons may be re-shuffled through interaction with medium (in resolvable scales) and may allow incoherent radiation off the individual partons in the shower.

off scale in momentum in order to return a finite result. This cut-off can be justified by the color-screening effects at low energy, and Debye mass can be considered as a quantification of how well the projectile can resolve the medium constituents [24]. Also, [25] predicts a big difference between collisional energy-loss of heavy and lighter quarks, which may result in interesting features in studies of b-tagged jets in PbPb collisions. The average amount of the energy-loss in elastic processes depends highly on the medium model, and in certain models it can be of significant value and should be taken into account in dynamical calculations of the parton propagation.

1.3.5 Radiative energy-loss and the transport coefficient, $\hat{q}$

Eikonal approximation assumes the momentum of the projectile to be infinity, given that it is big enough compared to the typical momentum transfer. In this approximation, the momentum exchange with the medium happens only in the transverse direction. This means the net longitudinal force on the projectile is 0 and there is no collisional energy-loss. The energy is dissipated, however, when the transverse momentum transfer to the gluons in the shower accumulate enough relative phase to resolve it as a free parton leaving the shower, and dispersed in the transverse direction with Brownian motion:

$$\langle k_T^2 \rangle \sim \hat{q}L \tag{1.3}$$

where k_T is the momentum transverse to the shower axis, and L is the thickness of the medium.

At this point, it is important to realize the *LPM effect*. The suppression of bremsstrahlung off high energy projectiles in high density QED medium was shown in 1953 [26, 27]. The idea is that, within the finite formation time of a radiated photon, the interactions within the length traversed by the fast projectile interfere destructively. Since the formation time of the photon is related to its energy, the energy spectrum of radiated photons is sensitive to the spatial structure of the medium. The effect is valid for the QCD problem of today, and it is of great importance to the models describing the dynamics of the jet quenching. The extension of the LPM effect to the QCD medium is studied by [28, 29].

Integrating the radiated energy spectrum [30, 31], the amount of energy-loss is proportional to the characteristic radiation energy, ω_c:

$$\langle \Delta E \rangle = \int_0^\infty d\omega \; \omega \; \frac{dI}{d\omega} = \alpha_s C_R \omega_c \propto \hat{q}L^2 \tag{1.4}$$

where C_R is the Casimir color-factor, which is 4/3 for quarks and 3 for gluons. This result introduces a non-trivial path-length dependence (L^2 for a static medium), and it allows the characterization of the medium by $\hat{q}$ parameter alone.

The medium is actually not static, and it's going through a hydrodynamic expansion, which can be formulated in the time-dependence of $\hat{q}$ as in [32]:

$$\hat{q}(\xi) = \hat{q}(\xi_0) \times \left(\frac{\xi_0}{\xi}\right)^\alpha \tag{1.5}$$

where ξ represents the time, or equivalently, the distance traveled, ξ_0 is the plasma formation time and α represents the dimensionality of the expansion.

It is shown that the $\hat{q}$ of an expanding plasma can be formulated as an effective $\hat{q}$

for a static medium [33]:

$$< \hat{q} >= \frac{2}{L^2} \int_{\xi_0}^{L+\xi_0} d\xi \ (\xi - \xi_0) \ \hat{q}(\xi) \tag{1.6}$$

$$< \hat{q} > L_{effective} = \int_0^{\infty} \hat{q}(\xi) \ d\xi \tag{1.7}$$

In studies such as the "parton quenching model" [34], the amount of energy-loss for each jet can be described by a probability distribution, called the *quenching weights.* Later in this study, we will examine the results by toy models of these quenching weights, in a static medium.

1.3.6 Jet-quenching in the strongly-coupled limit

It is possible that a significant portion of the energy-loss happens with momentum transfer from soft gluon components of the jet, for which the coupling is large ($\alpha_s \sim O(1)$), as discussed in section 1.2.1. This makes the calculation non-perturbative, and alternative approaches can be more helpful.

Lattice QCD methods, although useful in calculating static properties of hot medium [35, 36], may not be suitable for calculation of dynamical processes.

The AdS/CFT correspondence may be a potential candidate for such a calculation [37], which has already been used for other medium properties [38, 39, 40, 41, 42, 43].

The definition of the transport coefficient $\hat{q}$, mentioned in the earlier section was based on purely perturbative concepts. In order to do study the quenching in non-perturbative terms, one has to find more general quantities. The discussion in [44] defines the $\hat{q}$ parameter in terms of the expectation value of Wilson loop in the adjoint representation:

$$< W^A(C) > \approx exp\left[-\frac{1}{4\sqrt{2}}\hat{q}L^- L^2\right] \tag{1.8}$$

This parameter is a well-defined quantity in without weak-coupling assumption,

and also exists for other guage theories. Although the gravity dual of QCD is not known, other gauge theories with similar features may be used in computing the properties of the QCD medium, such as the supersymmetric Yang-Mills theory (SYM) in the strongly coupled limit. Finding the value of $\hat{q}$ in strongly-coupled $N = 4$ SYM in large number of color (N_c) limit is equivalent to maximization of action surface in 5 dimensional anti-deSitter space, (AdS). The finite temperature in the guage theory is represented by a black hole with a horizon at $r = r_0$. Based on the assumptions that high temperature and high number of colors limit, remains a valid approximation for the QCD medium, the $\hat{q}$ calculated in SYM may relate to the value QCD.

The study in [44], finds $\hat{q}$ values in the ranges of 5-15 GeV^2/fm for RHIC conditions, which is of comparable magnitude with the values extracted from data [34, 45].

1.3.7 Medium geometry and quenching

The above discussion proposes that there is a very strong influence of the medium on the jets produced inside. As a result, the quenching effects depend on the event-by-event behavior of the medium and the relative location and orientation of the production vertex of the high energy partons. Studies of low-p_{T} particle correlations have shown that the evolution of the medium is strongly correlated to the initial geometric configuration of the overlap between the nuclei, and this configuration fluctuates event-by-event by a large amount [46]. Therefore, the density and the extension of the medium that a typical parton observes is different at each collision, which is an important factor in the calculation of a realistic jet-quenching model [47]. Not only the azimuthal anisotropy of the medium, but also local fluctuations can have influence on the effect. Such fluctuations in the temperature profile of the medium, are illustrated in right figure [4]. The fluctuations of the amount of medium can be quantified as in [4]. The probability distribution for a parton observing a certain *effective* pathlength, (effective, meaning weighted by density) is shown in the left figure 1-11.

The cross-section for a high-p_{T} process decreases rapidly with p_{T}. When the sample is selected based on a high-p_{T}triggering jet (or hadron), it is more likely that

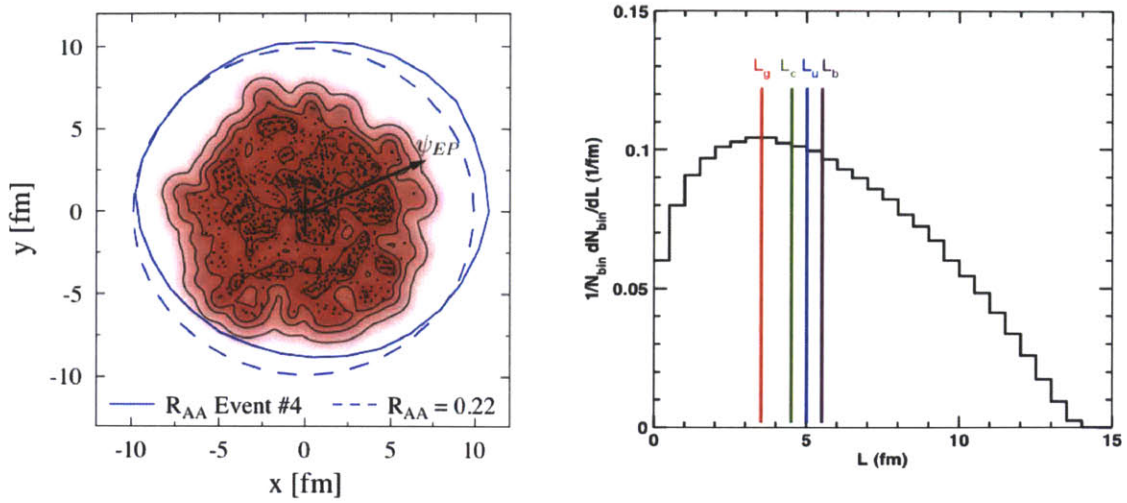

Figure 1-11: Left : Temperature profile on the transverse plane in a central collision between Au nuclei. Right : The probability of a parton to traverse a given (density-weighted) path-length. Each parton samples a different value from this distribution and suffers a different amount of energy-loss. The lines are related to a different calculation where an effective fixed path-length is used [4].

this jet has suffered little energy-loss than being with higher initial p_{T} that is quenched to this value. This also means the triggering jets observed are those produced closer to the surface of the medium, a situation referred to as *surface bias*. The production vertex distribution of surviving (p_{T}> 15 GeV/c) inclusive partons in AuAu collisions is illustrated in figure 1-12 [48].

Every parton travels a different amount of medium: both the length of travel and the conditions (density and temperature, or simply $\hat{q}$) across the traversed medium, differs for every parton. The path-length dependence of the energy-loss is very interesting, for it distinguishes between various descriptions (and types) of the energy-loss, introduced above. For example, due to the LPM effect discussed in 1.3.5, it makes a difference, whether a fixed amount of matter is distributed along a long distance or squeezed into a smaller path. The more compact the material is placed, the more the coherence effects come into play, reducing the amount of the energy-loss.

The path-length dependence of energy-loss is also sensitive to the expansion of the medium. As a parton traverses the medium at a fixed speed ($\sim c$), it experiences

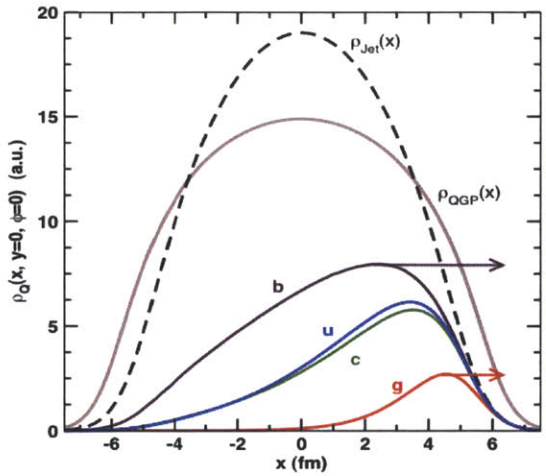

Figure 1-12: The vertex distribution of surviving partons (final $p_{\mathrm{T}} > 15$ GeV/c) in AuAu collisions for different flavors. The stronger the energy-loss, the more the partons are biased to be emitted from the surface of the medium.

the distant parts of the medium at later times, where $\hat{q}$ has evolved according to 1.6.

As a result of the role that the configuration of the medium plays in the energy-loss, it is of great interest to explore the data in observables that can distinguish the geometry dependent effects, from the other average medium properties. The correlations between dijets, as we will see in the analyses discussed in this thesis, provide such an insight to this problem. In the high-p_{T} dijet events, where parton momenta are balanced in the initial hard-scattering, the two jets lose a different amount of energy due to different material and distance travelled. As we will see, the imbalance between these jets reflect the material and path-length dependence of the quenching.

1.3.8 Jet quenching at RHIC and LHC

There has been a large volume of evidence for energy-loss phenomena from the RHIC experiments [9, 10, 11, 12]. The collisions at a nucleon-nucleon center of mass energy $\sqrt{s_{NN}} = 200$ GeV already have shown signatures of quenching. One of such measurements is the suppression of the high-p_{T} hadron production, quantified by the nuclear modification factor, R_{AA}:

$$R_{AA}(p_{\mathrm{T}}) = \frac{d\sigma^{AA}/dp_{\mathrm{T}}}{< \mathrm{N_{coll}} > d\sigma^{pp}/dp_{\mathrm{T}}} \tag{1.9}$$

One observes that the hadron spectra is suppressed by a factor of 5 at some momenta, as in figure 1-13. This suppression can be caused by a shift of the hadron p_{T} spectra to lower p_{T} values, thus appearing as a suppression. An alternative way of thinking of this effect is, if some hadrons are not produced any more due to the quenching of the partons, only a fraction of the jets, which originate from the surface of the medium, may produce the high-p_{T} hadrons, where R_{AA} represents such survival probability. The actual effect may be a combination of the two, the amount of energy degradation may differ for each jet in each event, therefore a more dynamical quantification of the energy-loss would be helpful.

However, as discussed in section 1.2.2, it is difficult (yet possible) to relate the hadron-level measurement to the partonic dynamics. In particular, the measurement of hadrons, being a result of convolution of both energy-loss and fragmentation effects, degrades the precision of this measurement in terms of the partonic energy-loss. The value of $\hat{q}$ that was estimated from these measurements [34, 45] had to rely on the fragmentation functions, which may impose theoretical uncertainties. These calculations suggested a $\hat{q}$ value of roughly 15 GeV^2/fm; however, [45] also states that due to the surface-bias, the hadron R_{AA} may lose sensitivity to the exact value of $\hat{q}$ when $\hat{q}$ is greater than 5 GeV^2/fm.

The study of azimuthal correlations between high-p_{T} hadrons can also probe the dynamics of the energy-loss, this time with sensitivity to the correlation between the energy lost by partons on either sides of the hard interaction. The results, as seen in figure 1-13, suggest that there are cases in which one jet is absorbed while another one survives to produce the trigger high-p_{T} hadron. Study of the azimuthal correlations with lower p_{T} hadrons pose difficulties due to the flow effects in the underlying event and the interplay between the quenching and the flow. In addition, the fragmentation remains an intermediate process between the actual effect and the observation.

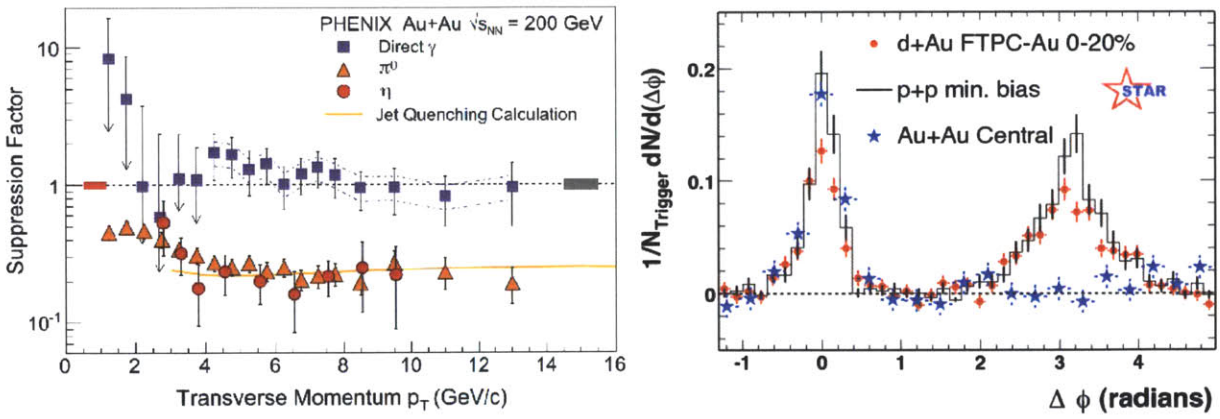

Figure 1-13: Hadron R_{AA} and correlation results from RHIC experiments.

The availability of the LHC data has significantly improved the p_T range accessible to hadron measurements 1-14. This already helps the analysis of the transport coefficient, $\hat{q}$, however prone to the same issues discussed above. The possibility of full jet reconstruction may help factorize the different levels of effects. First of all, the fragmentation of the jets can be quantified in terms of the hadrons and the observed jet energy, to see if the longitudinal profile of the shower (and possible medium response) has changed. This may serve as a connection between the parton level energy-loss calculations and the hadron measurements. On the other hand, the jet R_{AA} provides a closer look into the energy-loss in parton level. Furthermore, correlating back-to-back jets can provide many observables that are most sensitive to the different modes of the energy-loss. The azimuthal correlations of dijets, as an example, can probe any high momentum radiation in large angles, such as enhancement of early radiation at high virtuality. Another measurement is the momentum imbalance between dijets, which is sensitive to the location of dijets in the medium, and can factorize the medium-dependence of the energy-loss from the fluctuations in the shower process. In this thesis we will go through the analysis of these observables, and will try to learn about the medium effects on jets.

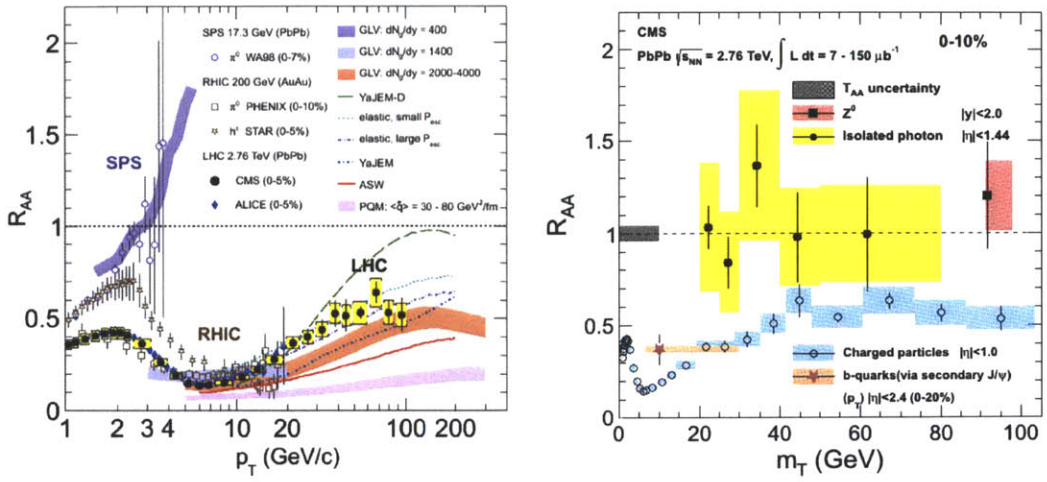

Figure 1-14: The compilation of R_{AA} results from CMS. Because the heavy particles are also included in the figure, the x axis is labeled m_T, which is simply p_{T} for approximately massless particles (charged hadrons and photons) and m for low-p_{T} heavy particles (J/ψ and Z).

Chapter 2

CMS experiment and data

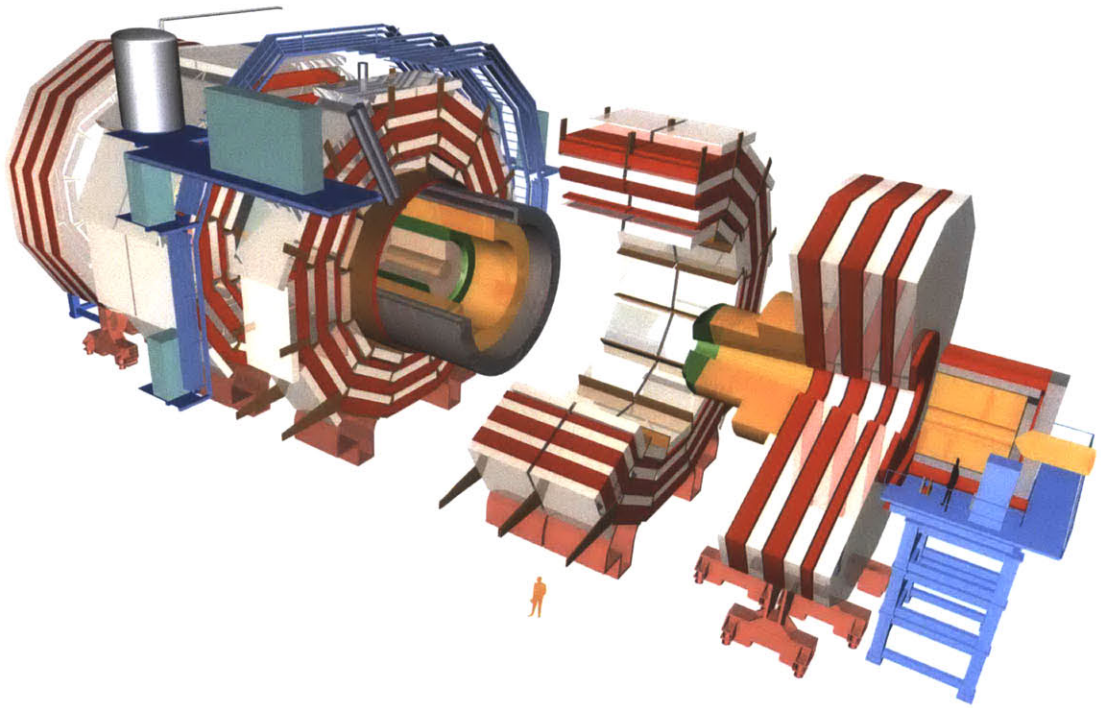

Figure 2-1: Various elements of the CMS Detector.

CMS is a multi-purpose large angular coverage detector, with a very high magnetic field (3.8 T) and very dense material, whose detailed description can be found in [49]. It is initially designed to study the physics of high-energy proton collisions, which require a good precision on QCD related probes [50]. It later proved to be an optimal

design also for the heavy ion collisions, with its wide coverage, precise calorimetry and good tracking.

2.1 The Tracking System

The tracking system in CMS is composed of two kinds of detectors: the Silicon Pixel Detector, as the closest detector element to the beam, and the Silicon Strip Chambers, surrounding the pixel detector.

2.1.1 The Silicon Pixel Detector

The pixel detector is the closest detector to the beam, and has a high granularity, which makes it a useful tool for the measurement of vertex position along and transverse to the beam axis. It is composed of three cylindrical layers around the beam referred to as barrel and two layers of disks at each side as endcaps, as illustrated in figure 2-2. The barrel layers extend to 53.3 cm along the beam axis, and are at distances of 4.3, 7.3 and 10.4 cm from the beam axis. The endcap disks have a diameter of about 15 cm and are positioned at z of 34.5 and 46.5 cm, on both sides. There are in total 66 million pixels, which can handle the greatest multiplicity events achieved in heavy-ion runs or pp runs with high pile-up.

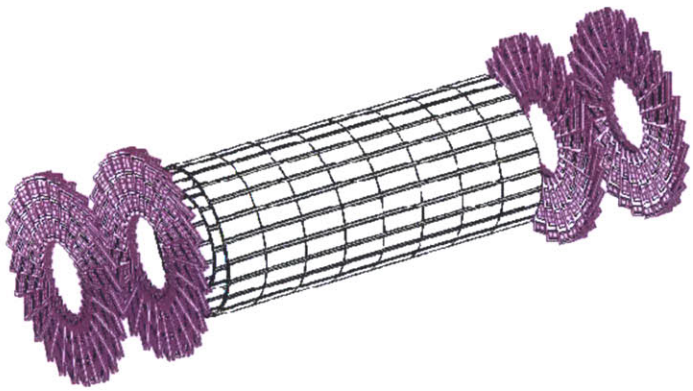

Figure 2-2: Silicon Pixel Detector.

The pixel detector is made of smaller detector units called modules, each contain-

ing two rows of 8 read-out chips connected to the active area. In barrel, there are in total 672 modules of rectangular shape and 96 additional half modules (with only one row of 8 read-out chips). In the endcaps there are 24 wedge shaped modules on each disk.

The pixels have an area of 150x150 μm^2, on a sensitive silicon layer of 250 um thickness. The orientation of modules are tilted in a way to optimize the charge share between pixels due to Lorentz angle, which results in a position resolution of 10 um and 15 um in azimuthal and z directions respectively.

One of the early and most important measurements in PbPb (and pp) was the measurement of the charged hadron multiplicity, which primarily used the signal in the pixel detector which has a good hit efficiency down to very low values of charged hadron p_{T} [51, 52].

2.1.2 The Silicon Strip Detector

The Pixel Detector is surrounded by a large (24 m^3 volume of pads with pixel strips. Different subsystems, which are responsible for a different angle of coverage, have slightly different design of strip modules. The different subsystems, TIB, TID, TOB and TEC are shown in figure 2-3. The surfaces of the modules, typically 10cm wide, consist of 80μ m strips. The thickness of the silicon is 320μ m in the inner tracker and 500μ m in the outer layers. Some modules are mounted back-to-back to be used as *stereo modules*, which are used in some layers.

The signal is read-out by custom integrated circuits, using optical fibers to transmit signal to the Front End Driver (FED). A single FED receives data from 96 fibers, with 256 channels per fiber. The pedestal and common-mode noise subtraction are applied to the digitized signal in the offline reconstruction (and HLT) process.

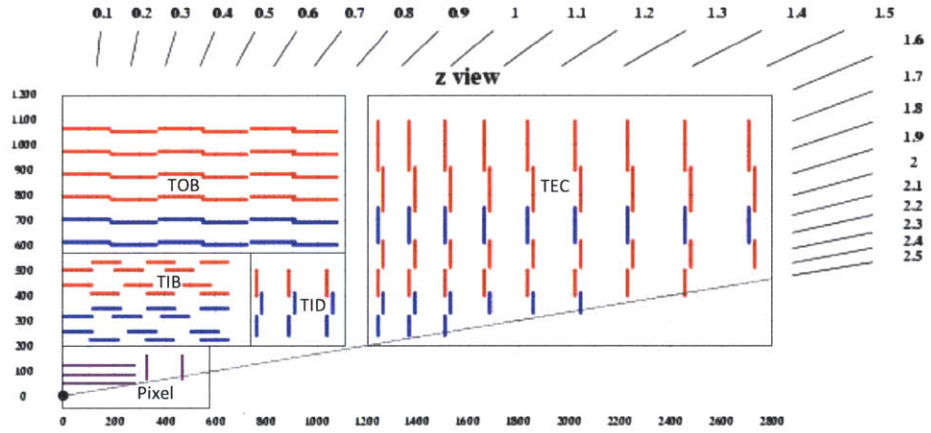

Figure 2-3: Components of the tracker. The red strip layers are single-sided and blue layers are double-sided (stereo) strip layers. The pixel detector is shown in purple.

2.2 The Electromagnetic Calorimeter

The CMS Electromagnetic Calorimeter (Ecal) is a system of lead-tungstate scintillators and avalanche photo-diodes (APD) that provide crucial information on electromagnetically interacting particles, mainly photons and electrons. In the context of jet quenching studies, the Ecal is particularly important for photon reconstruction, and in jet reconstruction where an important fraction of hadronic energy consists of π^0s which are observed as photons in the final state. The Ecal Barrel, EB, covers the pseudorapidity range of $|\eta| < 1.479$ and the Ecal Endcaps, EE, cover $1.479 < |\eta| < 3$. The EB is made of a single layer of lead-tungstate ($PbWO_4$) crystals, which have a radial length of 23 cm, and a width of 22×22mm in the inner edge and 26×26mm in the outer edge. $PbWO_4$, having a very high density, provides a short radiation length ($X_0 = 0.89cm$) and small Moliere radius (2.2 cm). The EE crystals are 22 cm long, and of area of 30×30mm. Sampling of the scintillation is performed by Avalanche Photo-Diodes (APD) in the barrel, and by Vacuum Photo-Triodes (VPT) in the endcaps. The pre-shower detector, ES, is a lead sampling calorimeter with silicon sensors, covering the end-caps, which is used to discriminate π^0 and direct photon signals. This subsystem was not used in the analyses of heavy-ions.

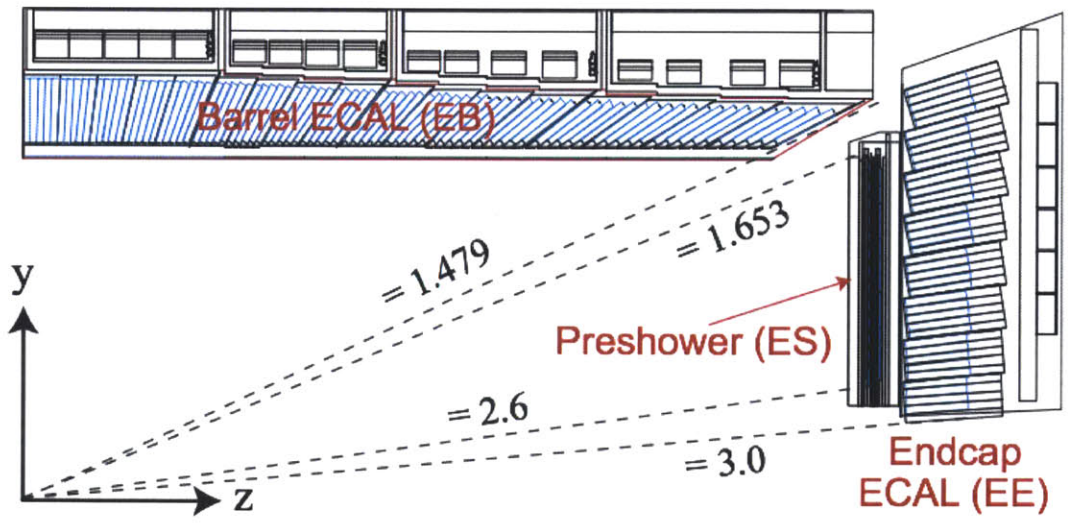

Figure 2-4: Ecal Detector.

2.3 The Hadronic Calorimeter

The Hadronic Calorimeter, Hcal, system in CMS is a combined system of different components. In the mid-rapidity region, a hydbrid absorber-scintillator calorimeter is used, and in the forward region, due to high irradiation, a Cerenkov radiation based system is used. Since these components have very different characteristics, we will discuss them separately.

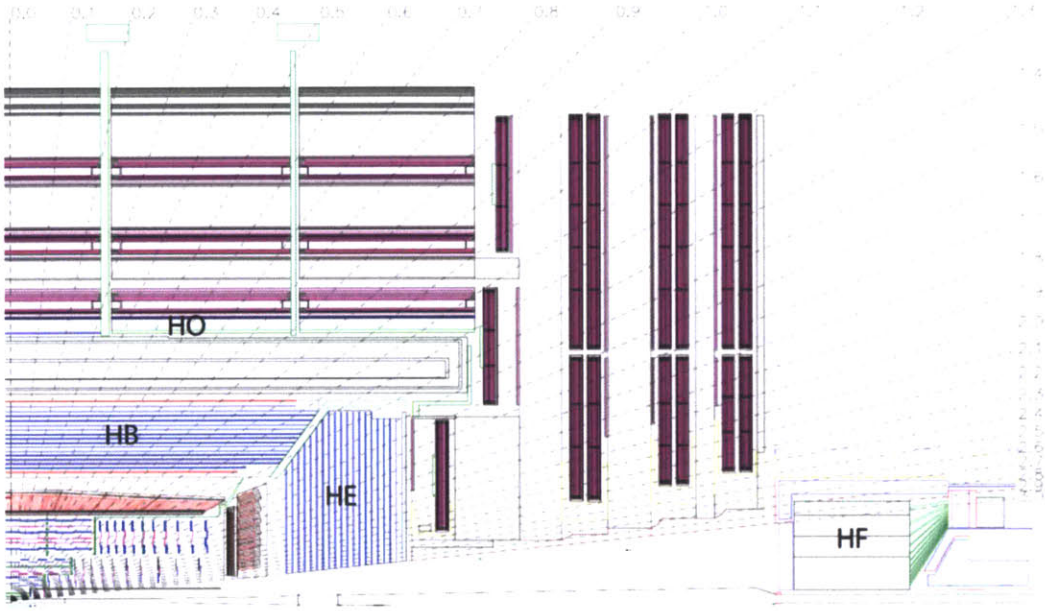

Figure 2-5: Hcal Detector.

2.3.1 Barrel and Endcap (HBHE)

CMS uses a hybrid calorimeter of brass plates and plastic scintillators for measuring the energy of hadrons at mid-rapidity. There are two subsystems, Hcal Barrel, covering $|\eta| < 1.3$ and Hcal Endcap for $1.3 < |\eta| < 3$. The system has a depth of 13 interaction lengths in order to guarantee the complete absorption of hadrons. The towers of radially stacked brass and scintillator plates, have a granularity of 0.087×0.087 in $\eta \times \phi$ in barrel and 0.17×0.17 in endcap. The goal of HBHE is to absorb all energy from charged and neutral hadrons, to be clustered in to jets or to

determine the missing transverse energy (MET) when combined with the information from Ecal and tracker. A jet of radius 0.3 typically consists of 37 calotowers, which can resolve the shape of the jet to a good extent.

2.3.2 Forward (HF)

HF is a system of quartz fibers placed behind a lead absorber. The Cerenkov radiation in the fibers are guided to the PMTs which are placed close to the detector in order to achieve fast response.

The HF detector has a particular importance in studies of PbPb collisions due to its role in two most important ingredients in any analysis:

- **Event selection** The first task in analysis of PbPb and pp collisions is selecting a sample purely corresponding to the physics of interest, free of background from other processes that happen in the collider. HF plays an important role in event selection because it can quantify the topology of the soft particle production in a collision, which is an important discriminator of many event types. Event selection is further discussed in Section 6.1.

- **Centrality determination** The centrality determination procedure is discussed in the Chapter 5. The HF detector is chosen to represent the centrality because it is farther from the calorimeters in mid-rapidity that constitute the main observables. This way, the centrality determination is not biased by the presence of the jets that are the object of the study.

Another important task that is preformed by HF is **event-plane reconstruction**, which finds the angle in the x-y plane in which the collision occurred. This is particularly important for studies of elliptic flow, in which the azimuthal anisotropy of the particles is quantified with respect to this angle. In the analyses discussed in this thesis, the effects of the flow to the first order are neglected, and the event plane determination is not used.

The HF detector is also used in jet reconstruction, however in the studies discussed in this thesis, the analyses are restricted to jets in the barrel region. The cross

section of high-p_{T} jets in the forward region is very low, therefore limiting the effective acceptance does not affect the results on the dijet correlations.

2.3.3 Outer calorimeter (HO)

HO is an extension to the barrel calorimeter, an additional layer of absorber and scintillator located outside the magnet coil, with towers of 0.17×0.17 granularity in $\eta \times \phi$. HO mostly aims to distinguish hadronic residual from muon signal in the outer muon tracker, and it is not primarily used in the studies discussed in this thesis.

2.3.4 Zero-Degree Calorimeter (ZDC)

A set of hybrid calorimeters are placed on the z-axis on both sides of the detector, at a distance of 140 m from the interaction point. The main purpose of these detectors is to capture the neutrons that result from the fragmentation of the nuclear remnants in PbPb collisions. It provides complementary information for triggering and centrality determination.

2.3.5 Beam Scintillation Counters (BSC)

The BSCs are 2 cm thick pads of scintillation detectors, located at the surface of the HF on both sides of pseudorapidity, as shown in 2-6. They cover the rapidity range of $3.9|\eta| < 4.4$. The main purpose of these scintillators is to detect coincidence of beam-correlated signal with precise timing, therefore they are important for event selection and triggering.

2.3.6 Beam Pick-up Timing Experiment (BPTX)

BPTX is an electrostatic beam detection device, positioned 175 m away from the interaction point. Its main purpose is to detect the beam presence on either side, therefore it is useful in the triggering.

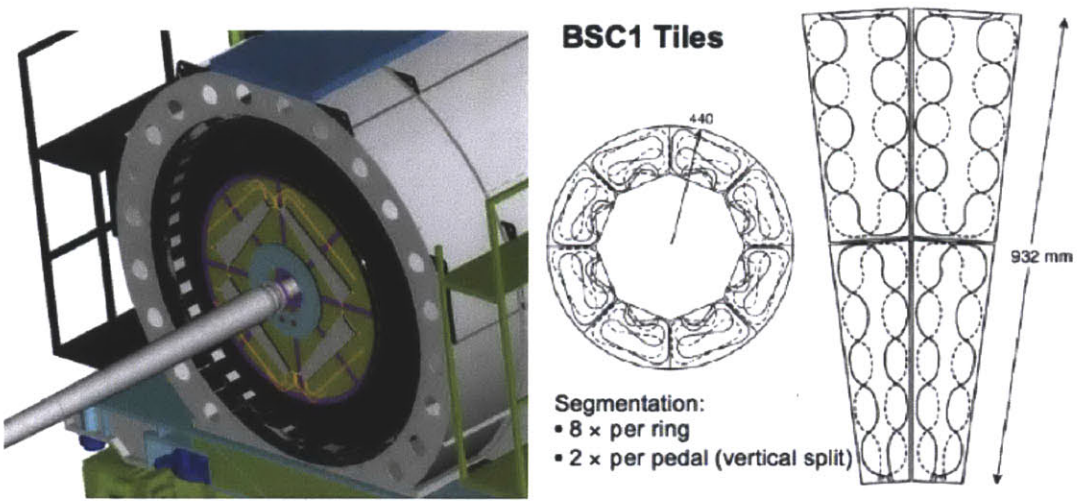

Figure 2-6: The beam scintillation counters are placed on the inner sides of the HF detector, with 16 segments on each side.

2.4 The Muon System

CMS is surrounded by a muon detector system, which is crucial for studies involving triggering and selection of muon-related events, such as leptonic decays from vector-bosons or quarkonia, which are also good probes for the studies of medium properties.

There are different components in overlapping barrel ($|\eta| < 1.3$) and endcap ($1 < |\eta| < 2.4$) regions. Drift Tubes (DT), are located only in the barrel region. They are drift chambers with an anode wire of 50μ m thickness. Stacked between layers of the drift tubes, Resistive Plate Chambers, (RPC), are layers of gaseous parallel-plate detectors.

RPCs are also available in the Endcap, however, instead of DTs, Cathode Strip Chambers (CSC) are used here. These are 6 layers of multi-wire proportional chambers placed in the endcaps.

The muon system is not extensively used in most of the studies in this thesis, although it is an important actor of reconstruction in the study of heavy-flavored jets, which provide complementary information to the study of quenching with light partons.

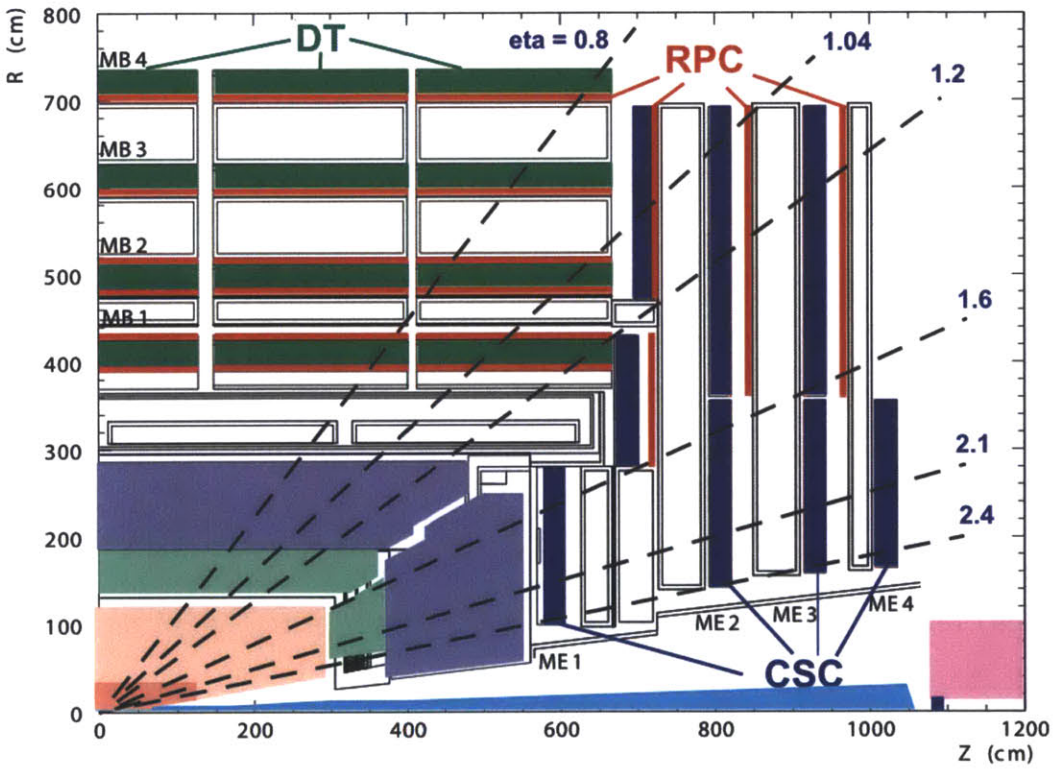

Figure 2-7: Muon Detectors.

2.5 Triggers and data samples

2.5.1 Trigger system

In order to make the best use of the available computing resources and high luminosity of collisions, the detectors must have a triggering system which can select and categorize the events to record. CMS uses a two level trigger system, implemented in hardware (L1) and software (HLT) levels.

The Level-1 system ($L1$) triggers the readout of the detector in hardware level. The decisions from a singe detector subsystem are transmitted as "technical bits", and some technical bits are combined by detector firmware to form "algorithm bits". Some of these L1 bits are specified to be "active", meaning when the decision returns true, the read-out of the whole detector is performed.

The High-Level Trigger (HLT) runs on the computer farm located in the P5 cavern, where event building from various detector signals also takes place.

HLT is a typical CMS software process, composed of multiple *paths*. A path represents a sequence of operations on a given event, and the final decision to qualify the event. An HLT path is seeded by a given L1 bit, and it can run any type of offline reconstruction on the event in order to perform the decision. Certain optimization of this reconstruction is needed in order to accommodate for the high rate of events received by the HLT farm. The reconstruction in HLT is very similar to the full reconstruction that is used in the analysis, with the following differences:

- **Calibration** : Since the calibrations can only be perfect after a full processing of the data that is being recorded at any instant, the calibrations at the time of the data acquisition may differ from the ones used in full reconstruction, which happens with a certain latency.

- **Tracking** : Full tracking is not run for all paths available in the HLT. It is available for certain dedicated paths with limited rate, in order to maintain the satisfactory timing.

- **Jet algorithm** : Although ParticleFlow jets (described in section 3.3, which

employ tracking, are used in offline analyses, the triggering is performed on calorimeter-only jets.

In HLT, the events are selected based on their physics content, and certain abundant physics channels are pre-scaled (repetitively skipped) if necessary. Some trigger paths, relevant for the dijet analyses, are described below.

Minimum-bias event triggers

Minimum-bias event triggers are very important for heavy-ion collisions. Even in studies of rare probes, one has to know well about the bulk properties of the medium in an unbiased selection, which influence the MC tuning, centrality determination and investigation of underlying event effects to hard probes.

The coincidence of signals in HF and in BSC are helpful in associating the event to a common vertex in the vicinity of the interaction point. The trigger bit "HLT_HIMinBiasHfOrBSC" accepts events in which either both sides of HF or both sides of BSC are hit. This path, like all others used in analyses, is gated with the BPTX coincidence to ensure using only beam events.

Calorimeter jet triggers

The calorimetric coverage of CMS allows the identification of all high-p_{T} jet events. The signals from Ecal and Hcal are added together to form *CaloTowers*, on which the jet algorithms (with background subtraction, as described in 3.4), are run. To be discussed in more detail in section 4.1.1, the energy resolution for calorimeter-based jets is not as good as those reconstructed with ParticleFlow, therefore a lower threshold, than that to be used in the final analysis, has to be preferred. Figure 2-8 shows the turn-on curve for the 80 GeV jet trigger, as a function of offline-reconstructed PF jet p_{T}.

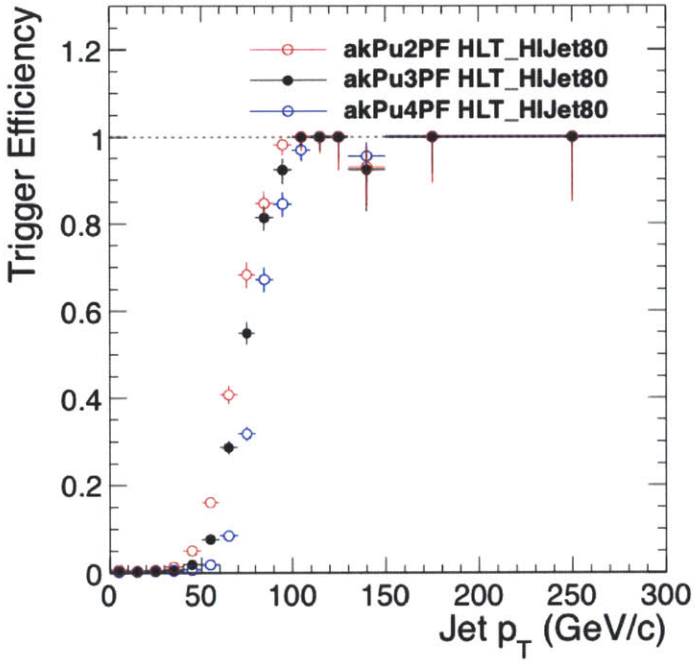

Figure 2-8: Efficiency of the jet trigger as a function of offline PF jets. Some inefficiency at 140 GeV is observed, which is an artifact of fake tracks which affect the PF jets and do not affect calorimeter jets.

2.5.2 Data samples

- **2010 PbPb sample** : 6.8 μ b^{-1}

  The first LHC run of Pb ions was with a low luminosity of XXX, in which CMS was able to record all collisions without the need for prescales.

- **2011 pp sample** : 231 nb^{-1}

  Although a huge dataset of pp collisions at 7 TeV was collected by CMS in the last years, the proton run at 2.79 TeV was very useful for heavy-ion studies, as it provided a good reference for medium-related effects in PbPb studies.

- **2011 PbPb sample** : 150 μ b^{-1}

  This was the last and longest run as of the time this thesis was prepared, on which most of the analyses are based on. The high-statistics allowed the study of a p_{T}differential approach in the study of dijet imbalance, which is the essence of this thesis.

2.5.3 Simulations

The simulations involve two important components:

1. A signal (high-p_{T} dijet) event of vacuum behavior, chosen to be Pythia [53]

2. An underlying minimum-bias event, generated by Hydjet [54, 55]

The events produced by these MC generators are propagated through the detector by Geant [56] simulations. Pythia events are superposed on the events from an earlier produced Hydjet sample, in a consistent vertex position in order to represent a single combined event. This procedure is called *event embedding*. The resulting signal, including noise in the measured amount, is reconstructed with the same methods as applied to data.

The Hydjet sample, without embedding, is also useful in studies of minimum-bias data, and tuned to match the observed minimum-bias properties such as (mostly low-p_{T}) hadron spectra, multiplicity and elliptic flow.

When a data sample is selected on a rare high-p_{T} process, it is biased towards more central events. This is because the number of binary collisions, therefore the probability of the process to occur, is larger in these events. Since the sample is generated with a minimum-bias centrality distribution, the MC is re-weighted with the centrality distribution observed in data in order to accommodate for an equivalent centrality bias.

The simulations are important for two reasons. First of all, the performance of the reconstruction and systematic effects of the analysis can be estimated with the help of simulations. In addition to that, in the cases where a consistent reference (pp) data is not available, Pythia is considered as the baseline for medium effects observed in data. In such situations, one has to consider the limitations of leading-order MC, and try to avoid sensitivity to higher-order effects.

Chapter 3

Particle and jet reconstruction

3.1 Track reconstruction

Tracking in a dense environment is a certainly very interesting challenge. The CMS detector is designed in a way to handle not only single pp collisions, but also high track multiplicity in many pp interactions happening simultaneously, called *pile-up*, which is the natural environment of the high luminosity runs that the LHC was designed for. It was then shown that the tracking system can go further and reconstruct tracks in even PbPb collisions. One can understand that, the high multiplicity in the PbPb collisions may by combinatorics create a larger number of fake tracks compared to those in pp, and the tracking may have to be more selective, with the cost of less efficiency. In addition, the high occupancy in the detector may introduce a loss in efficiency already in the algorithm level. Although the tracking in HI analyses was intended to be as close to the pp tracking strategy as possible, certain modifications were implemented in order to achieve the best performance in the perspective of the intended HI analyses. The tracking algorithm consists of the steps discussed in the following subsections.

3.1.1 Hit reconstruction in pixel and strip detectors

When a track traverses a piece of active tracker layer, the excited electron-hole pairs spread in a larger area than a single pixel/strip. Particularly for the fact that there is both a constant **E** field (for charge accumulation) and a **B** field, the particles drift in a specific direction called the *Lorentz angle*, which enhances this spread. The charges accumulated in the detector therefore should be clustered to locate the exact position of the track. The integration of the charge in a cluster returns an estimate of the energy that the particle has deposited in the active volume, which provides input for particle identification via *dE/dx method* (although not used directly in this analysis). It also helps to estimate the orientation of the track within the local volume, for which the spatial extent of the cluster also provides information. This is important when checking hits for their compatibility with the vertex, which will be discussed in Section 6.1.

3.1.2 Vertex reconstruction

The collisions of the beams happen in a finite region in the center of the detector, which is very small in the transverse direction (a few μm), since the beams themselves are very narrow; however very wide in the z direction (10-20 cm), since the bunches in the beams are wide. The parameters that describe the region of possible collisions to happen, its center and width in 3 dimensions, is called the *beamspot*. The beamspot is calibrated both in real-time during the data-taking, and offline before data processing (with better precision). Since the beamspot is wide in the z direction, in order to reconstruct the primary tracks in a given event, it is important to determine, event-by-event, the exact position of the collision, named the *event vertex*. It is possible to localize the position of the vertex without already having fully reconstructed tracks. As mentioned in the previous subsection, the spatial extent of the pixel clusters, called *cluster size*, encode information on the track orientation. With a survey of the pixel clusters, one can constrain the vertex position to a much narrower region than what the beamspot allows. Based on this rough vertex position, tracks in the pixel detector

can be reconstructed, called *proto-tracks*. With more precise information from the momenta of these proto-tracks, the vertex position is determined to a good precision, and used as an input to full tracking.

3.1.3 Seed finding with pixel detector

The pixel detector, with its very high spatial resolution, in a small volume, can determine some preliminary information on the tracks, by grouping the hits in the different layers in pairs, or triplets. The grouping starts from the outer layers of the pixel detector where tracks are expected to be well separated in space. The outer layer hits are matched to inner layer with a constraint on the compatibility with the vertex, forming *pixel pairs*. In the case of barrel, the grouping can include the innermost layer, forming a *pixel triplet*. In the cases where a vertex is not successfully reconstructed, the constraint can be based on the beamspot. In the analyses discussed here, however, only events where a vertex is well reconstructed are analyzed.

3.1.4 Trajectory finding

The inner part of the CMS detector is filled up with a very homogeneous **B** field of 3.8T in the z direction, with no **E** field. The solution to the Lorentz force for a charged particle in this field is a *helix*, which can be parametrized by the initial momentum and position of the particle. The seeds in the pixel detector can constrain these parameters by a good amount before trajectory finding in the strip detector. The trajectory is then extrapolated to the strip detector volume, also taking into account the multiple scattering in the detector material. A *compatible layer* on the strip detector is found based on the comparison of the distance of a hit to the trajectory versus the position uncertainty of the hit in that layer. The hit is compatible if it is within $n \times \sigma$ from the extrapolated trajectory, where n is taken to be 3 for the reconstruction in the analyses discussed here. The *compatible hits* are then determined by using the Kalman Filter. Adding the information of the compatible hits to the track improves the initial trajectory which was based on pure extrapolation, and the

procedure is repeated until there is no more unassociated hits left that are compatible with the trajectories.

3.1.5 Final track fit

After the association of all hits to the trajectory, a final χ^2 fit on the hits is performed, from which the track parameters are determined. This includes the track kinematics (based on the curvature in the magnetic field), and the quality variables, which quantify how confident the measurement of a specific track is. The uncertainty vales of the track p_{T}, and impact parameter are determined for each track, and used in the final track selection, discussed below.

3.1.6 Track selection in analysis

The algorithm returns the widest possible selection of tracks, with flexibility of further selection in the analysis level. Different types of analysis may be sensitive to the track efficiency and fake rates differently, thus there is always room for optimization. In the analyses discussed in this thesis, the track selection is based on the following variables and criteria:

- $N_{valid} \leq 13$: Number of valid hits on the track
- $d_0/\sigma(d_0) < 3$
  - d_0 : The shortest distance between the primary vertex and the track in transverse (xy) plane
  - $\sigma(d_0)$: The uncertainty on the d_0 of a track, where the uncertainty of the vertex position is also quadratically added
- $d_z/\sigma(d_z) < 3$
  - d_z : The shortest distance between the primary vertex and the track along the z axis

- $\sigma(d_z)$: The uncertainty on the d_z of a track, where the uncertainty of the vertex position is also quadratically added

- $\sigma(p_{\mathrm{T}})/p_{\mathrm{T}} \leq 0.1$: The uncertainty on the p_{T} of a track, normalized by the p_{T} of the track

The name of the tracking collection that results from the above selection and was used in all analyses discussed in this paper (except jet R_{AA}), is "hiGoodTightTracks". In jet R_{AA}, "hiIterativeTracks" were used.

3.1.7 Tracking performance

The performance of the "hiGoodTightTracks" is shown in figure 3-1. Important quantities are the overall tracking efficiency, which is a combination of algorithm efficiency and the geometrical acceptance of the detector, and the fake rate of tracks. The efficiency values are applied as inverse weights in the analysis to correct for the tracking inefficiency. The fake rate is also corrected for, in the same weighting procedure.

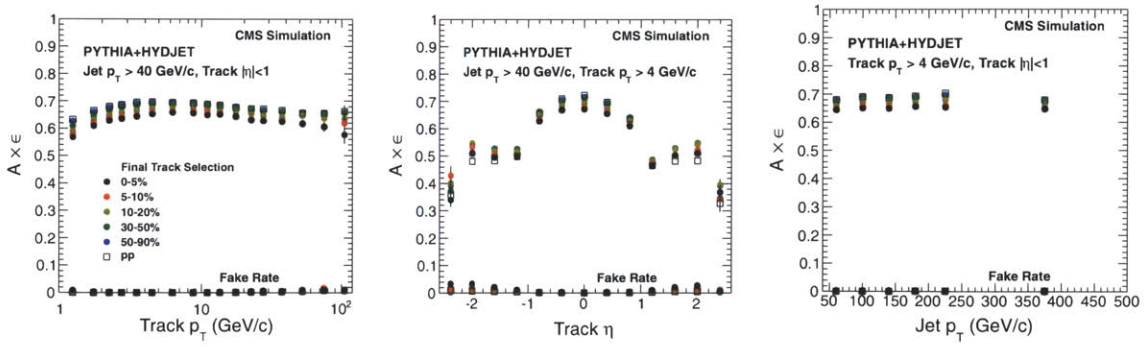

Figure 3-1: Tracking efficiency (topmost points) and fake rate (bottom points) for *HiGoodTightTracks*. The three panels show the tracking efficiency and fake rate a function of track p_{T}(left), $|\eta|$ (middle), and jet p_{T}(right) evaluated in PYTHIA+HYDJET.

The performance of tracking is determined from MC, therefore it has to be validated with data. The efficiency is validated by comparing track quality distributions in data and MC, before and after each cut involved in analysis. In addition, track

multiplicity distributions and correlations between calorimeter jets and particle-flow jets are studied as possible indicators of a misestimated tracking efficiency.

3.2 Calorimeter reconstruction

3.2.1 Ecal energy reconstruction and clustering

Although Ecal crystal cells are designed to match the *Moliere radius* of lead-tungstate, which is, the transverse size that contains a full shower of photon and electrons, many times the particles may not hit right the center of the cell and have their energy distributed over a wider region. The Ecal candidates are therefore constructed by clusters of crystals rather than individual cells.

3.2.2 Hcal energy reconstruction

The energy within the smallest $\eta \times \phi$ unit of detector, (combining all layers of the detector in HB, HE, and different-length fibers in HF) is summed up to form the Hcal *RecHits*. The hits are the main input to the ParticleFlow reconstruction, which will be described next. When the Hcal energy is also summed up with the corresponding 5×5 group of Ecal crystals, the candidates representing the total energy in that unit cell are called *CaloTowers*, which are the main input to the purely calorimeter-based version of the jet reconstruction. This reconstruction method is not vulnerable to tracking efficiency, however it suffers from a less precise energy determination compared to tracks. The jets obtained though pure calorimetry are evaluated to have a wider resolution compared to the ParticleFlow jets, discussed next.

3.3 Particle Flow algorithm

Although the calorimeters absorb the energy of hadrons completely, therefore are a good candidate for jet reconstruction, the non-linearity of the hadronic calorimeter limits the energy resolution of the reconstructed jets. Tracking can provide com-

plementary information on particles at each event, however this information is only useful if it does not introduce double-counting. The "Particle Flow" algorithm enables the optimal use of both calorimetry and tracking, by reconstructing single particle candidates from tracks and calorimeter energy deposits. Depending on the type of the particle, one piece of information can be preferred rather than other:

- **Charged hadrons** both leave tracks in the tracker, and deposit energy in the calorimeters. Since the track momentum resolution is in better quality than calorimeter energy resolution, one can use the tracking information only.
- **Photons** are the majority of the particles that deposit energy in Ecal. They can be identified with the absence of a track pointing to the center of the Ecal cluster.
- **Neutral hadrons** do not leave marks in either the tracker or the Ecal. Any energy left in the Hcal after subtracting the charged hadron contributions is assumed to be belonging to a neutral hadron.

The particle flow algorithm starts the reconstruction by connecting the various layers of detector inside out: Starting from tracks, it matches them to Ecal clusters and Hcal towers and then mathes Ecal clusters to Hcal towers. The connections between each reconstructed object are called *link*s. Depending on the energy fractions in each link, a set of links from tracks to Hcal towers are assigned a particle type, *particle-flow id*, and treated as a single particle. The energy of the particle is assigned based on weights and priority over the components it is made of, with the approach discussed above. Not all the Hcal energy is considered to be belonging to this particle, but rather an expected amount in the Hcal is subtracted, and the rest is left available for contribution to other particle candidates, for example to the neutral hadrons.

The calibration of weights, particle identification and energy subtraction are based on single particle studies with the pp data and simulations.

3.4 Jet reconstruction algorithms

3.4.1 Jet definition

As discussed in Section 1.2.3, the definition of the jets is very important for the clarity of the physics message that a certain measurement gives. The choice of the jet algorithm is driven by both the demands from the theoretical perspective and experimental conditions.

- The algorithm has to be fast enough to afford many iterations in a busy environment.
- The algorithm has to be infra-red and collinear safe, which allows to clearly define the object in theoretical study, due to issues discused in section 1.2.4.
- The background from the underlying event (discussed in the next sub-section) should be easy to quantify, which means a circular jet area with fixed size is advantageous.

The FASTJET package [57] provides a variety of algorithms, implemented in an efficient way [58]. Among these, the anti$-k_{\mathrm{T}}$ algorithm [59], is a popular and efficient one, satisfying the above requirements. It has been by far the most popular algorithm in recent analyses in RHIC, Tevatron and LHC.

The anti$-k_{\mathrm{T}}$ algorithm is a special case of the more general sequential recombination algorithm, which works as follows:

1. A set of candidates is defined (particles, or pre-merged towers).
2. A distance measure for each pair of candidates is defined as
   $d_{ij} = min(k_{T,i}^{2p}, k_{T,j}^{2p})\frac{\Delta_{ij}^2}{R^2}$
   where p and R are parameters of the algorithm, and Δ_{ij}^2 represents the distance between the candidates i and j in the rapidity-ϕ space (which can be approximated to be η-ϕspace for small rapidities and small masses).

3. Add the beam-candidate distances, $d_{i,B} = k_{T,i}^{2p}$ into the list of pairs constructed above.

4. Investigate the minimum element of the list:

   (a) If it is any $d_{i,B}$, define it as a jet an remove from the list.

   (b) If it is any $d_{i,j}$, remove the individual i and j from the set of candidates and add a merged candidate k into the set of candidates.

5. Restart the procedure from (1), until all candidates are converted into jets.

The choice of p = -1 is called the anti$-k_{\mathrm{T}}$ algorithm, which was invented after the k_t ($p = 1$) and Cambridge/Aachen ($p = 0$) algorithms. One can understand the inherent infra-red and collinear safety in the above formula:

- When the angular distance between two candidates approaches zero, d_{ij} diminishes and guarantees merging (and collinear safety).

- When either of the candidates is of very low-p_{T}, it has more priority to be merged with other candidates, thus eliminating sensitivity to soft radiation (and infra-red divergence).

What the peculiar p = -1 choice introduces is the priority given to the hard components to guide the clustering.

Although it is not entirely explicit in the procedure, the algorithm results in jets that are quite circular (as opposed to random) in shape in the η-ϕ plane(while $p = 1$ yields quite distorted shapes), and the radius of the circle is very close to R, unless the jet is composed of very low total p_{T} (a few GeV/c) that can only cluster a smaller region.

The R parameter of the algorithm is chosen to be 0.3. This is a rather small value compared to the jets that are used in pp analyses (R = 0.5, R = 0.7). Choosing a large radius is good for integrating more radiation effects and have a more direct correspondence to the parton involved in the hard process. Choosing a smaller value of R means the partons that we are analyzing correspond to a slightly later time

scale after the hard collision, therefore it may already contain more imbalance effects without the presence of any medium. However, in the PbPb measurement, the smaller radius has the advantage of being less vulnerable to the background fluctuations due to the underlying event. The resolution deterioration due to underlying event roughly scales with the area under the reconstructed jet, therefore R^2.

3.4.2 Background subtraction algorithms

In PbPb collisions, there is a high multiplicity of soft particles originating from processes that are not fully correlated to the single hard interaction we are interested in. Furthermore, the amount of this underlying event varies dramatically event-by-event, and so does its angular modulations. If we want to work with the jets in a way that relates them best to the parton in the hard scattering, we need to subtract this background contribution. This subtraction may be applied before or after clustering the jets. For either approach, certain issues have to be dealt with, although may differ in implementation:

- The background estimation should not be affected by the jets themselves.
- The angular modulations (in η and ϕ) of the background should be considered.

The analyses discussed in this thesis mostly use the so-called "Pile-up subtraction algorithm", which is a pre-clustering subtraction approach, with details in [?]. The procedure can be summarized as follows:

1. The ParticleFlow candidates are merged together in *towers* of unit $\Delta\eta$ and $\Delta\phi$, which is chosen to be same as the Hcal granularity since it is the coarsest of the components involved. 3-2
2. For each set of towers at a constant η, mean and variance of energy is determined. The sum of mean and variance corresponds to the estimated amount of background. In general, there can be a tuning factor multiplied with the variance term before adding. This factor is chosen to be 1 for the analyses discussed here.

3. The estimated background is subtracted from all towers. 3-3

4. The clustering algorithm (e.g. anti$-k_{\mathrm{T}}$) is run on the subtracted towers.

5. Excluding all towers within a chosen radius (0.5) around the jets (with a p_{T} threshold of 15 GeV) found in step 4, background is re-estimated. 3-4

6. Clustering algorithm is re-run over the final subtracted towers. 3-5

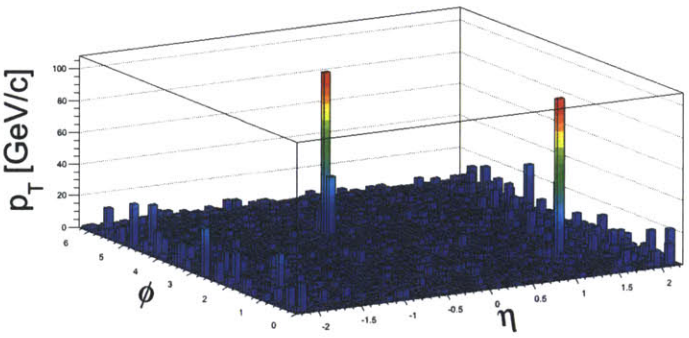

Figure 3-2: The ParticleFlow candidates are merged together in *towers* of unit $\Delta\eta$ and $\Delta\phi$, which is chosen to be same as the Hcal granularity since it is the coarsest of the components involved.

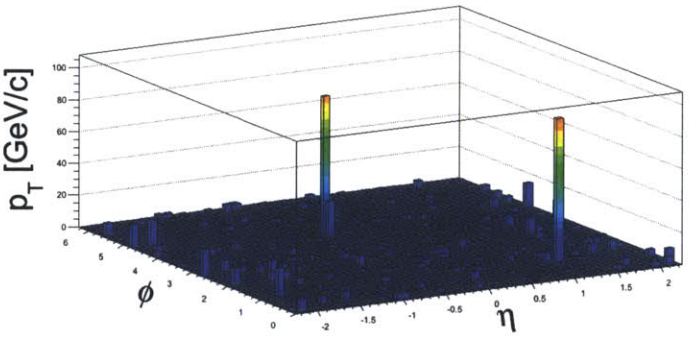

Figure 3-3: For each set of towers at a constant η, background level is determined. The estimated background is subtracted from all towers.

One should notice the algorithm has some important free parameters. The coefficient of standard deviation in background estimation is the first one, and it is driven

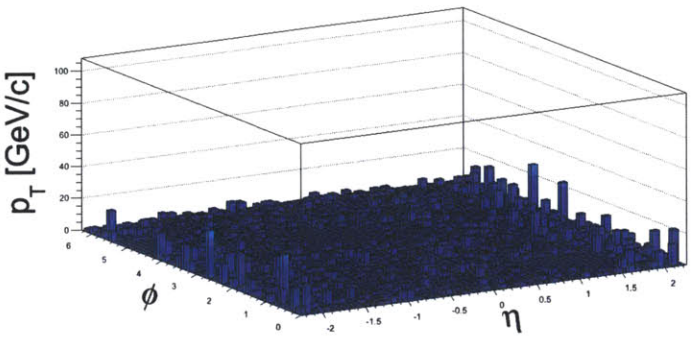

Figure 3-4: Excluding all towers within a chosen radius (0.5) around the jets (with a p_{T} threshold of 15 GeV) found in step 4, background is re-estimated.

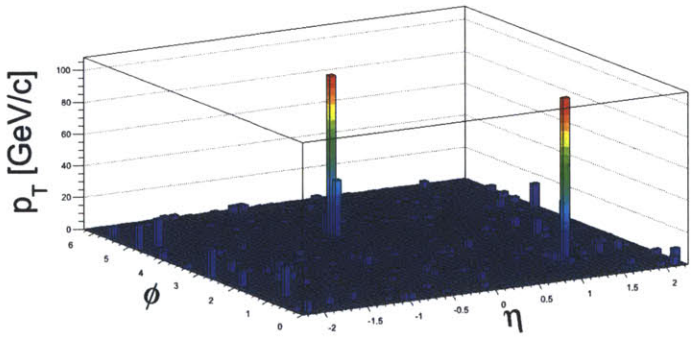

Figure 3-5: Clustering algorithm is re-run over the final subtracted towers.

based on calibration of average response in simulations. Other parameters are those related to the jet exclusion as of step 5. These are particularly important for low-p_{T} jet studies, in which background fluctuations can also fake jets, and the choice of the threshold can bias the energy of the jets. In this thesis we are concentrating on high enough jet-p_{T} values (>30 GeV/c) and avoid this problem.

Chapter 4

Jet energy scale and resolution

The jet energy scale and resolution, in addition to tracking efficiency, are the most important sources of systematic uncertainty in the measurements, therefore they deserve a detailed study of their values. As discussed later in the overview of results 7, one will see that the connection between a theoretical quantity and data is possible only with the knowledge of the performance parameters, which the results are folded or unfolded with.

The reconstruction performance of the CMS detector is extensively studied with a large effort [60], driven by various physics goals, including the search for the Higgs boson [61]. A significant portion of this calibration and performance study applies also to the reconstruction employed in PbPb studies, however, differences exist, which have to be additionally studied.

The important contrasts of the PbPb reconstruction and studies to pp are:

- Different center-of-mass energy
- Higher multiplicity environment
- Background subtraction in jet reconstruction
- Possible fragmentation differences

Some of these effects are only known based on the measurements of data, and they

are sources of systematic uncertainty. They can be improved as more measurements are performed.

4.1 Major factors in jet response and resolution

There are many factors involved in the resolution of jets in PbPb. Each of these factors may contribute in a different way, therefore it is necessary to evaluate each effect.

4.1.1 Calorimeter response

The calorimeter system consists of Ecal and Hcal, which have been described in 2.2 and 2.3. In the reconstruction of jets with Particle Flow method, Ecal is primarily used to determine the contribution of photons (and pi0s), and Hcal is used to determine the contribution of neutral hadrons, and charged hadrons that were not successfully reconstructed with tracking. Ecal is able to measure a single photon's energy with 5% precision.

The energy measurement of hadrons from a cascade in Hcal is not as precise as Ecal response to photons, due to the nature of the hadronic cascade involving lots of fluctuations in the particle composition of the final state.

4.1.2 Effects of tracking efficiency

The track efficiency has some effect on the jet p_{T} resolution, however in second order because missing a track in particle-flow is compensated by the calorimeter energy. The effect is estimated by analysis of fully simulated MC. This also relies on the validation of tracking efficiency in MC by comparing to data, as was discussed in ref-sec:trackefficiency.

4.1.3 Background fluctuations

The factors in jet response mentioned so far were generic for all collision systems. However, in the PbPb collisions, the large underlying event activity due to many soft interactions between the nucleons introduce a significant contribution to the jet response. Although the underlying event component is estimated event by event and subtracted from the measured jet's energy, it only contains limited information on the actual background fraction in a jet's energy, and there are finite fluctuations in the final jet response, that depend on the method of the background estimation and the nature of the underlying event. These fluctuations not only affect the response of a given jet, but it is also important to understand its effects in various multi-jet (e.g. dijet imbalance) measurements.

The jets in the PbPb collisions can be considered to be superposed with the underlying event, whose contribution to the jet would depend on the particles falling into the same cone. It is easy to estimate this amount from study of minimum-bias collisions, as done in later sections. In a simple approach, the fluctuations of this energy can be considered to correspond to the exact additional component of the resolution. However, the actual effect on the jet energy is not as straightforward measurement because:

1. The outcome of the jet algorithm is affected by the background before the jet axes are determined.

2. Jet reconstruction involves thresholds which have non-linear impact on background contribution.

3. Background subtraction effectively reduces the sensitivity to background contribution in lower energies, with the cost of systematic uncertainty in the energy scale.

For these reasons, the real effect of the fluctuations on the jet resolution should be estimated within the context of the algorithm, which is possible in studies of full simulation or data mixing. However, the accuracy of such methods gains confidence

with good understanding of the underlying event though direct studies of minimum bias collisions.

Multiple hard interactions

The events with the jets are biased towards more central events, where more binary nucleon interactions happen. It is also possible, that additional hard scatterings happen in the same PbPb collision. In such interactions, the scattering with higher momentum exchange is considered to be the primary interaction that this analysis measures, and the others are considered to be part of background contribution to the primary jets. Consideration of these events explains the non-gaussian nature of the background fluctuations that are observed in the various methods that estimate the jet resolution. The hard part of the fluctuations are investigated through analysis of Hydjet MC events, in which many hard nucleon interactions are overlaid on top of each other to simulate the underlying event in the PbPb collisions. One can keep track of the information of individual interactions, and these can be associated with the final jets observed in reconstruction. Study of data and MC with random cones also provides information of the hard part of the fluctuations, which is explained below.

4.1.4 Effects of quenching

The study of missing pT in asymmetric dijet events show that there is a finite excess of particles in a wide region in the hemisphere of the jet. Some of this excess also exists within the jet cone, and results in an extra soft component in the jet energy. Spectra of charged particles in jet cone for PbPb and pp dijet events are analyzed, and from their difference the amount of expected energy excess is estimated. This energy is estimated to be less than 1-2 GeV, and it is attributed to the systematic uncertainties regarding the jet energy scale.

The quenching can also affect the jet energy scale through any modifications in the fragmentation pattern. As discussed in Section 6.3.1, the fragmentation is

similar to pp collisions, and with studies of the detailed difference in pp and PbPb fragmentations, the possible effects on the jet energy scale is estimated to be 5%.

4.2 Estimation of Jet Energy Scale and Resolution in PbPb

As mentioned in the previous section, although the jet reconstruction in CMS pp studies is extremely well-understood, further studies are needed to test the additional effects that arise in the PbPb study. Here we will discuss the studies for validation of the energy scale and resolution, and determine the uncertainties that will be later reflected on analysis results.

4.2.1 Simulation studies

The energy scale, corrections and resolution are determined from fully simulated MC events. These events are generated by Pythia, and jet reconstruction is run on both the generator output particles, and on fully simulated and reconstructed particle-flow candidates.

Some useful definitions before starting the discussion:

- **GenJet** : The jet obtained by applying same jet algorithm on the gen-level particles in the MC event.
- **RecoJet** : The reconstructed jet after the MC event is fully simulated.
- ΔR : The distance in η-ϕ space, with magnitude $\sqrt{\Delta\eta^2 + \Delta\phi^2}$
- **Matching** : Correlating gen and reco level objects by checking compatibility $\Delta R < 0.3$
- **Matched GenJet** : Any GenJet that is matched to a RecoJet
- **Matched RecoJet** : Any RecoJet that is matched to a GenJet

- **Fake Jet** : Any RecoJet that is **not** matched to a GenJet
- **Missed Jet** : Any GenJet that is **not** matched to a RecoJet
- **Jet efficiency** : The ratio of matched GenJets to all GenJets in a given selection.
- **Fake jet rate** : The ratio of unmatched RecoJets to all RecoJets in a given selection.

The GenJets are assumed to represent the jets of all hadrons that appeared in the final state, whether or not being detected. The GenJets are in this view the right object to relate with the theoretical calculations. In some of the the studies in this thesis, the results are presented in reconstructed level, not being unfolded to the true GenJets. In such cases, the results have to be carefully interpreted by correctly modeling the reco-level observables.

Event embedding

An important aspect of the jet resolution is its vulnerability to the effects of the underlying event, which is of different amount in PbPb and pp. For this reason, in building the reference for the PbPb-MC comparison, the MC has to include the PbPb background, with the same centrality distribution.

The PbPb underlying event is generated by Hydjet, with the Drum tune that reproduces the observed data quite well [55]. The bulk properties of the medium are shown in figure 4-1. The background fluctuations are further studied in section 4.3.1. A different tune of the Hydjet, namely the Bass tune, has been used previously. This tune underestimates the multiplicity, and the uncertainties resulting from underlying event multiplicity can be studied by these different tunes.

It is difficult to generate a high-statistics sample of high-p_{T} dijets by running production of minimum bias PbPb events. Instead, a minimum bias sample is generated once, and to each event an additional hard scattering event, by Pythia, is superposed, with the proper cross section. The centrality distribution obtained this way is similar

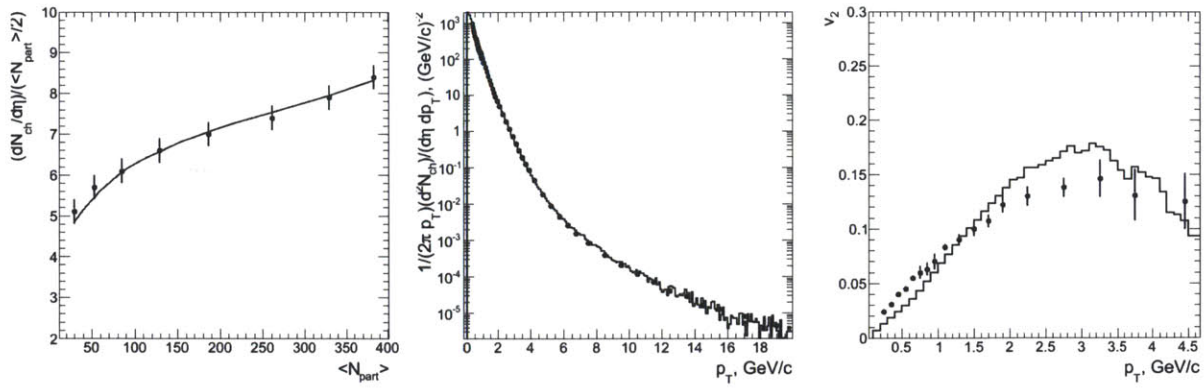

Figure 4-1: Performance of the Hydjet Drum tune, against data observed by Alice. From [55].

to minimum bias, whereas the jet sample displays a bias towards more central events due to the relatively higher number of hard collisions in more central events. The MC sample is then reweighted as a function of fractional cross section (in 40 bins of 2.5%), to achieve the realistic distribution.

The jet performance estimated from embedded MC studies is summarized in the figures 4-2 and 4-3.

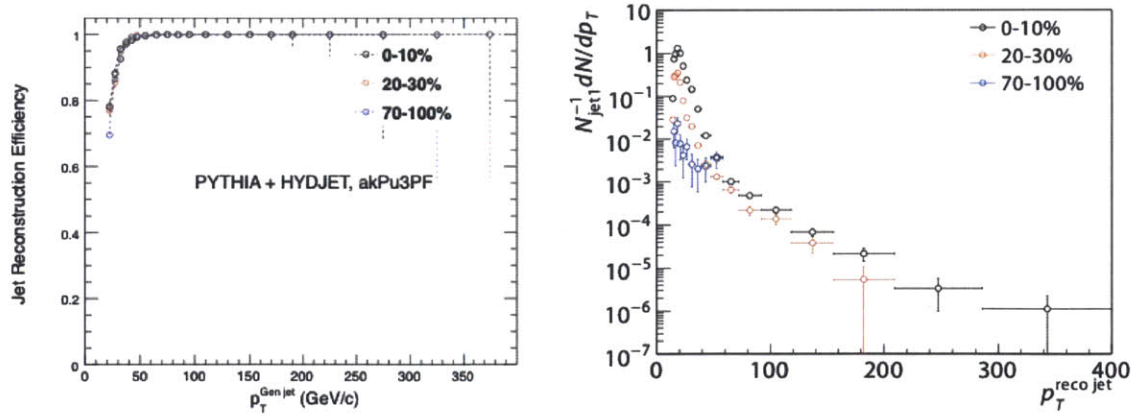

Figure 4-2: Left: Inclusive jet efficiency in different centrality bins. Right: The rate of fake jets per selected leading jet.

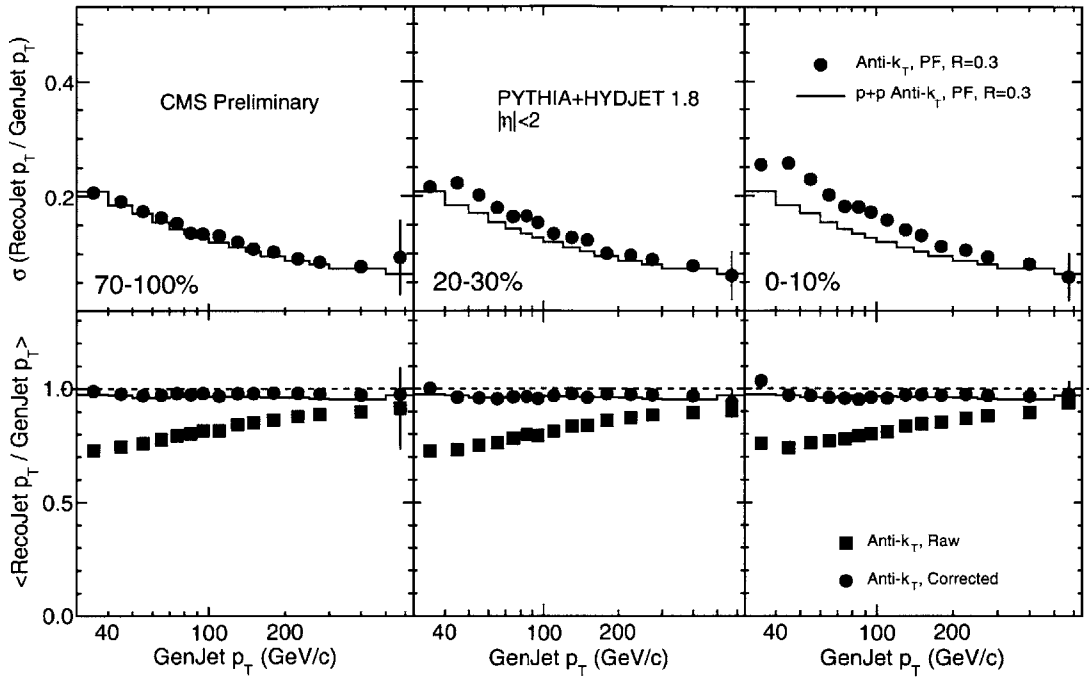

Figure 4-3: Top row shows the jet p_{T} resolution for different centralities, compared to pp. One can see that as a result of the underlying event fluctuations, the resolution deviates from pp in high centralities. Bottom row shows the jet p_{T} scale for both uncorrected and corrected jets. Due to some inefficiency of jet reconstruction at lowet p_{T} values, sampling the high-fluctuated values of p_{T} introduces a kink in p_{T}-scale and resolution, which is treated separately in systematics.

Jet energy corrections and uncertainties

The raw sum of the candidates that make up a jet, represents only a fraction of the total energy that belongs to the GenJet. This amount should be corrected to yield the right value in average. The corrections are obtained by comparing the p_{T} of the matched RecoJet-GenJet pairs, in simulations of Pythia events. The corrections are derived as a function of p_{T} and η. In the case of particle-flow jets, most of the jet energy is successfully detected by the tracker and the calorimeter, and the correction needed to calibrate the average energy to 100% is about 30-10%, decreasing with jet p_{T}, as can be seen from the response of uncorrected and corrected jets in figure 4-3. The corrections are an important source of uncertainties, therefore minimizing the amount of necessary correction is one of the main goals of the reconstruction method.

The uncertainty on the jet energy scale is determined by combining various sources. First of all, the uncertainty that is quoted for the pp reconstruction (1.5-3%) [60] is taken to be the base value which PbPb uncertainties are added on top of. These additional effects include the missing residual corrections for PU subtraction effects, and the fragmentation related effects on the energy scale, which have an effect of about 3%.

Jet resolution parametrization and systematics

The jet resolution parameters for a specific study, namely the photon-jet correlations [8], has been published along with the paper. These numbers may be used by theorists to translate their calculation to detector-level observables, as will be discussed in section 7. The values in various PbPb centralities and pp data, are summarized in table 4.1.

The jet resolution can be considered to consist of different independent components, which add up quadratically as :

$$\sigma\left(\frac{p_{\mathrm{T}}^{\mathrm{Reco}}}{p_{\mathrm{T}}^{\mathrm{Gen}}}\right) = C \oplus \frac{S}{\sqrt{p_{\mathrm{T}}^{\mathrm{Gen}}}} \oplus \frac{N}{p_{\mathrm{T}}^{\mathrm{Gen}}}, \tag{4.1}$$

Table 4.1: Parameters of the functional form for the jet energy resolution $\sigma\left(p_{\mathrm{T}}^{\mathrm{Reco}}/p_{\mathrm{T}}^{\mathrm{Gen}}\right)$ given in Eq. 4.1, obtained from GEANT4 simulation of PYTHIA pp jets and from PYTHIA jets embedded in HYDJET events for various PbPb centralities (indicated by the % ranges in parentheses). The units of S are $\sqrt{\mathrm{GeV}/c}$ and the units of N are GeV/c. From [8].

C	S	N (pp)	N (50–100%)	N (30–50%)	N (10–30%)	N (0–10%)
0.0246	1.213	0.001	0.001	3.88	5.10	5.23

The different terms in this parametrization represent different experimental effects, and it is important to know their physics origin when examining the systematic effects due to uncertainties in resolution.

- **C)** *constant term*: This term represents the resolution from p_{T}-scaling noise

effects, such as those from read-out, or tracking efficiency; as a constant fraction of the p_{T}. It is almost negligible for the p_{T} ranges populated in this analysis.

- **S)** *sampling term* (or *stochastic term*): This term is governed by the shower fluctuations in the calorimeter, in addition to the fluctuations in the p_{T} profile of the hadron clusters.

- **N)** *noise term*: This term represents the fluctuations in the underlying event, and pile-up if there is any. Even though background subtraction does a good job, eliminating the energy-scale to shift under influence of underlying event; fluctuations of the background density contributes to the resolution of the jet. in the PbPb collisions, this is the centrality-dependent part of the resolution, which gets significantly large value (up to 5-10 GeV depending on the jet definition).

The assumption of independence of these terms is may be fragile. For example, the amount of background fluctuation that a jet is susceptible to may depend on the fragmentation of the jet, which correlates S and N terms. Therefore the effort was put in measuring the combination of all effects with embedded simulations, rather than individual components. Terms above are used as a guide in fitting the full resolution, therefore they are good enough for applications.

4.3 Study of Background with Minimum Bias PbPb Collisions

In order to rely on the reconstruction performance results obtained from embedded MC studies, it is important to make sure the underlying event background is described in these simulations accurately. With this motivation, the properties of the minimum-bias events are studied extensively. The underlying event properties can be quantified by multiplicity distributions and $dN/d\eta$ [62, 63], two-particle correlations [64], elliptic flow [65, 66] and other methods. In this section, we will look at a particular study that aims to quantify the local fluctuations of the underlying event, which is important in understanding jet resolution.

4.3.1 Random Cones

In order to validate the MC description of local fluctuations that may influence the energy determination in the cone of the jet, a study on minimum bias events is performed, where cones are randomly placed at different angles in minimum bias events, and the energy within these cones are summed up. The distributions of the random cone energies are compared to those obtained from MC, shown in figure 4-4.

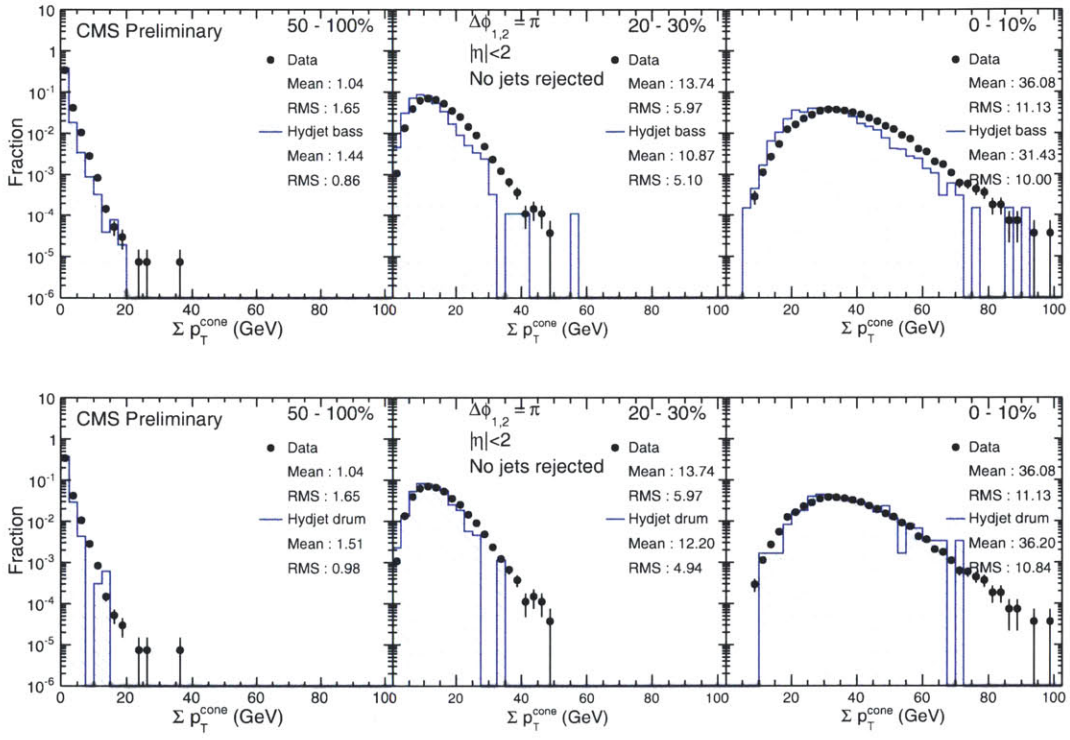

Figure 4-4: Total p_{T} of the particle flow candidates in a cone around a randomly determined axis, for various wide centrality bins. The top row is results in various centrality bins for the Hydjet 1.6 (Bass) tune, whereas the bottom row shows the results from Hydjet 1.8 (Drum) tune, which is much more consistent with the data.

Back to Back Random Cones

The fluctuations in the background do not always happen independently. The effects such as elliptic flow or higher order angular correlations (which our background subtraction procedure cannot resolve) introduce an angular correlation of fluctuations

within an event. In the dijet analysis, the jet selection is constrained to well aligned jets in azimuth, for which these correlations would be significant. In order to evaluate the correlated amount of the fluctuations, two random cones are placed in each minimum bias event, however the second one only being random in eta, but in phi being exactly anti-aligned with the first one. The results for the sum and difference of the back-to-back cone energies are shown in figure 4-5.

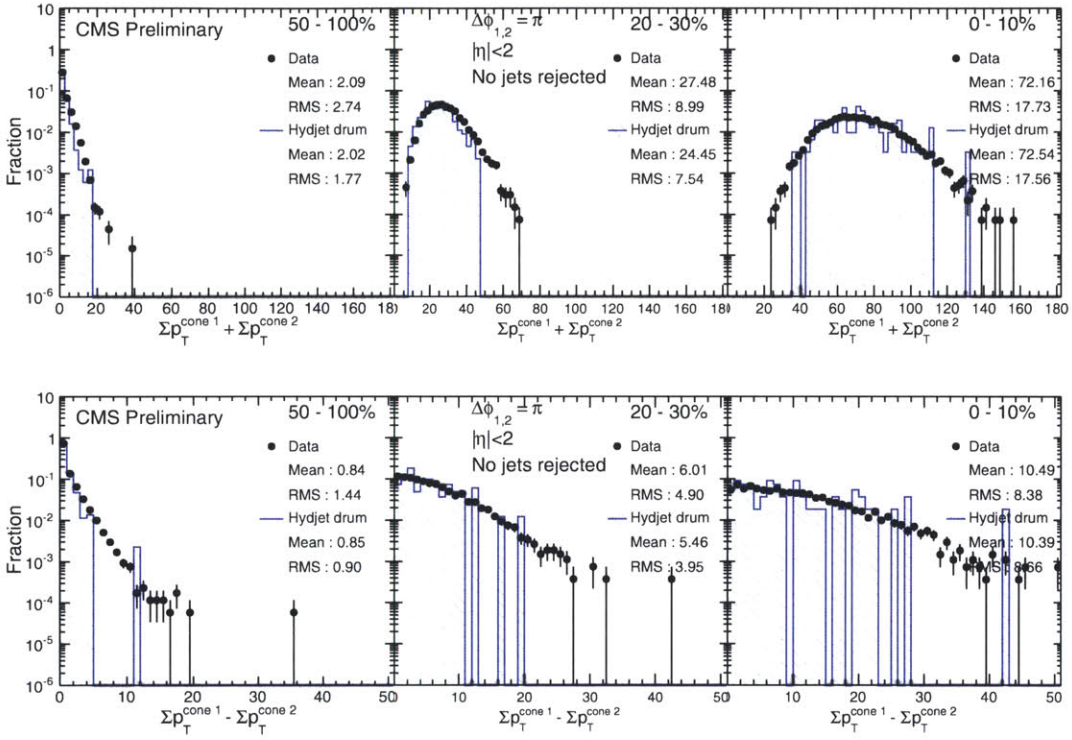

Figure 4-5: Top : The distributions of the p_{T} sum of two back-to-back random cones. Bottom : The p_{T} difference of the back-to-back cones.

As a conclusion of the random cone tests, Hydjet 1.8 tune, which our reference is based on, is shown to reproduce the effects of the background reasonably well. By a comparison of various background tunes and also the absence of background, the systematic uncertainty on the dijet imbalance is estimated. For the dijet imbalance variable $\langle p_{\mathrm{T},2}/p_{\mathrm{T},1}\rangle$, the uncertainty is about 5% (which is a shift of 0.03 when the $\langle p_{\mathrm{T},2}/p_{\mathrm{T},1}\rangle$ is 0.6) in the 0–10% centrality bin.

Chapter 5

Centrality determination

The Pb nucleus is a *large* object. What we mean by large is that, the nucleons are distributed in a volume (of radius ~10 fm) that is many times the size of the individual nucleon (~fm). In such case, not all nucleons participate in every interaction. Also, the nucleus is not a rigid body, the nucleons, having some non-zero momenta, may be found at any location. In addition to the complication above, the data sample of PbPb collisions includes interactions at all impact parameters, as in figure 5-1. Therefore, a collision between two nuclei may have happened in many different configurations. The procedure of estimating the average nuclear configuration properties in a given set of events is called *centrality determination*, which is the most important ingredient in all heavy-ion collision studies. The importance comes from many factors:

- The medium density is higher in more central events, therefore medium-related effects are most enhanced.
- The average medium shape depends on the centrality of the collision
- The final state particle multiplicity is higher in central events, therefore experimental performance may be affected differently.

The important quantities of the initial-state of the two nuclei are the following :

- Number of participating nucleons : N_{part}
- Number of binary collisions between nucleons : N_{coll}

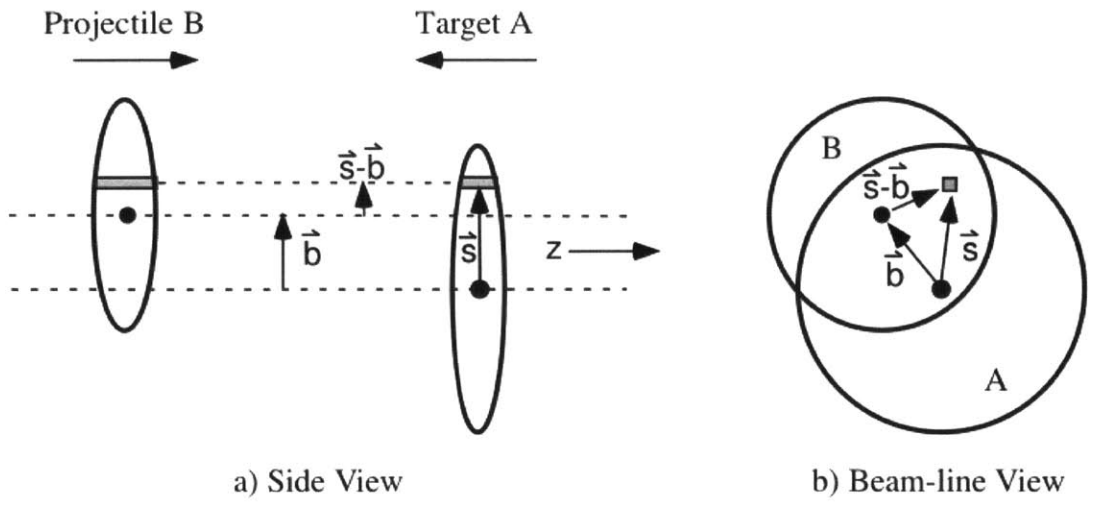

Figure 5-1: Illustration of the overlap between two colliding nuclei, parametrized by the impact parameter $\vec{b}$ defined as the transverse vector between the centers of the nuclei. The nuclei are described by a Wood-Saxon distribution around the nucleus, as a function of the vectors $\vec{s}$ and $\vec{s} - \vec{b}$ for nuclei A and B respectively.

- The impact parameter of the collision (distance between the centers of the two nuclei) : b
- The event plane angle (The direction of the minor-axis in the elliptic density profile of the participating nucleons) : Ψ

Rather than treating the nuclei as perfect spheres (or lorentz-contracted pancakes) and analytically calculating the overlap, a MC method which computes nucleon-by-nucleon overlap for each collision gives a better description of the collision. The nucleons are placed around each nuclei according to a Woods-Saxon potential, and for each event they are placed randomly on the transverse plane, as in figure 5-2. This so-called Glauber model as implemented in [67] represents the N_{part} and N_{coll} distributions to a good extent, also able to exhibit fluctuations, as shown in figure 5-2. These fluctuations have been shown to have importance for flow studies [46], and it is potentially of similar importance to jet quenching.

In addition to these numbers characterizing the initial state, the nucleons that do not participate in the collision, called *spectators*, are also interesting, as their energy

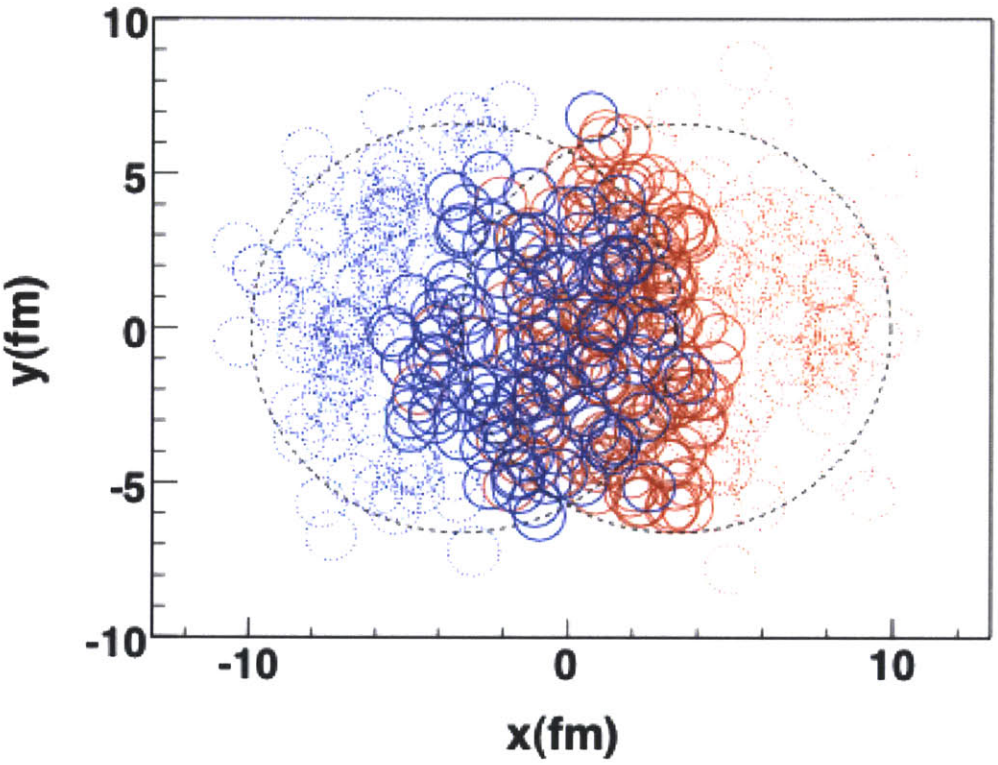

Figure 5-2: The nucleons from nuclei A (blue) and B (red) placed randomly around the nuclear center. The overlapping nucleons are determined by their geometric overlap, based on the inelastic NN cross-section.

can be measured by the ZDCs 2.3.4.

In the following sections, we will discuss both the experimental and physics aspects of the centrality determination procedure.

5.1 Method

It is not experimentally possible to count and locate the individual nucleons in each event. The approach is, to determine a specific selection of events, and estimate the average properties of those events based on some initial state model (the PHOBOS Glauber [67] model in this case). In order to do this, one has to choose an experimentally observable variable, which correlates well to the centrality of the collision, with a monotonic relation [68]. The event multiplicity, or energy in a chosen detector region, represents such a variable, since in more central collisions (greater N_{part}) there is a larger number of particles produced. Figure 5-3 shows the correlation of number of pixel hits at mid-rapidity, to the forward (HF) energy. In the studies discussed in this thesis, the centrality determination is performed by using the total transverse energy in the HF detectors, which are at the forward pseudorapidities ($3 < |\eta| < 5$). The reason for using forward detectors is to remove auto-correlation effects when analyzing the jets at mid-rapidity ($|\eta| < 2$).

Once the total E_T in the two sides of the HF detector is summed up, the data sample of minimum-bias events is sorted in this variable, and split into fractions of equal cross-section. The model calculations are also split into the same cross-sectional fractions, which are called *centrality classes*, or more commonly, *centrality bins*. The convention is to quote the fractional value in terms of the percentage, e.g. 0–10%,10–20%,20–30%, etc... It is important to remember that the smaller percentage corresponds to more central events (greater N_{part}).

In the analysis of MC events, which are obtained by embedding Pythia events into minimum bias Hydjet events, the centrality distribution has match the centrality in data, therefore the sample is reweighted by the distribution for selected dijet events shown in left figure of 5-4.

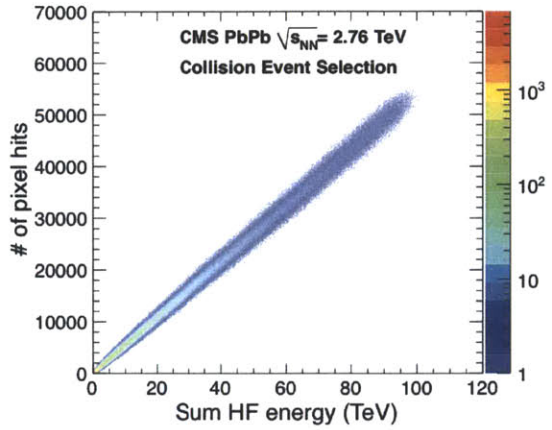

Figure 5-3: Correlation between the total HF energy (in the forward rapidities) and the number of hits in the pixel detector (at mid-rapidity). The strong correlation between the particle production at the two rapidity regions imply that the sample after selection consists of hard nuclear interactions and it is clear of background events.

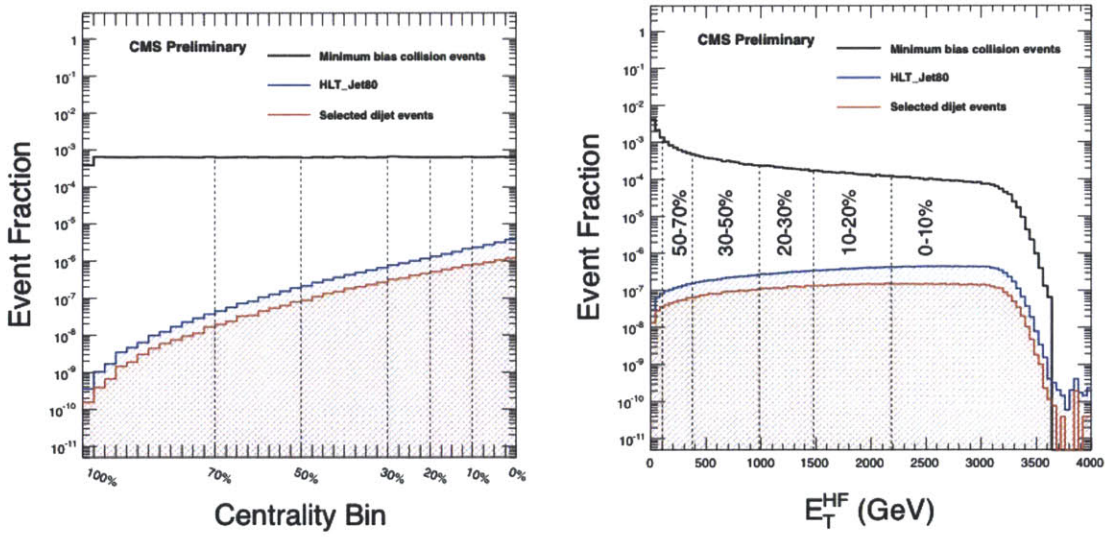

Figure 5-4: Left : Distribution of centrality percentage, which is a flat line by definition for minimum-bias sample (except the inefficiency at most peripheral bin), compared to the distributions from jet-triggered sample and offline-selected dijet sample, where a bias towards more central events is observed. Right : The distribution of the centrality variable, total E_T in HF, for the various samples.

5.2 Detector resolution effects

The reconstructed energy in the detector is only an approximate estimation of the real energy produced in the collision. Also, the number and energy of the particles for a specific N_{part} may fluctuate from collision to collision, adding a factor of resolution in the estimation of the N_{part} based on the observables. In order to account for these effects, the model calculation is modified to include similar amount of fluctuations. This is done by a two level smearing procedure, based on correlation matrices obtained from full simulations of Hydjet and AMPT. First, the amount of particle energy for a given N_{part} is estimated, and then the amount of reconstructed HF energy is estimated for a given amount of particle energy. The correlations involved in the procedure are illustrated in figure 5-5.

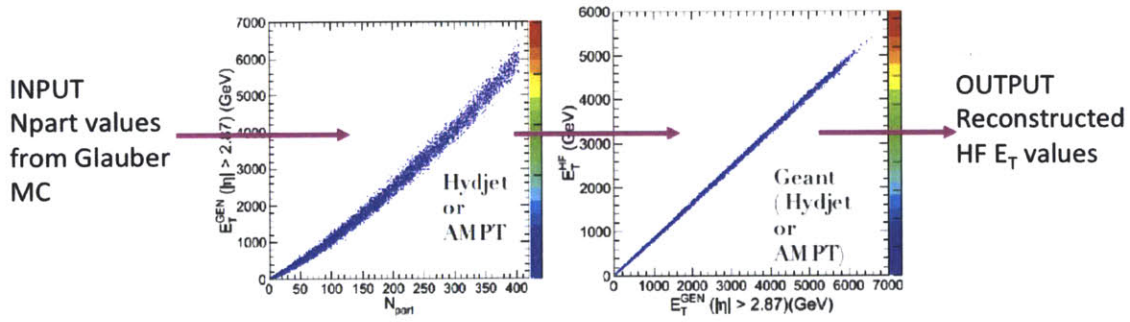

Figure 5-5: Summary of the smearing procedure applied to the standalone Glauber calculations. The N_{part} values from the Glauber calculation are first translated into particle-level E_T, then this is smeared to emulate the reconstructed E_T values in the HF acceptance.

The model calculation is then classified into centrality bins based on the smeared variable, making the comparison consistent across data and the model.

Chapter 6

Analysis of jets

We have introduced jets as good observables for probing hot and dense QCD dynamics, and then described the experimental methods to detect them and analyze. What is next is to examine the behavior of the jets, their kinematics and correlations, in PbPb collisions and compare the results to pp. The differences in jet behavior in different types of collisions, are considered to be a reflection of the effects due to the medium that is present in the PbPb collisions.

The 2011 pp data statistics have been limited for the parts of the analysis where very high-p_{T} reach is needed. For the imbalance study, a MC sample, based on Pythia and Hydjet, is used as a reference, and it is also compared with pp data.

The trigger system of the CMS detector introduced in section 2.5.1, has been quite successful collecting all high-p_{T} jet events that occurred in PbPb and pp runs very efficiently. This provided us of more than 50 thousand events with a high-p_{T} jet in 2011 PbPb data, as will be seen in table 6.2.

In this chapter, we will describe the analyses that examine the behavior of these jets, in particular the correlations of the dijets. The probability of a jet to be fully absorbed in the medium, azimuthal correlations between the jets, and their momentum imbalance are studied. In addition, we will briefly go through the observations from inclusive jet R_{AA} and jet fragmentation studies, however will not discuss their systematics in full detail.

6.1 Event selection

6.1.1 Types of background events

The analysis is interested in a rare type of events, which can be easily contaminated by non-collision signals that mimic jet events. These contaminations can be eliminated based on the different topologies of these events.

Electromagnetic and diffractive collisions

These events leave large deposit in the forward calorimeters, sometimes only on a single side of rapidity. Requiring large enough energy in the both sides of HF and a reconstructed vertex controls this background.

Beam-scraping events

These events have a large multiplicity in the pixel detector, mostly with appearing as a sequence of hits in a fixed ϕ position. The distinguishing property of these events is that the hits do not point back to a vertex within the detector. The *cluster-vertex compatibility* (described in the next subsection) is useful to eliminate these events completely.

Cosmic muon events

The chances of these to be associated with a primary vertex is very low.

Beam-halo events

These events are cleaned out based on the timing of the BSC coincidence. A large time difference (73 ± 20 ns), between the signal from two detectors on the opposite sides of the interaction point, means that the particles do not originate from the interaction point, and these events are rejected.

Calorimeter noise events

As discussed in the sections 2.2 and 2.3, there are various type of noise events in certain calorimeter systems. The term "noise" in this discussion does not refer to the low energy fluctuations (which are instead dealt with in reconstruction performance 4.1), but rather to large and rare signal pulses due to interaction of the particles with the readout systems of the detectors. Depending on the type and installation of the read-out, the noise events can show different characteristics. These methods are already developed for pp studies [69], and optimized further for PbPb studies.

The types of noise events related to calorimeters are:

- **HPD noise :** The channels all from the same HPD may contain a large pulse synchronously, and this may look like a high energy deposit along a strip of several towers.

- **Read-out box noise :** This happens when all channels connected to the same RBX suddenly exhibit high signal, which can be identified as a large set of high energy towers in a large rectangular region.

- **PMT hits in HF :** The PMTs are designed to pick up Cerenkov radiation in quartz fibers, however they are vulnerable to radiation from particles that hit the PMT window.

- **Ecal spikes :** These are high single crystal signal events, which are due to noise inside APDs of the Ecal Barrel. They can be cleaned out by the so-called swiss-cross cut, which acts on the ratio of energy in the spiky crystal to the neighboring four crystals. The real photons actually occupy a larger area with their shower, therefore can be separated. The cleaning of the spikes happen within the reconstruction.

These events can fake jet events, or show up as an additional jet in an event with already a real jet. They should be cleaned out of the data sample, as described in section 6.1.2.

6.1.2 Event selection criteria

Although the event selection procedures in analyses of PbPb and pp differ slightly in order to maximize the signal in a different multiplicity/luminosity/background environment, they consist of common main elements. Table 6.2 shows the number of events in the sample after each selection.

HLT path

To accommodate for the LHC runs of different beams, with different luminosity and backgrounds, the L1 and HLT menus are re-implemented each time. The HLT paths used in various data acquisition periods are summarized in table 6.1.

Table 6.1: HLT paths

Sample	HLT path	analysis
2010 PbPb	HLT_HIMinBiasHfOrBSC	minimum bias physics
2010 PbPb	HLT_HIJet50U	high-p_{T} jet physics
2011 pp	HLT_HIMinBiasHfOrBSC_v1	minimum bias physics
2011 pp	HLT_HIJet80_v2	high-p_{T} jet physics
2011 PbPb	HLT_HIMinBiasHfOrBSC_v1	minimum bias physics
2011 PbPb	HLT_HIJet80_v2	high-p_{T} jet physics

Cluster-vertex compatibility

As discussed in section 3.1.1, the length of the pixel clusters specify the orientation of the track, and this information can be used to distinguish events in which many hits do not come from the same vertex, such as the beam-scraping events, as a result of collisions far from the interaction point. Similarly, the cluster-vertex compatibility variable is defined as the ratio of number of clusters that are compatible with the vertex to the number of clusters that are compatible with a 10 cm displaced vertex. Events where there are many pixel hits that are not correlated with the vertex have a small value of this variable. More details are on cluster-vertex correlations are in [51]. Figure 6-1 shows the correlation of cluster vertex compatibility and number of pixel hits, and the beam-scraping cut.

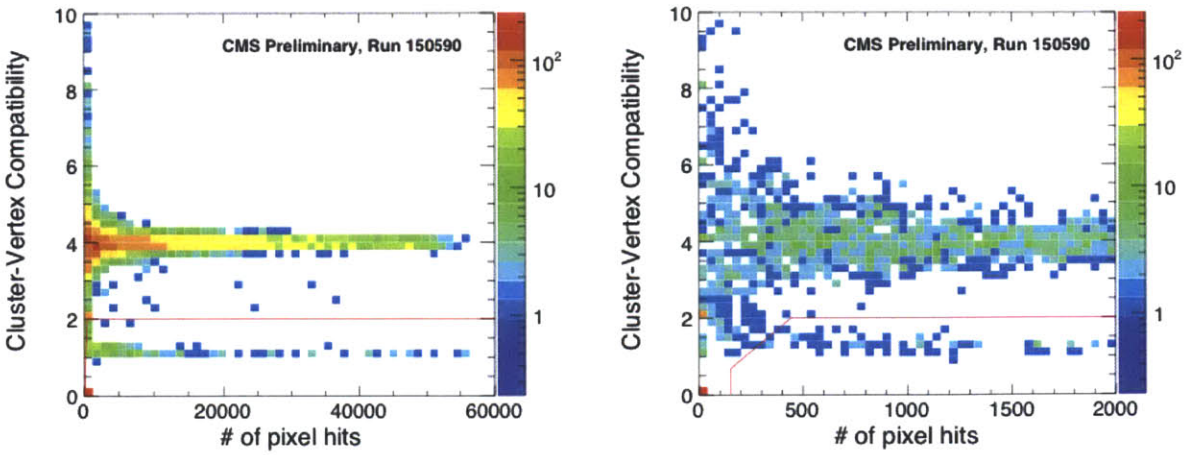

Figure 6-1: Correlation of cluster vertex compatibility and number of pixel hits, and the beam-scraping cut.

Vertex reconstruction

The vertex reconstruction methods have been introduced in section 3.1.2. In the analysis, the events are required to have a vertex reconstructed within $-25 < z < 25$, with at least two good-quality tracks attached.

HF coincidence

In this analysis, the sample to be collected is the set of collisions with full nuclear overlap. The UPC events are cleaned out of this sample, by requiring a coincidence of HF detectors on both sides of pseudorapidity. Events are required to have at least three towers with a reconstructed energy of 3 GeV on each side of the HF. In the case of pp analysis, the requirement is loosened to be satisfied by either side, to collect the biggest fraction of non-single-diffractive (NSD) events.

Hcal noise cleaning

A non-collision event sample is obtained by reversing the HF-coincidence and vertex requirements. The cuts for the various types of Hcal noise (as discussed in section 6.1.1) are optimized based on study of this noise enriched sample. Comparing the

Table 6.2: The effects of various selections applied to the data sample. In the third column, the fractional values are with respect to the line above and in the fourth column they are with respect to the triggered sample. The selections are applied in sequence.

Selections	Events remaining	% of previous	% of triggered
Jet triggered events ($p_{\mathrm{T}}^{\mathrm{corr}} > 80$ GeV/c)	369 938	100.00	100.00
Offline collision selection	310 792	84.01	84.01
HCAL and ECAL noise rejection	308 453	99.25	83.38
Leading jet $p_{\mathrm{T},1} > 120$ GeV/c	55 911	18.13	15.11
Subleading jet $p_{\mathrm{T},2} > 30$ GeV/c	52 694	94.25	14.24
$\Delta\phi > 2\pi/3$	49 993	94.87	13.51
Track within a jet	49 054	98.12	13.26

behaviors (total number and energy) of HPDs and RBXs, cuts that are safe enough for real collision events are determined.

Jet quality with track content

To further limit the possible remaining calorimeter noise contamination, the high-p_{T} jets are required to have at least one track with $p_{\mathrm{T}} > 4$GeV/c. In the dijet analysis, it is sufficient for for an event to have either of the two jets to satisfy this criterion. This cut removes a very small fraction of events, after the above selection, and these events are checked in event-displays to be indeed of an Hcal noise type appearance.

6.2 Dijet azimuthal correlations and momentum imbalance

In a hard parton scattering, the momentum in the transverse direction, is conserved, which, after some distortion due to radiation, results in two jets, back-to-back in ϕ and of similar p_{T}. When the scattering happens in medium, the momenta of the partons may be affected differently and may result in less correlated jets. The p_{T} balance and the ϕ correlations might be changed. To measure these effects, the azimuthal correlation based on $\Delta\phi$, and the momentum balance, $x = p_{\mathrm{T},2}/p_{\mathrm{T},1}$, are studied [5], for a selection of dijet events. The rate of losing the subleading jet (see 6.2.1) is also measured.

6.2.1 Dijet selection

The dijet analysis [5] is performed with a selection of events in which reconstruction driven uncertainties are under best control, which means highest possible p_{T} ranges, since most of the problems reside at the low p_{T} where background effects get more significant. With the large dataset available from the 2011 LHC run, we already have a large range in jet p_{T}, available for splitting into bins. We characterize the dijets mainly in terms of the leading jet p_{T}, as defined below. In this analysis, the effective acceptance for the jets is $-2 < \eta < 2$, because only the jets that are completely within the tracker coverage are considered in analysis. This does not have a significant effect since the high-p_{T} jets in the forward region are very rare. The selection of dijet pairs can be summarized as follows:

- Leading jet : We start selecting the dijet events by first requiring the highest p_{T} jet in the event to be at least 120 GeV/c. The kinematic variables for the leading jet are denoted with subscript 1.

- Subleading jet : Then we select the second highest p_{T} jet, with a minimum p_{T} requirement of 30 GeV/c. The events in which there is no second jet with p_{T} 30 GeV/c are considered only in the analysis of matched dijet and background frac-

tions, as will be discussed in the next two subsections. The kinematic variables for the subleading jet are denoted with subscript 2.

- $\Delta\phi_{1,2}$: The angular correlation of the two jets is examined. If the jets have an azimuthal angle difference, $\Delta\phi_{1,2}$, of greater than $\frac{2}{3}\pi$, these are considered *back-to-back* and selected as the dijets for analysis. The other jets are used in the $\Delta\phi_{1,2}$ analysis and in background subtraction.

The momentum ratio of the two jets, $p_{\mathrm{T},2}/p_{\mathrm{T},1}$, is denoted x and used to probe the different amount of energy loss in the jet momenta. Another variable, $A_J = \frac{p_{\mathrm{T},1}-p_{\mathrm{T},2}}{p_{\mathrm{T},1}+p_{\mathrm{T},2}}$, is also used in some references. It has been traditionally used in jet resolution studies, however, in presentation of quenching phenomena, the variable $x = p_{\mathrm{T},2}/p_{\mathrm{T},1}$ is preferred.

6.2.2 Reference distributions

In the analysis of dijet imbalance [5], a simulated Pythia (Z2) sample is used as a reference representing the vacuum behavior. The dataset of pp events at $\sqrt{s}$ = 2.76TeV was also analyzed, to compared with peripheral PbPb data. Although the pp data is a more reliable reference than MC, the analysis relies on high statistics at high p_{T}, for which the pp dataset at the same $\sqrt{s}$ was too small at the time of the analysis, therefore the Pythia sample is chosen to be the primary reference. In order to include the effects of the PbPb underlying event in the reference, the Pythia events are embedded in a sample of minimum bias Hydjet simulations. The details of the MC reference have been discussed in section 2.5.3. As mentioned there, the MC is re-weighted so that it has the same centrality distribution as in data. This is to account for the fact that, the sample of jet-triggered events have a natural bias towards more central events where there are more binary interactions per nuclear collision.

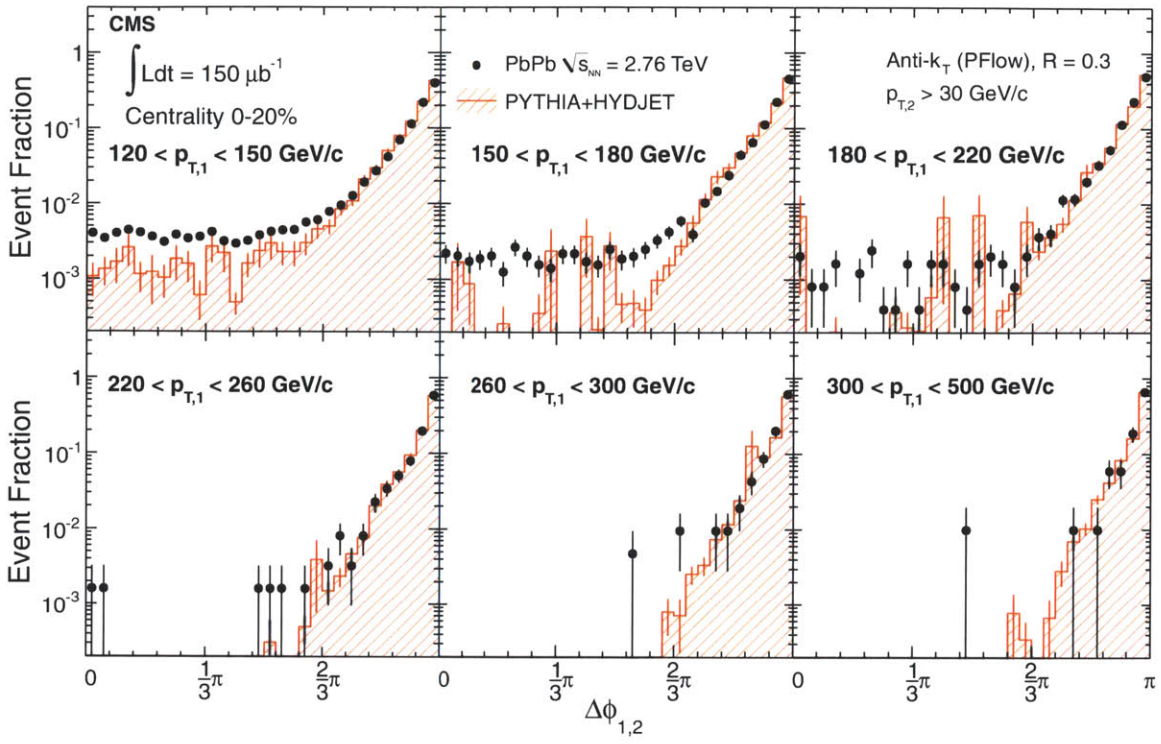

Figure 6-2: Distribution of the angle $\Delta\phi$between the leading and subleading jets in bins of leading jet transverse momentum from $120 < p_{\mathrm{T},1} < 150$ GeV/c to $p_{\mathrm{T},1} > 300$ GeV/c for subleading jets of $p_{\mathrm{T},2} > 30$ GeV/c. Results for 0–20% central PbPb events are shown as points while the histogram shows the results for PYTHIA dijets embedded into HYDJET PbPb simulated events. The error bars represent the statistical uncertainties. From [5]

6.2.3 Azimuthal correlations of jets

In the dijet selection, no requirement is imposed on the angular configuration of the two jets. When the azimuthal correlations are examined by $\Delta\phi_{1,2}$ distributions as shown in 6-2, one observes two aspects to this correlation. First of all, the distributions peak at π and the distribution in this region is very similar in data and the MC. This is in fact an important observation: As we will see in next subsection, there is a significant p_{T}-loss in the jets, however, not with an equivalent deflection in angle, which has implications on the radiation pattern [70], suggesting that the lost energy cannot be dominantly in form of hard large-angle radiation.

Another observation in $\Delta\phi$ distributions is, there is a roughly constant offset, particularly in low-p_{T}, high centrality bins, with different amounts in data and MC.

This is likely due to the background jets replacing the genuine subleading jet from the hard interaction.

6.2.4 Background jet pairs and subtraction

In the later analysis, we are trying to correlate the jets that are produced in the same hard partonic interaction, among many that occur in a single nuclear collision. Due to the presence of additional partonic interactions and a certain amount of soft background, we may sometimes be correlating the leading jet to another fake or real jet that is initially uncorrelated. Since the independent partonic collisions and the background fluctuations can happen at any ϕ, the $\Delta\phi_{1,2}$ component resulting from this is roughly flat. A higher order consideration of this background should involve the bias due to the effects of flow on the jets, as was discussed in ??.

The contamination from correlations of leading jet with the background can be estimated and subtracting with the events in which dijets have large $\Delta\phi_{1,2}$. In order to obtain imbalance results that will be discussed next, the imbalance in events with $\Delta\phi < \pi/3$ is also plotted, and subtracted from the result obtained from the signal selection, $\Delta\phi > 2\pi/3$, as shown in figure 6-3.

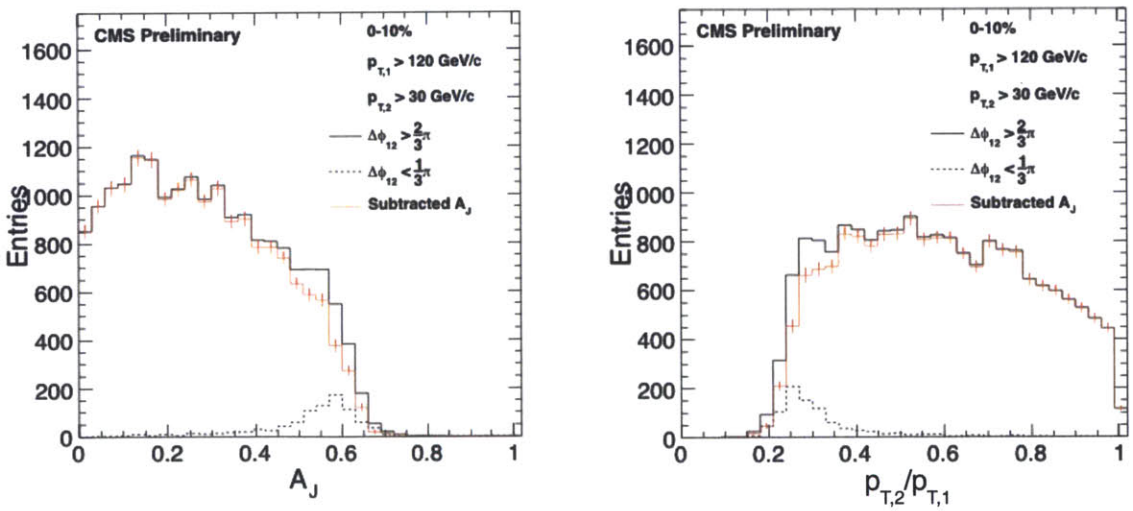

Figure 6-3: The background subtraction procedure for imbalance distributions.

6.2.5 Fraction of matched dijets and rate of background events

One of the early predictions for jet quenching involved a set of events where one jet disappears completely while another jet leaves the medium freely, when a dijet is produced in the surface of the medium [23]. Figure 6-4 shows the fraction of events where the leading jet has an accompanying jet above 30 GeV/c on the away side. It is interesting to note that at high enough $p_{\mathrm{T},1}$, the away-side jet is always found, meaning the medium is not sufficiently large to absorb the jet to below 30 GeV/c. The figure also shows the rate of background jet pairs, as defined in the previous subsection 6.2.4. Notice that the amount of such events vanished rapidly at low centralities and at high $p_{\mathrm{T},1}$.

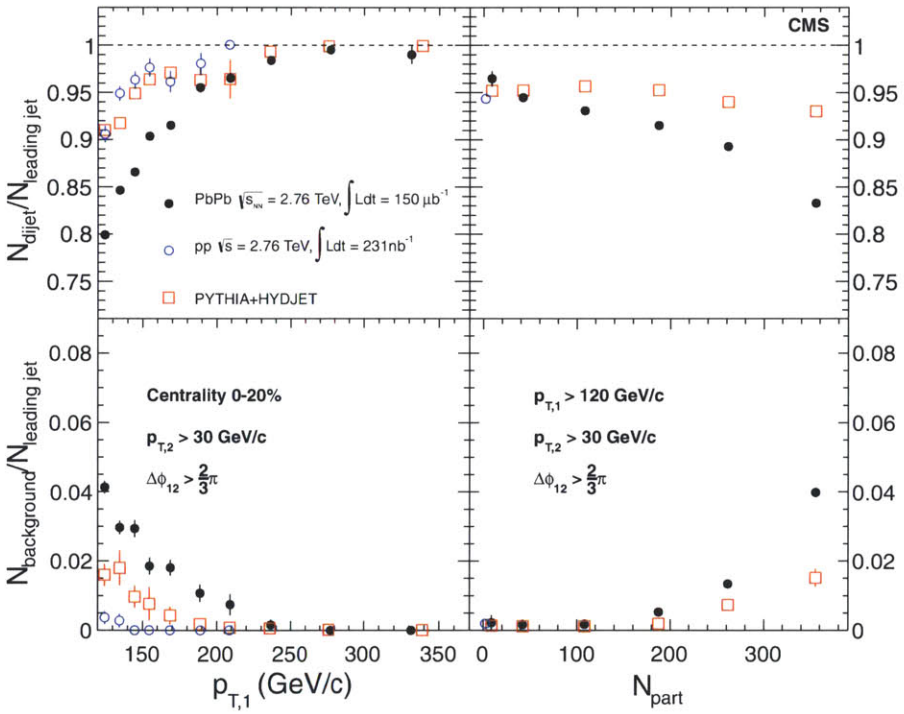

Figure 6-4: Fraction of events with a genuine subleading jet with $\Delta\phi > 2\pi/3$, as a function of leading jet $p_{\mathrm{T},1}$ (left) and $\mathrm{N_{part}}$ (right). The background due to underlying event fluctuations is estimated from $\Delta\phi < \pi/3$ events and subtracted from the number of dijets. The fraction of the estimated background is shown in the bottom panels. The error bars represent the statistical uncertainties. From [5].

6.2.6 Centrality dependence of imbalance

Figure 6-5 shows the distributions for the dijet asymmetry variable $A_J = \frac{p_{T,1}-p_{T,2}}{p_{T,1}+p_{T,2}}$, in bins of centrality, compared to the MC reference. One can observe that an enhanced imbalance effect, relative to the MC reference, appears when going towards more central events. The most peripheral bin, with the least observed imbalance, is also compared to the pp data, and the distributions are consistent within the statistical uncertainties. The MC reference roughly matches the pp distribution, however with slightly more balanced dijets. Nevertheless, the discrepancy between the MC reference and pp data is of a small magnitude, compared to the imbalance effect observed in the most central collisions. This enhancement in the imbalance can be attributed to the energy-loss mentioned in the earlier chapters.

With increasing collision centrality, the effect of background fluctuations increases. The background fluctuations appear in these distributions in two aspects:

First of all, the momentum resolution of the jets change as a function of the centrality, which smears the imbalance distributions accordingly. This smearing is small but visible in the distributions, and shifts the mean of the A_J spectrum by about 0.008 in both data and MC.

In addition to the resolution effect, in the cases where the true recoil jet is not found on the away side, a fake jet formed by a local background fluctuation may be selected as the subleading jet. This effect would also increase with the quenching of jets, absorbing the actual recoil jet completely or pushing its momentum below the analysis thresholds. Such mismatches are subtracted from the results by estimating from small $\Delta\phi$ events, as described in the earlier subsection 6.2.4. Therefore the final result does not exhibit a specific trend (such as the effects in analyses where this contamination is not subtracted [71]), however here it poses systematic uncertainties, which are evaluated from the estimated rate of such events.

At higher leading jet p_T selections, such background events disappear completely, and the resolution effect gets less significant. Next, we will examine what happens to the observed energy-loss when higher p_T selections are imposed, and try to quantify

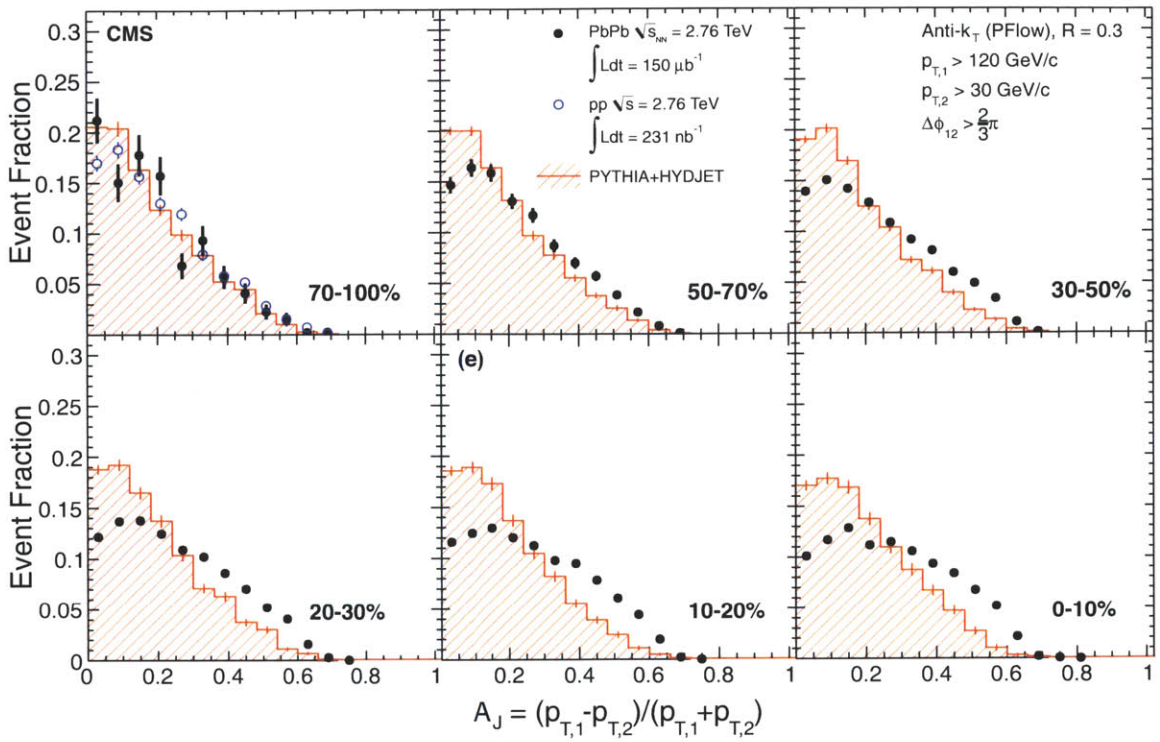

Figure 6-5: Dijet asymmetry ratio, A_J, for leading jets of $p_{T,1} > 120$ GeV/c and subleading jets of $p_{T,2} > 30$ GeV/c with a selection of $\Delta\phi > 2\pi/3$ between the two jets. Results are shown for six bins of collision centrality, corresponding to selections of 70–100% to 0–10% of the total inelastic cross section. Results from data are shown as points, while the histogram shows the results for PYTHIA dijets embedded into HYDJET PbPb simulated events. Data from pp collisions at 2.76 TeV are shown as open points in comparison to PbPb results of 70–100% centrality. The error bars represent the statistical uncertainties. From [5].

the momentum-dependence of the imbalance.

6.2.7 Momentum dependence of imbalance

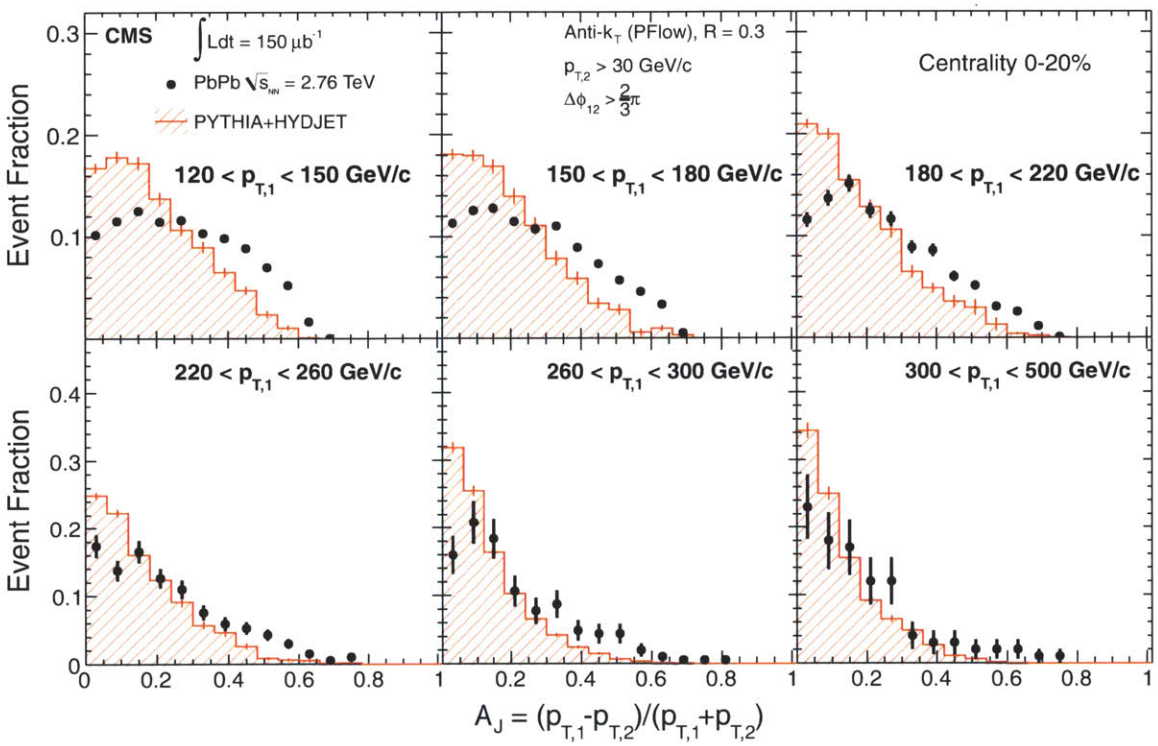

Figure 6-6: Dijet asymmetry ratio, A_J, in bins of leading jet transverse momentum from $120 < p_{\mathrm{T},1} < 150$ GeV/c to $p_{\mathrm{T},1} > 300$ GeV/c for subleading jets of $p_{\mathrm{T},2} > 30$ GeV/c and $\Delta\phi > 2\pi/3$ between leading and subleading jets. Results for 0–20% central PbPb events are shown as points, while the histogram shows the results for PYTHIA dijets embedded into HYDJET PbPb simulated events. The error bars represent the statistical uncertainties. From [5].

The first observation from the study of imbalance in different $p_{\mathrm{T},1}$ bins is that a certain amount of energy loss is happening in all these p_{T} values. Now it is interesting to observe any trends in the different imbalance distributions when varying in $p_{\mathrm{T},1}$. To first order, the distributions can be characterized by their mean value, which is plotted against $p_{\mathrm{T},1}$ in figure 6-8. This figure has various features, which deserve some discussion. The MC reference distributions all have an increasing trend. This trend shifts (downward) little as centrality is varied, due to background fluctuations causing slightly more imbalance. Remember, however, that the background fluctuations are only a fraction among the factors affecting the jet resolution.

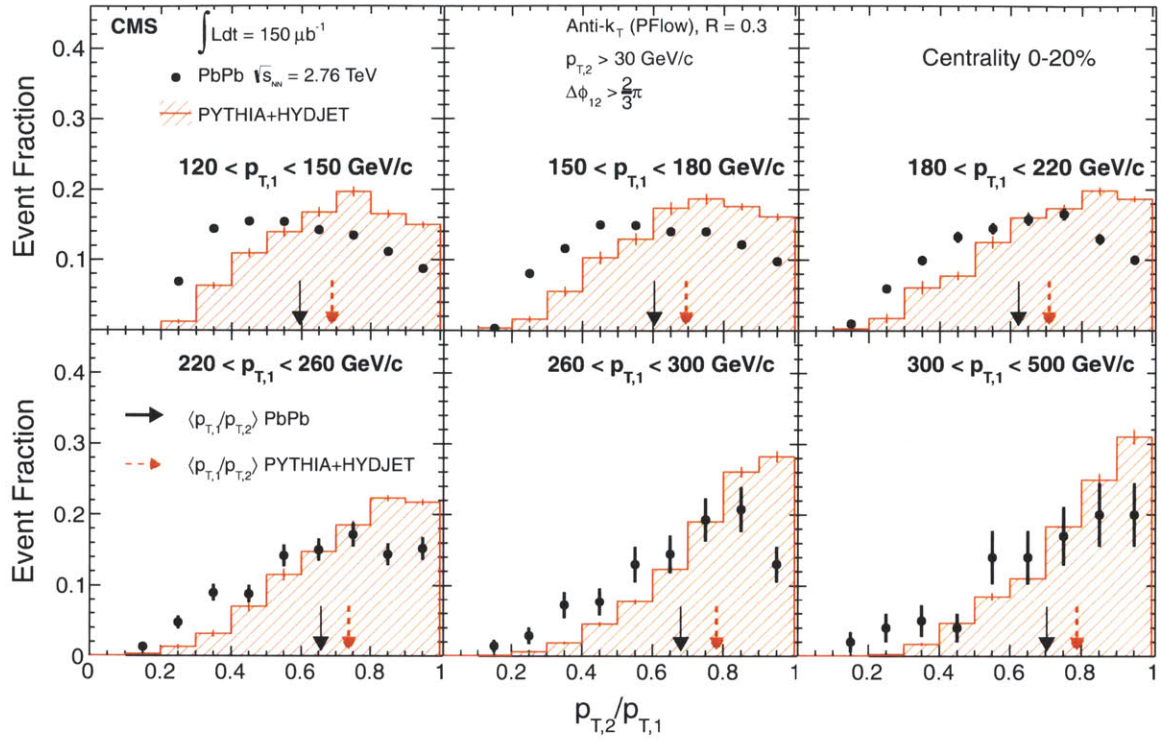

Figure 6-7: Subleading jet transverse momentum fraction ($p_{\mathrm{T},2}/p_{\mathrm{T},1}$), in bins of leading jet transverse momentum from $120 < p_{\mathrm{T},1} < 150$ GeV/c to $p_{\mathrm{T},1} > 300$ GeV/c for subleading jets of $p_{\mathrm{T},2} > 30$ GeV/c and $\Delta\phi > 2\pi/3$ between leading and subleading jets. Results for 0–20% central PbPb events are shown as points, while the histogram shows the results for PYTHIA dijets embedded into HYDJET PbPb simulated events. The arrows show the mean values of the distributions and the error bars represent the statistical uncertainties. From [5].

6.2.8 Energy resolution effects on the observed imbalance

The results shown in the previous subsections have been in "reconstructed" level. Which means, we are looking at the convolution of multiple effects, which allows us to only make very rough qualitative statements on the observed energy loss. Figure 6-9 shows how different the imbalance result is, in the absence of resolution effects. In the same figure it is also shown that the resolution effects can be emulated by a random smearing of generator-level MC events. This procedure for model comparisons will be discussed later in section 7.0.3.

Without the resolution effects (or smearing), figure 6-9 shows that the imbalance in Pythia already has an increasing trend for this observable. This is because the ra-

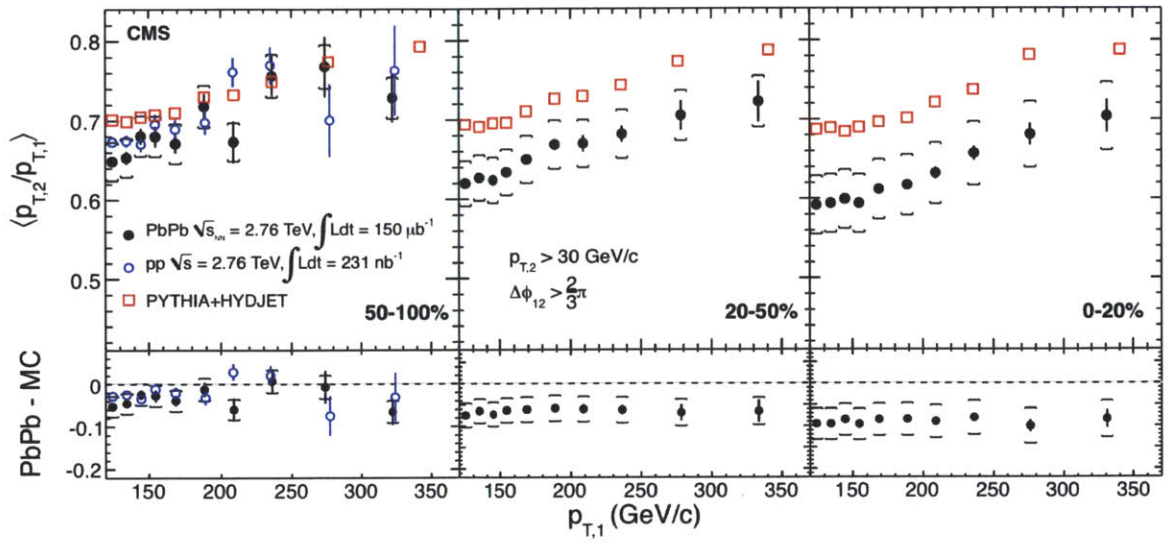

Figure 6-8: Average dijet momentum ratio $p_{T,2}/p_{T,1}$ as a function of leading jet $p_T$for three bins of collision centrality, from peripheral to central collisions, corresponding to selections of 50–100%, 30–50% and 0–20% of the total inelastic cross section. Results for PbPb data are shown as points with vertical bars and brackets indicating the statistical and systematic uncertainties, respectively. Results for PYTHIA+HYDJET are shown as squares. In the 50–100% centrality bin, results are also compared with pp data, which is shown as the open circles. The difference between the PbPb measurement and the PYTHIA+HYDJET expectations is shown in the bottom panels. From [5].

diation dynamics in vacuum may change with the changing p_T selection. In addition, energy resolution shifts this result by a p_T-dependent amount. From the discussion in section 4.1, we have already seen that the jet resolution is a function of the jet p_T, and this is directly reflected in the imbalance results.

The value of the $p_{T,2}/p_{T,1}$ is therefore difficult to translate analytically into the fraction of lost energy. In chapter 7, we will attempt to quantify the conclusions with a more detailed look at these multiple effects.

6.2.9 Systematic uncertainties

The dominant sources of uncertainty are those from the resolution of jets (and accuracy of background model), which was mentioned in section 4.2.1, and the jet energy scale, which was discussed in section 4.2.1.

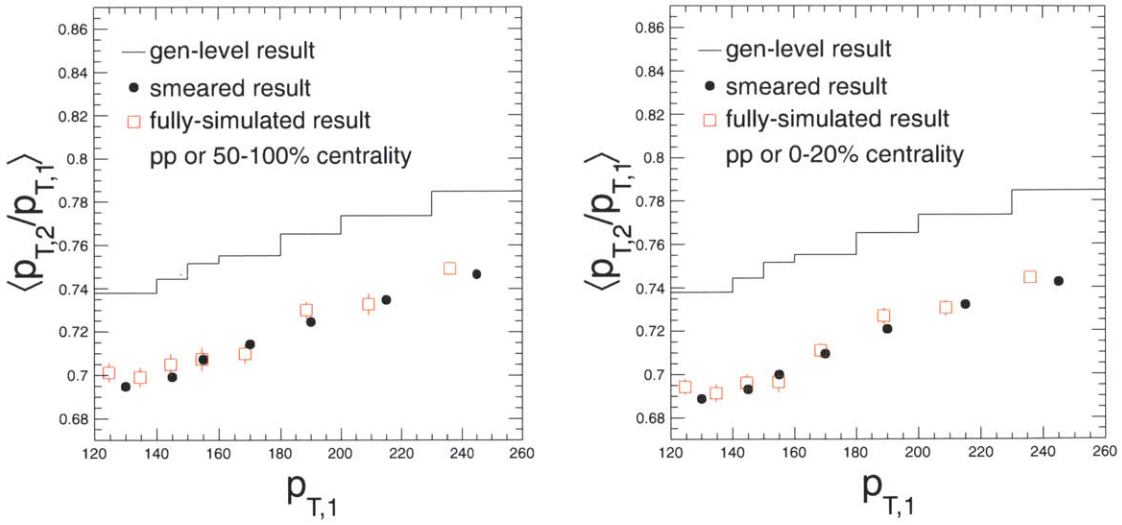

Figure 6-9: Comparison of imbalance result from smeared jets to fully simulated Pythia sample.

First of all, a priori to all measurements, the fragmentation of the jets observed in PbPb may be different than in pp. Since the jet energy corrections are based on pp fragmentation, and the resolution is estimated in the same assumption, the uncertainty of the fragmentation effects directly influence the uncertainty of the jet energy scale and resolution simultaneously. The effects are studied by variation of jet corrections by the amount of uncertainty. This variation is applied to high and low p_{T} ranges with maximum difference. The envelope that contains the amount of variation to be applied to the jet energy scale is determined from the discussion in section 4.2.1.

The presence of a large underlying event activity certainly affects the resolution. The resolution is important to estimate correctly since it has a role in MC to data comparison, as will be discussed in chapter 7. The uncertainty due to background fluctuations is estimated from comparison of embedded events to non-embedded events, and also to events embedded into different background generator tune 4.2.1.

The summary of systematic uncertainties on the dijet imbalance results [5] is displayed on table 6.3.

Table 6.3: Summary of the $\langle p_{T,2}/p_{T,1} \rangle$ systematic uncertainties. The percentages represent the ratio of absolute uncertainty to the actual value of the variable, which ranges from 0.6 to 0.8.

	20–30%		0–10%	
Source	$p_{T,1} < 140$	$p_{T,1} > 300$	$p_{T,1} < 140$	$p_{T,1} > 300$
Underlying Event	3%	3%	5%	5%
Jet Energy Scale	3%	3%	3%	3%
Jet Efficiency	1%	$< 0.1\%$	1%	$< 0.1\%$
Jet Fake Rate	$< 0.1\%$	$< 0.1\%$	1%	$< 0.1\%$
Calorimeter Noise	$< 0.1\%$	$< 0.1\%$	$< 0.1\%$	$< 0.1\%$
Jet ID	$< 0.1\%$	$< 0.1\%$	$< 0.1\%$	$< 0.1\%$
Total	4.5%	4.5%	6%	6%

6.3 Other observations

6.3.1 Jet fragmentation pattern

The fragmentation pattern of the jets can also be a probe of the medium effects. With the measurements of the fragmentation, one can observe possible modifications in the profile of the parton shower, and get ideas on the radiation and scattering pattern of the partons traversing the medium. It is also of importance for the jet reconstruction performance studies. The effects on the fragmentation can influence the jet p_{T} determination due to the non-linearities introduced by calorimeter response and tracking efficiency. The fragmentation patterns of leading jets and subleading jets are studied separately [6]. The fragmentation is quantified by the distributions in the ξ variable.

$$\xi = \ln \frac{1}{z} \quad ; \quad z = \frac{p_{\parallel}^{\mathrm{track}}}{p^{\mathrm{jet}}}, \tag{6.1}$$

where $p_{\parallel}^{\mathrm{track}}$ is the projection of the track momentum onto the jet axis, in the frame of the dijet, defined as $\eta_{\mathrm{dijet}} = (\eta_1 + \eta_2)/2$, as illustrated in figure 6-10.

Remember from section 3.1.7 that the tracking algorithm, including the geometrical acceptance, is not 100% efficient in capturing all charged hadrons that are produced in the event. In order to correct for this effect, the tracks that are counted in fragmentation function are weighted by a factor of inverse efficiency, so that the lost tracks are accounted for. The efficiency is only defined as an average quantity for various types of fragmentation possible for a jet to undergo, therefore such a track-by-track application of weights is a source of uncertainty in the analysis. This uncertainty is estimated from difference of results with and without track weights, and also from non-closure in MC for a given sub-set of events with a specific fragmentation. This is the dominant uncertainty in the analysis and has an effect of 10% in ξ distributions.

In the fragmentation function study, it is both convenient and required to use the pp data sample as reference, rather than MC. The different amounts of jet p_{T}

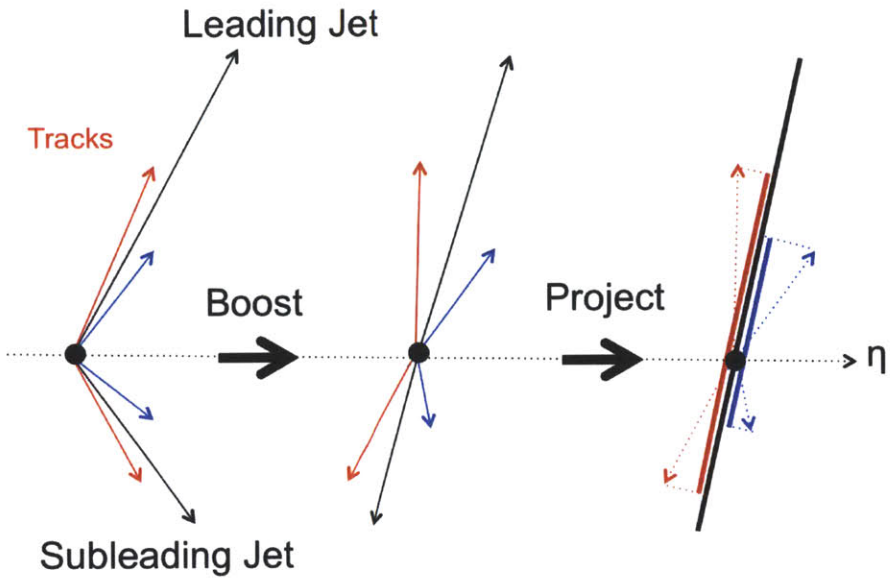

Figure 6-10: Definition of the fragmentation variable z [6]. The track momentum is projected on the jet axis, in the frame of the dijet which is approximated by $\eta_{\text{dijet}} = (\eta_1 + \eta_2)/2$. The black arrows represent the momenta of the reconstructed leading and subleading jets, where it is important to note that this definition for jet momenta is **not** expected to represent the momentum of the parton in the hard scattering, but rather the final state of the shower that forms while and after traversing the medium.

resolution in PbPb and pp may cause a difference in the observed ξ distributions. The comparison is performed in the reconstructed-jet level, therefore in order to have a consistent resolution, the p_{T} values of the jets in the pp sample are artificially smeared by the quadratic difference of estimated resolutions in PbPb and pp, resulting in the same effective resolution. The fragmentation function obtained this way is compared to the PbPb data.

The dijet sample is analyzed in bins of A_J. The corresponding pp reference is not produced by the same A_J cut, but rather by reweighting the events in jet p_{T} so that the p_{T} distributions are the same as in PbPb. In this way, the effects that are solely due to the momentum difference are eliminated to a good extent, with uncertainties due to the unknown parton composition.

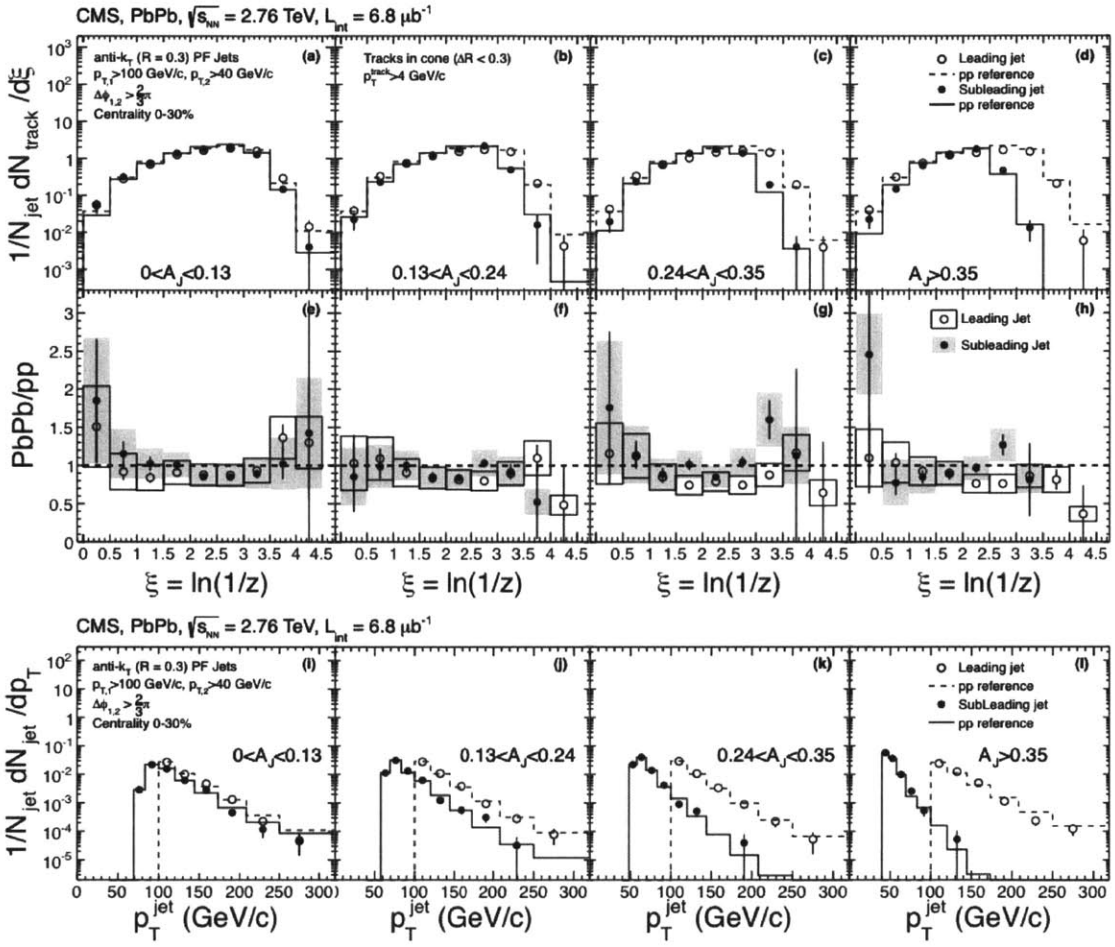

Figure 6-11: (a–d) Fragmentation functions for the leading (open circles) and subleading (solid points) jets in four regions of A_J in central PbPb collisions compared to the pp reference. (e–h) Ratio of each fragmentation function to its pp-based reference. Error bars shown are statistical. The systematic uncertainty is represented by hollow boxes (leading jet) or gray boxes (subleading jet). Only statistical uncertainties are shown. From [6].

6.3.2 Jet cross-sections and nuclear modification factor

As mentioned earlier, the enhanced momentum imbalance in the dijet events does not directly reveal the average amount of energy loss per parton, mostly because the leading jet is also subject to quenching. The analysis of inclusive jet cross-sections in PbPb and pp, as a function of jet p_{T},however, can give the exact complementary information on the quenching that we need.

In the introduction, we had defined the factorization theorem based on the distinction between the long-time and short-time physics. Assuming the short-time physics is same for parton interactions that occur in PbPb and pp collisions, one can expect the production rate for a *parton* with a given p_{T} to be the same in both systems. What is different however, is the evolution of the parton into jets, and since the jet p_{T} is a falling spectrum, the cross-section for jets in a given p_{T} in PbPb will appear to be shifted to lower values than the expected production.

In order to compare PbPb and pp, it is important to estimate the amount of underlying nucleon collisions, $\mathrm{N_{coll}}$, and scale the PbPb result accordingly. The details of centrality determination are discussed in appendix 5. The *nuclear modification factor*, R_{AA}, is defined as :

$$R_{AA} = \frac{dN^{AA}_{jets}/dp_{\mathrm{T}}}{< \mathrm{N_{coll}} > dN^{pp}_{jets}/dp_{\mathrm{T}}} \tag{6.2}$$

This is measured by CMS with the data from PbPb and pp collisions at 2.76 TeV [7]. The jet p_{T} spectra are obtained by Bayesian-unfolding the observed reconstructed-jet p_{T} spectra for the resolution effects. The response matrix of jet p_{T} are obtained from full Pythia simulations, without fitting. The results as a function of jet p_{T} are in figure 6-12.

Since the pp result is the common denominator of all R_{AA} results, the statistical fluctuations in the pp data are reflected in R_{AA} of all centralities. Aside from that, one can see that the p_{T} dependence of the R_{AA} is very little, the ratio is very close to flat distribution in a given centrality bin. On the other hand, there is a very strong

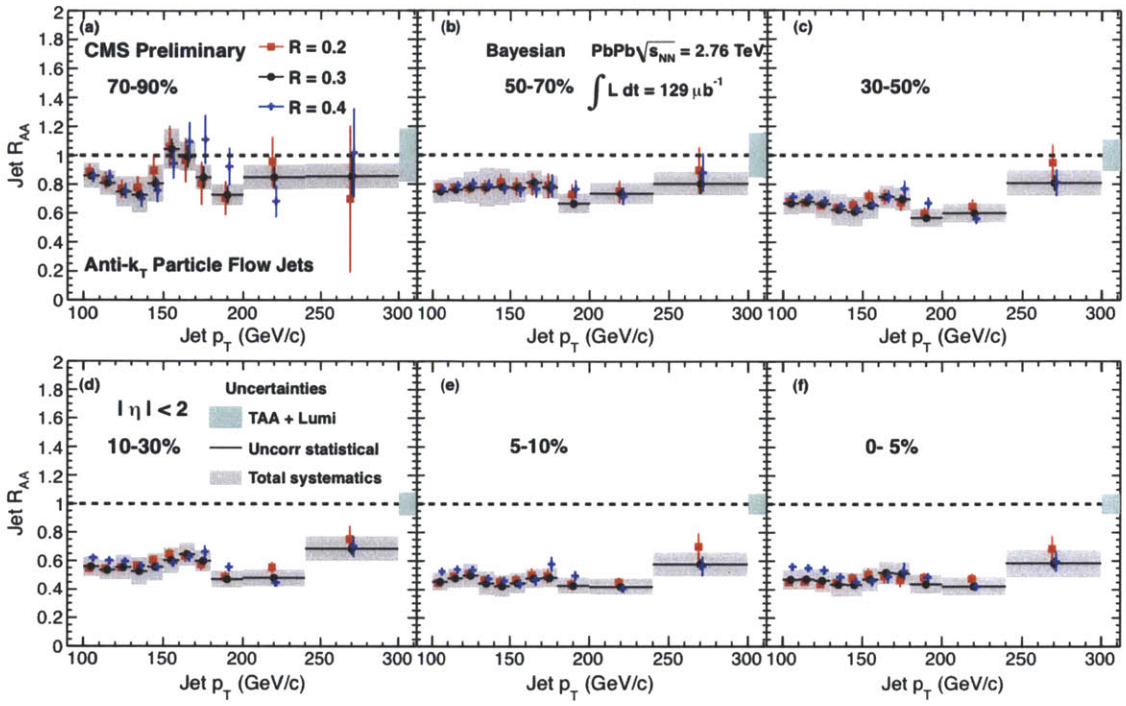

Figure 6-12: Results for the nuclear modification factor, R_{AA}, for inclusive jet p_{T} spectra in various centrality bins. Results with different R parameters in jet definition (with anti$-k_{\mathrm{T}}$, see section 3.4), exhibit similar results. Notice that the statistical fluctuations of the reference (pp) spectrum is reflected in results at all centralities. From [7].

correlation to the collision centrality. Figure 7-2 shows the centrality dependence of the jet suppression, by presenting R_{AA} as a function of $\mathrm{N_{part}}$.

The results from the jet R_{AA} measurement will be combined with momentum imbalance results in order to achieve true distinction between models that are explored in section 7.

One should remark that charged hadron R_{AA} measurement provides equivalent information, given the jet fragmentation not modified strongly. The jet fragmentation will be discussed in the next subsection.

Chapter 7

Results and discussion

The analyses discussed have taught us important lessons about the jet-quenching phenomenon. Although the jets behave in a similar manner to pp in peripheral PbPb collisions, the central collisions, in which a greater amount of material is involved, exhibit interesting effects that imply the loss of energy in the formation of the jets. The results showing these modification to the jets in the most central collisions are summarized in figure 7-1.

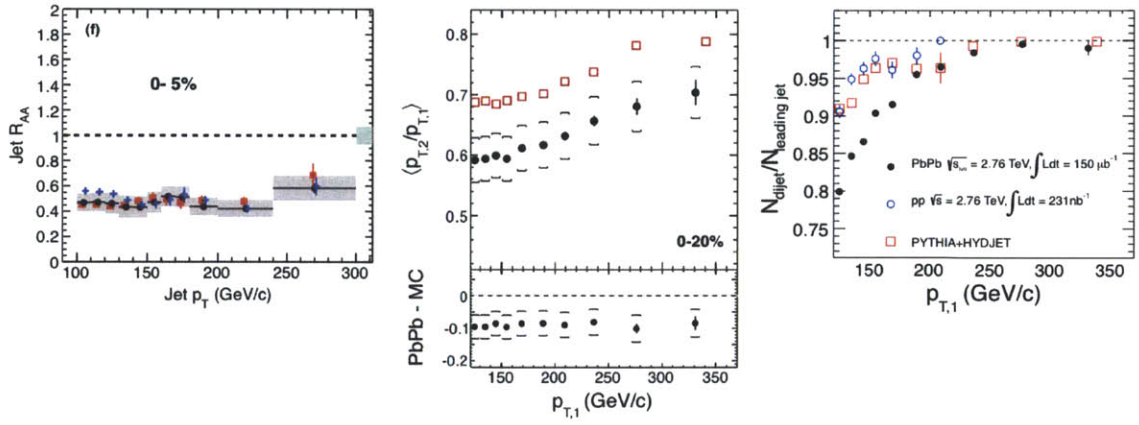

Figure 7-1: The summary of the quenching results that construct the primary input to the discussion of the magnitude of energy-loss, with results from [7] and [5].

Although the measurement of leading jet momentum dependence of imbalance is a simple one, it is not very straightforward to extract the physics of the observed

behavior. When trying to interpret the middle figure 7-1, one has to avoid the wrong conclusions by keeping in mind the following:

- The rise of the mean p_{T}-ratio is **not due to** any weakening of energy-loss : Although the mean p_{T}-ratio in PbPb data approaches 1, so does the imbalance in pp, because of vacuum QCD and resolution effects. Only the contrasts between the two results is relevant, whose comparison may be complicated. Although it is difficult to conclude about the exact p_{T}-dependence of the effect, the energy loss effect does exist by a significant amount in even the highest-p_{T} selection.

- A constant difference of mean p_{T}-ratio in PbPb and pp **does not mean** jets lose a **constant fraction** of their energy, neither it excludes the scenario. The x-axis represents the leading jet after energy loss, and it is significantly affected by quenching as well.

A short time after the p_{T}-dependent imbalance results were published, the inclusive jet suppression results were also presented by CMS and Atlas experiments, as discussed in 6.3.2. These results confirm the existence of quenching up to highest jet p_{T} ranges observed, and provide an additional constraint on the energy loss mechanism. The discussion here tries to combine these observations to clarify the physics message of the dijet imbalance.

Since the dijet imbalance study had focused on the centrality bin of 0-20%, in the discussion of results in the next chapter, we will constrain the quenching model parameters by the R_{AA} data, and for 0-20%, we will use the region shown in figure 7-2 to define whether the model is compatible with the data for this centrality selection.

7.0.3 Modeling of results

As emphasized earlier, the message of the dijet imbalance results have to be treated very carefully. For any model that attempts to describe the quenching effect, one should compare exactly the same variables as the data is presented in. This involves applying the proposed effect on realistic vacuum-QCD MC events, and plotting results

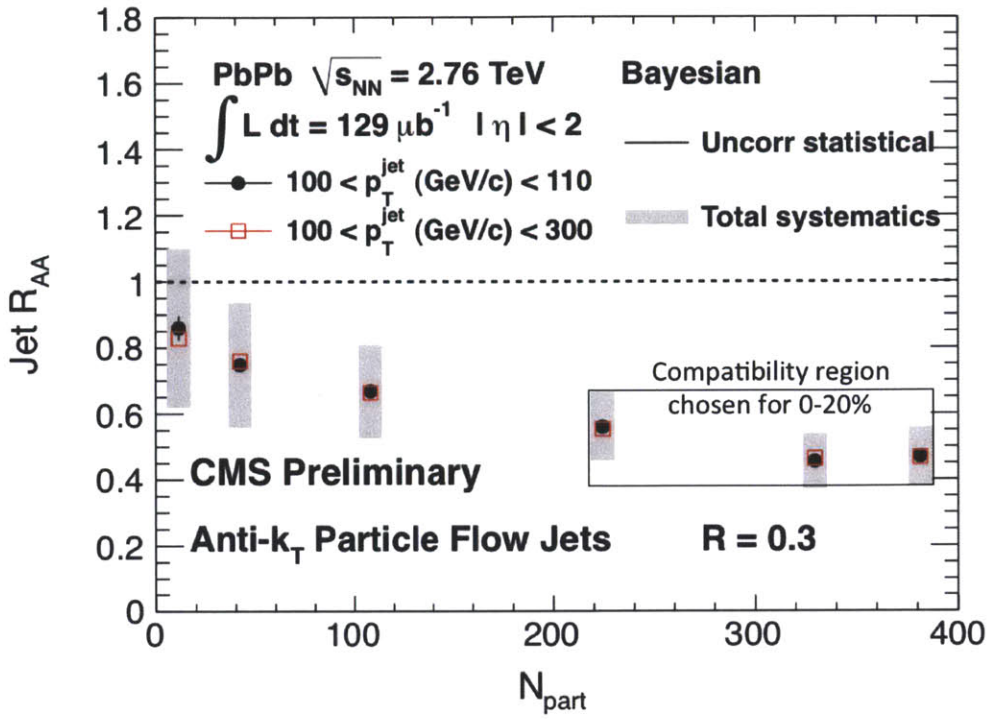

Figure 7-2: Centrality dependence of the inclusive jet R_{AA}. One may observe that the turn-on of the quenching effect appears very sharp at the peripheral events. A band containing, with systematic uncertainties, the most central bins is chosen to represent the result for 0-20% central collisions, to be used in constraining the models discussed later in the chapter. The data points are from the analysis in [7], however the interpolation to 0-20% and region for testing model compatibility is chosen by the author.

in the reconstructed level. The detector simulation and reconstruction software may not be available for any theorist trying to test a hypothesis. However, the experiment claims the ability to represent the detector effects by simple toy MC, in which a gaussian smearing is applied in order to account for the jet energy resolution. The discussion below illustrates the approach, and presents examples of compatibility tests for very simple quenching scenarios.

Folding the resolution effects

As discussed earlier in 6.2, the momentum dependence of the imbalance of reconstructed jets displays the cumulative effect of various factors involved. One approach

Table 7.1: Parameters of the functional form for the jet energy resolution $\sigma\left(p_{\mathrm{T}}^{\mathrm{Reco}}/p_{\mathrm{T}}^{\mathrm{Gen}}\right)$ given in Eq. 4.1, obtained from GEANT4 simulation of PYTHIA pp jets and from PYTHIA jets embedded in HYDJET events for various PbPb centralities (indicated by the % ranges in parentheses). The units of S are $\sqrt{\mathrm{GeV}/c}$ and the units of N are GeV/c.

Source	C	S	N (pp)	N (0–20%)
Published	0.0246	1.213	0.001	5.23
Rounded	0.025	1.2	0	5

in deducing the amount of actual energy loss can be by assuming a certain model, and test its consistency with data by applying the resolution effects to obtain the same observable. We can do this for many models, however, the most important is to test the accuracy of this approach by first doing it for the reference distribution, which is Pythia in this case. The most realistic application of the resolution effects can be achieved by fully simulating the detector response and the underlying events, as in section 4.2.1. However, this is not feasible for an extended study of all models, since not all theorists can afford such computation, neither can access the detailed CMS detector description and software. We need to therefore be able to emulate the same effects on a probabilistic basis with simple smearing methods.

One should notice the fact that the resolution effect applied this way is not a simple smearing of the imbalance variable by the combined two jet resolution. Instead, each jet in the event is smeared by the resolution, and the leading and subleading jets are determined only after this smearing procedure. This means, the leading jet before smearing can become the subleading jet after smearing, and the third jet can become the subleading jet after smearing. Such different scenarios are displayed on Figure 7-3.

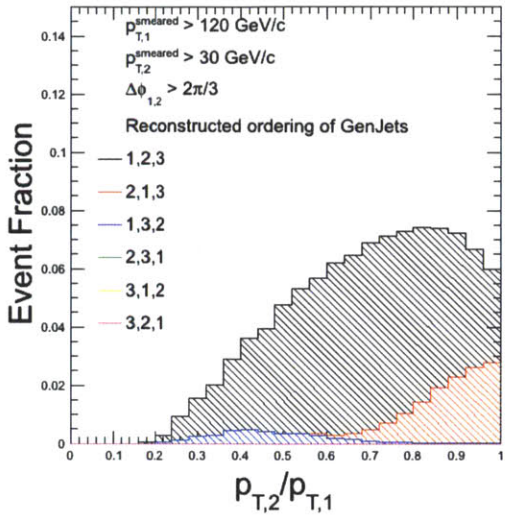

Figure 7-3: The colors represent the different permutations of the reconstructed jets. As an example, (2,3,1) refers to the events in which the leading GenJet has become the third highest p_{T} RecoJet and the subleading GenJet has become the leading RecoJet. The first two type of permutations are those in which the third jet or a background fluctuation has not affected the analysis. The dominant contribution among the rest is the case in which the third jet (or background fluctuation) supersedes the true subleading jet, colored in red.

7.0.4 Simple energy loss scenarios

It would be interesting to visualize how a certain amount of energy loss affects the reconstructed result with a certain resolution, and parametrized by the leading jet. We can apply simple energy loss distributions on the jets in generator level pythia events. With following assumptions:

- that the energy loss acts on scales at which the full pythia shower down to a radius of 0.3,
- that the GenJet represents the collinear portion of the shower

we can subtract the energy from GenJets, and apply the resolution effects. With this assumption of the GenJets representing the parton passing through the medium, we will use the term "parton" when referring to the object in the following discussion. The observations of the jet fragmentation patterns, which were discussed in section 6.3.1 support the idea of well resolved partons which fragment after reaching the vacuum, and we are interpreting the observed jet to be well representing this parton.

A jet of a given p_{T} does not always lose a fixed amount of its energy, but rather can suffer different amount of energy loss at different times due to the fact that:

- The material that is present in the trajectory of the parton is different in every collision.
- The energy loss happens through processes of quantum mechanical nature.

This means that the energy loss will appear as a distribution from zero up to the total energy of the parton. We can add a further assumption that this distribution peaks at zero.

Since the available measurement focuses on the average effect for a given p_{T} and centrality selection. The probability distribution for energy-loss can be described with a single width parameter, and the results are not very sensitive to the shape of the

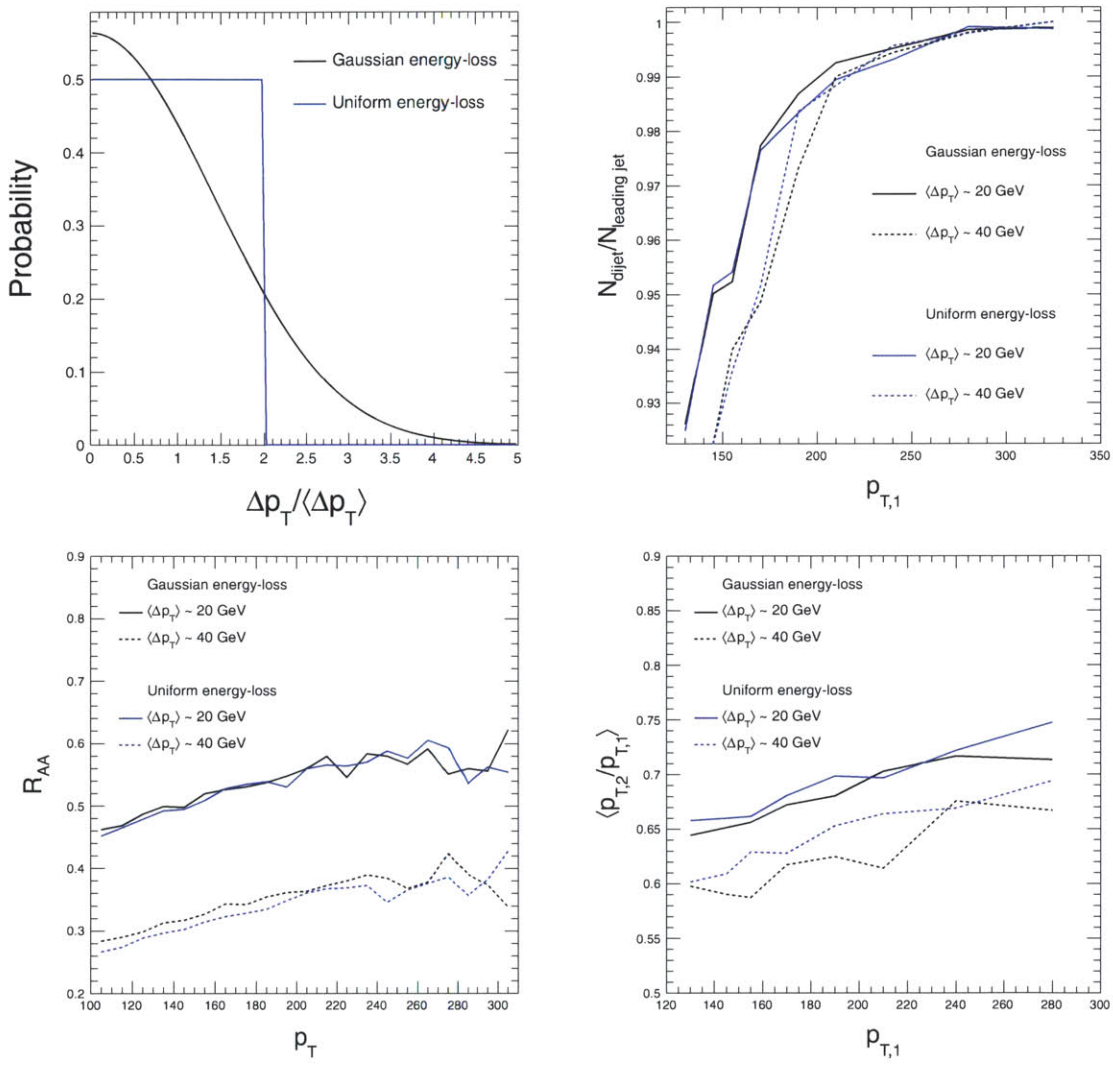

Figure 7-4: Test of sensitivity of results to the underlying probability distribution for energy-loss. Flat and Gaussian energy-loss distributions, with the same average value, return similar results for the observables of interest, while the amount of average energy-loss visibly effects the results.

distribution. This is illustrated in figure 7-4, where gaussian and uniform probability distributions for energy-loss are compared.

Multiple scenarios are implemented, with different assumptions on the correlation of the different jets' energy loss. At each scenario, the p_{T} dependence is separately applied with two options: constant energy loss and constant fractional energy loss.

Independent energy loss for the jets

In the simplest scenario, we assume all jets among the chosen events to be subject to the same amount of medium, and let quantum fluctuations introduce a variety of energy values to be dissipated, assumed to be gaussian. This approach neglects the fact that the amount of material traversed highly depends on where in the medium the dijets were produced, in addition to the motion of the medium itself. A number of calculations available in literature follow this approach for simplicity, referring to the assumption as a "brick of QGP", with a nice comparison of different formalisms in [72].

In each one the amount of energy loss is determined randomly from a positive gaussian function with a width of $\sigma_{\Delta p_T}(p_T^i) = \sqrt{2}E$, where p_T^i is the GenJet p_{T} before artificial energy loss and E is the input energy loss parameter, either being $E = constant$, or $E = constant \times ln(p_T^i)$ or $E = constant \times p_T^i$, where i stands for the index of the jet among the N jets available in the event. The energy-loss probability distribution is shown i figuren 7-5. Later when comparing to path-length related modulation of energy-loss, we will see that the gaussian parametrization of the probability is a reasonable approximation. However, here the quenching of the jets is treated independently, which will be the main contrast to the next calculations where a geometry model is used.

After the application of energy-loss, the jets undergo the resolution smearing procedure described in section 7.0.3. This way, supposedly "reconstructed jets" are obtained. The leading and subleading jets are determined among the collection of the N jets in the acceptance ($|\eta| < 2$) based on the "reconstructed" energy. This way, the model calculates the exact quantity that the data represent.

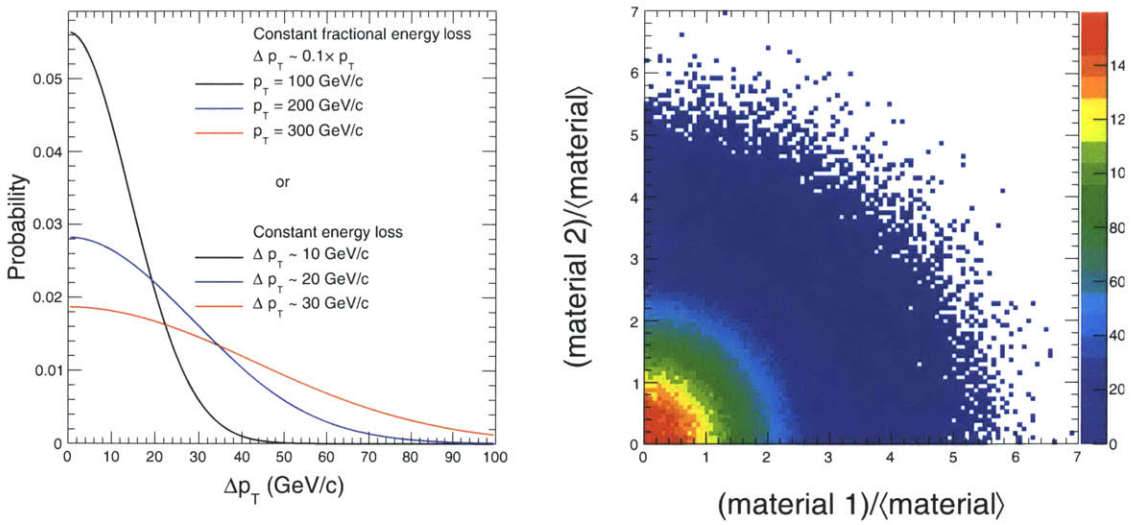

Figure 7-5: Probability distribution of energy-loss for a given parton. The distributions are characterized by their average value, which is constructed to have a specific p_{T} dependence. On the right, the distribution of the energy-loss (with an arbitrary scale) for the two back-to-back partons.

Figure 7-6 shows the comparison of model results to data. The top row shows the R_{AA} results, which intends to calibrate the average amount of energy loss. The second rows shows the momentum imbalance results, which is somehow smeared as a result of the energy loss. It can be observed that, for a given amount of energy loss, it is difficult to cause an imbalance of dijets to the extent in data when the energy loss of the two jets is completely independent.

In the third row of 7-6, as well as later figures, shows the matched dijet fraction, which is of complementary nature to the momentum imbalance, which is restricted to completely found dijets, with cut-offs. The dijet fraction represents the below-threshold extrapolation of the imbalance distributions. If the underlying distribution is too wide (towards low values), then this is reflected by a large amount of missing subleading jets. Interestingly, this test challenges the p_{T}-dependence of the energy loss with better success than others, limiting the possibilities a lot more in a p_{T}-linear energy loss. This challenge is also observed in later figures where a different underlying mechanism, based on collision geometry, is implemented.

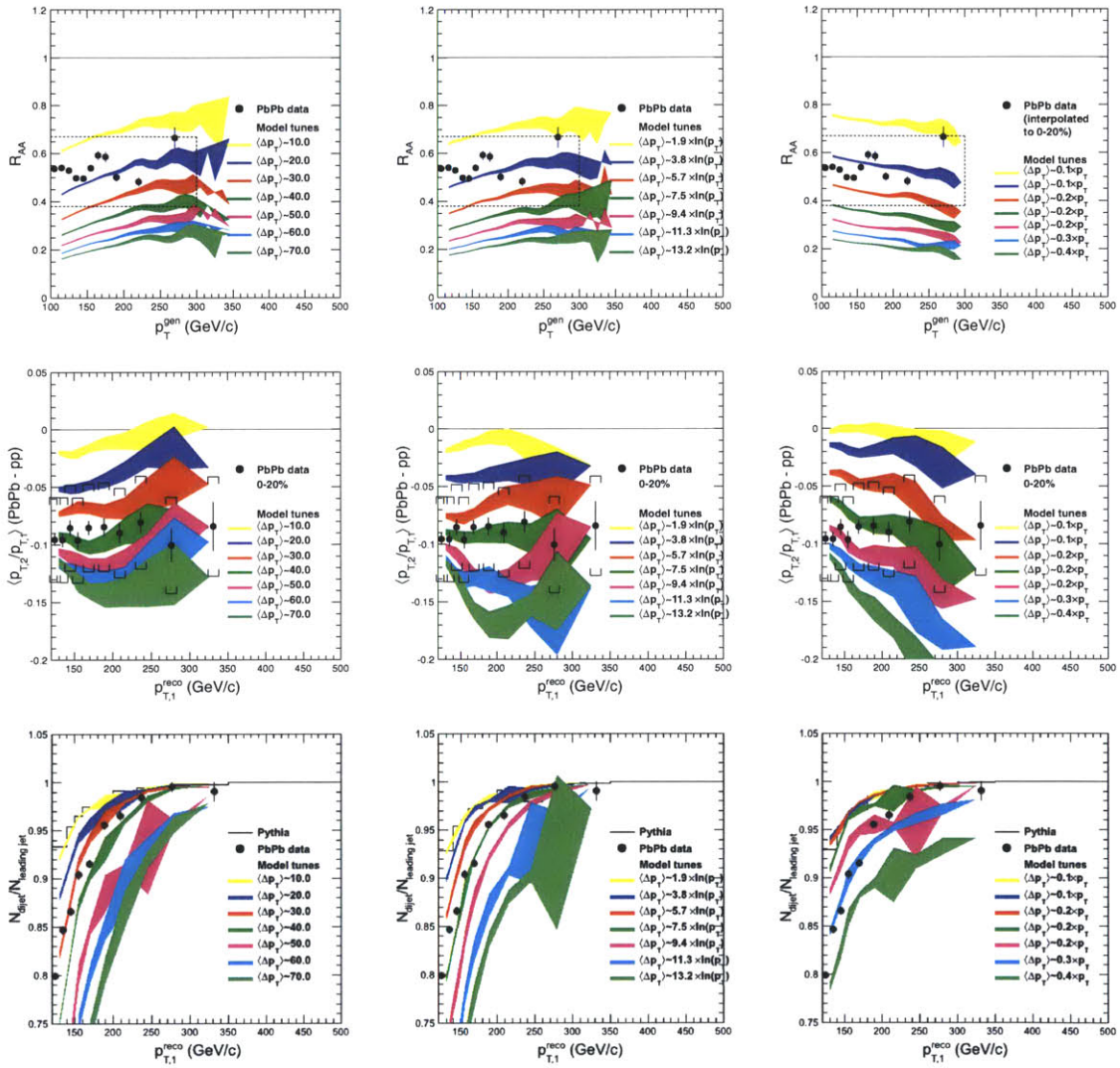

Figure 7-6: Comparison of results from simple independent energy-loss model with data. In order to introduce a large imbalance between the two jets, the average energy loss has to be very high, which is not compatible with the R_{AA} results (e.g. the green curves). The R_{AA} result for PbPb data is interpolated to 0-20% as described in figure 7-2.

Energy loss based on collision geometry

Studies of harmonic flow [46] have taught us of how fluctuations in the geometry of the nuclei in a collision are important in determining the properties of the matter produced. They also show that the so-called Glauber calculations are very effective in emulating the general features of the geometry fluctuations for central nuclear collisions. This observation naturally implies that the medium effects on jets also depend on these fluctuations, and on the orientation of the jets inside the medium. The correlation of the energy loss between the to jets may be emulated by a simple model where the amount of matter that a parton traverses is approximated by the amount of participating nucleons along the line of motion. Using the PHOBOS Glauber MC [67], we have calculated the material event-by-event [73] , and applied the energy loss on the jets with the earlier prescription. An example dijet event is shown in figure 7-7, where all nucleons along the path of the jets are highlighted. Such calculation naturally introduces the geometry bias of figure 1-12 in the observable, since the selection is based on the leading jet p_{T}.

Before moving onto dijets, we can observe the material distribution for inclusive jets. In figure 7-8, the result is compared to the AuAu calculation in [4].

Figure 7-9 shows the material distributions for the first and second jet. The correspondence of these to the leading and subleading jet is unknown at this point, the assignment of first vs second jet is completely arbitrary since the distribution is symmetric. The energy-loss is correlated to geometry using three different quantities. The first is the number of participant nucleons encountered by a parton along the path of motion. Since the parton-medium interaction scales may be of comparable magnitude to the length scales of the medium, the coherence of the states may have significant impact on the energy loss, which may introduce dependencies on the medium size. With this in mind, length-related terms are also used in the calculation, and the second material variable is the sum of the $L = |\vec{r}_{nucleon} - \vec{r}_{vertex}|$ for the nucleons along the path, and the third variable is the sum of L^2. Each of these material-related quantities are used to represent the amount of energy loss in different models.

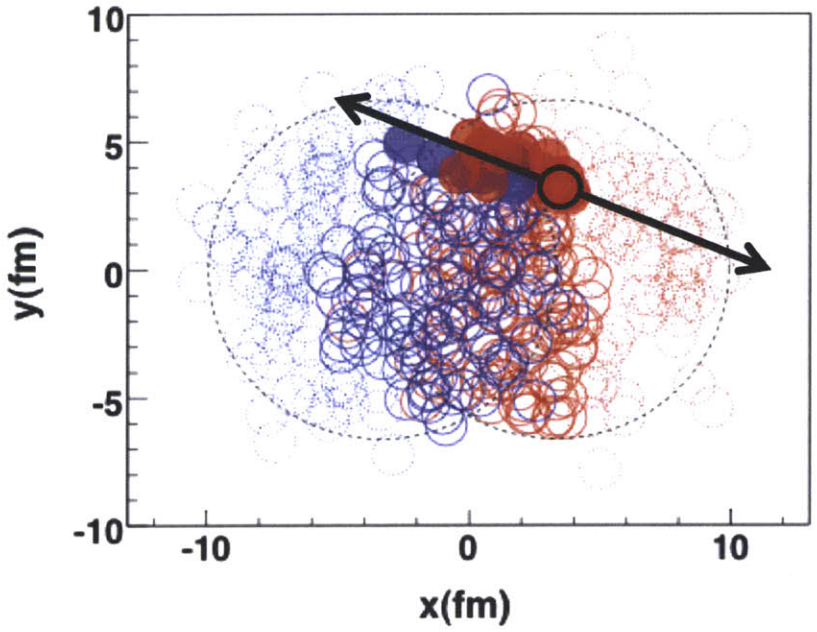

Figure 7-7: An example event, generated by modified PHOBOS Glauber MC. The blue and red correspond to nucleons belonging to different nuclei before the collision, however treated equally once the collision happens. The faint circles are spectator nucleons which have not participated in the collision, and the dark open circles are participating (wounded) nucleons. Among these, the solid circles represent the nucleons that fall in the path of the two back-to-back jets.

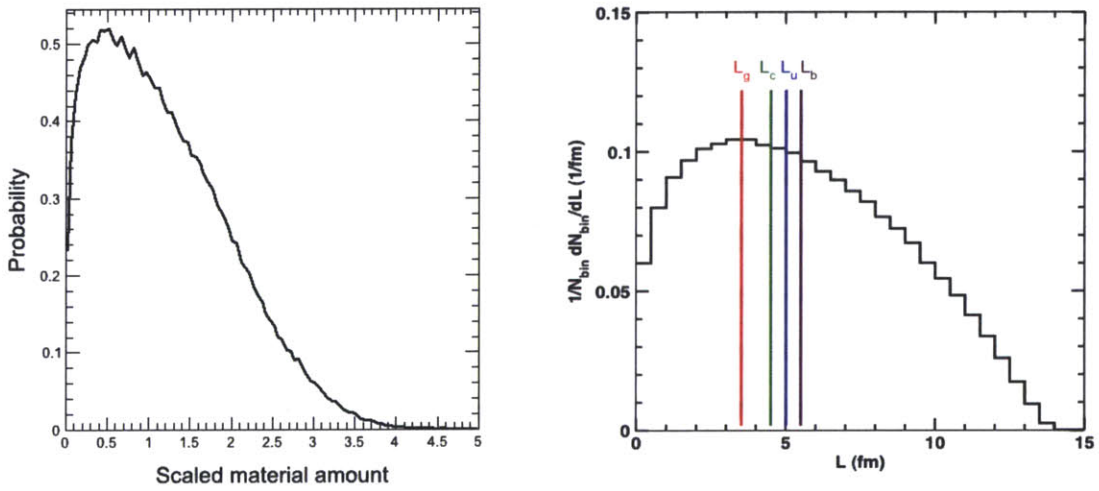

Figure 7-8: Left : The distribution of the scaled amount of material (to give average = 1), to be later multiplied with the energy-loss parametrization in jet p_{T}. Right : The density-weighted path-length calculation in AuAu from [4].

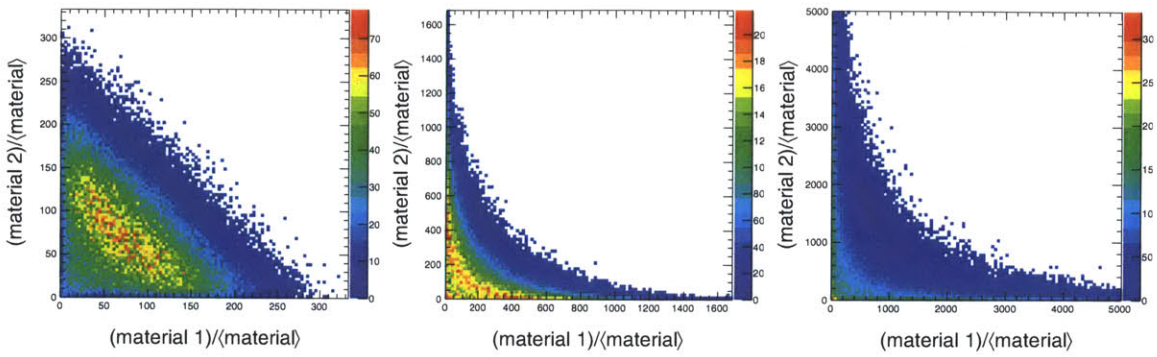

Figure 7-9: Material distributions for the two back-to-back parton trajectories.

Figure 7-10 shows the projection of the material distributions for a single jet. The first column is similar to the calculation in [4]. The distribution is scaled horizontally to have an average of 1, so that the amount of energy-loss is purely set by the momentum-dependent term used in the earlier parts. This is a reason why it is quantitatively different in scale from figure 1-11.

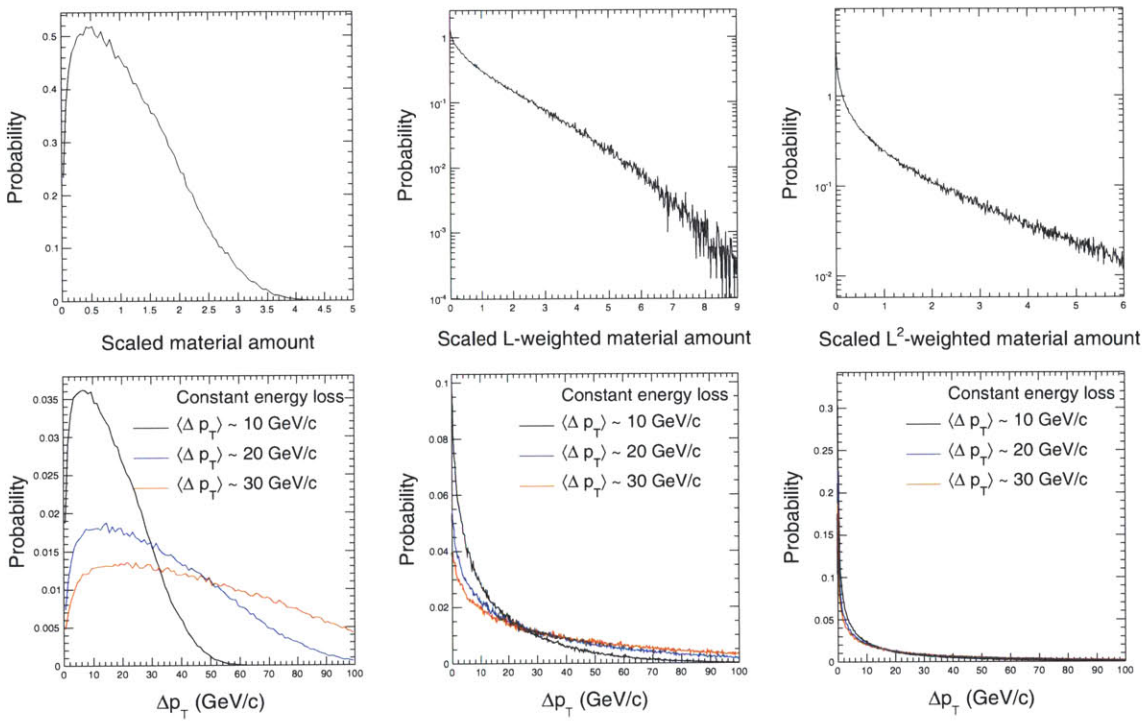

Figure 7-10: Top row shows the scaled projections of material distributions for the two back-to-back parton trajectories. The mean of each distribution is set to 1. The bottom row shows the same distributions, scaled horizontally by a factor representing the average amount of energy-loss in GeV.

Figure 7-11 shows results from the material-proportional energy loss when the material is simply quantified by the number of nucleons (or equivalently, the energy density along the path). This calculation is similar to a density-weighted path-length calculation as in [4]. Such an approach neglects the time-dependence (expansion and flow) of the medium, treating it to be static throughout the motion of the parton.

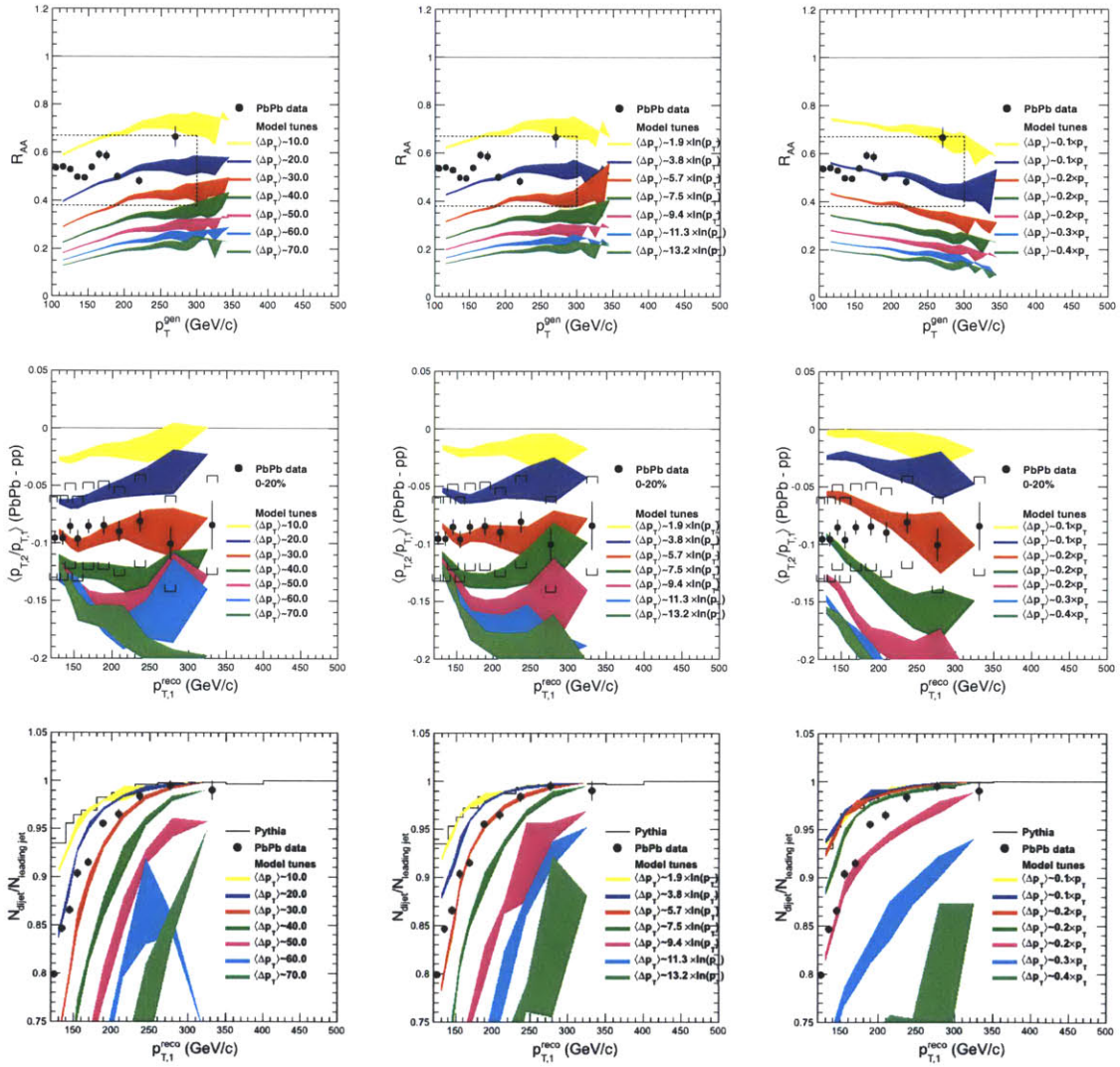

Figure 7-11: Material without distance weighting. The R_{AA} result for PbPb data is interpolated to 0-20% as described in figure 7-2.

In the two other models shown in figures 7-12 and 7-13, the material estimation starts to include a distance dependence with an arbitrary parametrization of L^n. The sum over the nucleons is weighted by L or L^2, where L is the distance between the

target nucleon and the dijet origin. The actual distance effects may correspond to a different L-dependence, however, by understanding the systematic effects introduced by a this variation in the model, we are effectively testing the possible tails introduced to the anti-correlations illustrated earlier in figure 7-9. If such an enhanced anti-correlation is responsible for the observed data, it may also help to adjust the more realistic quenching models.

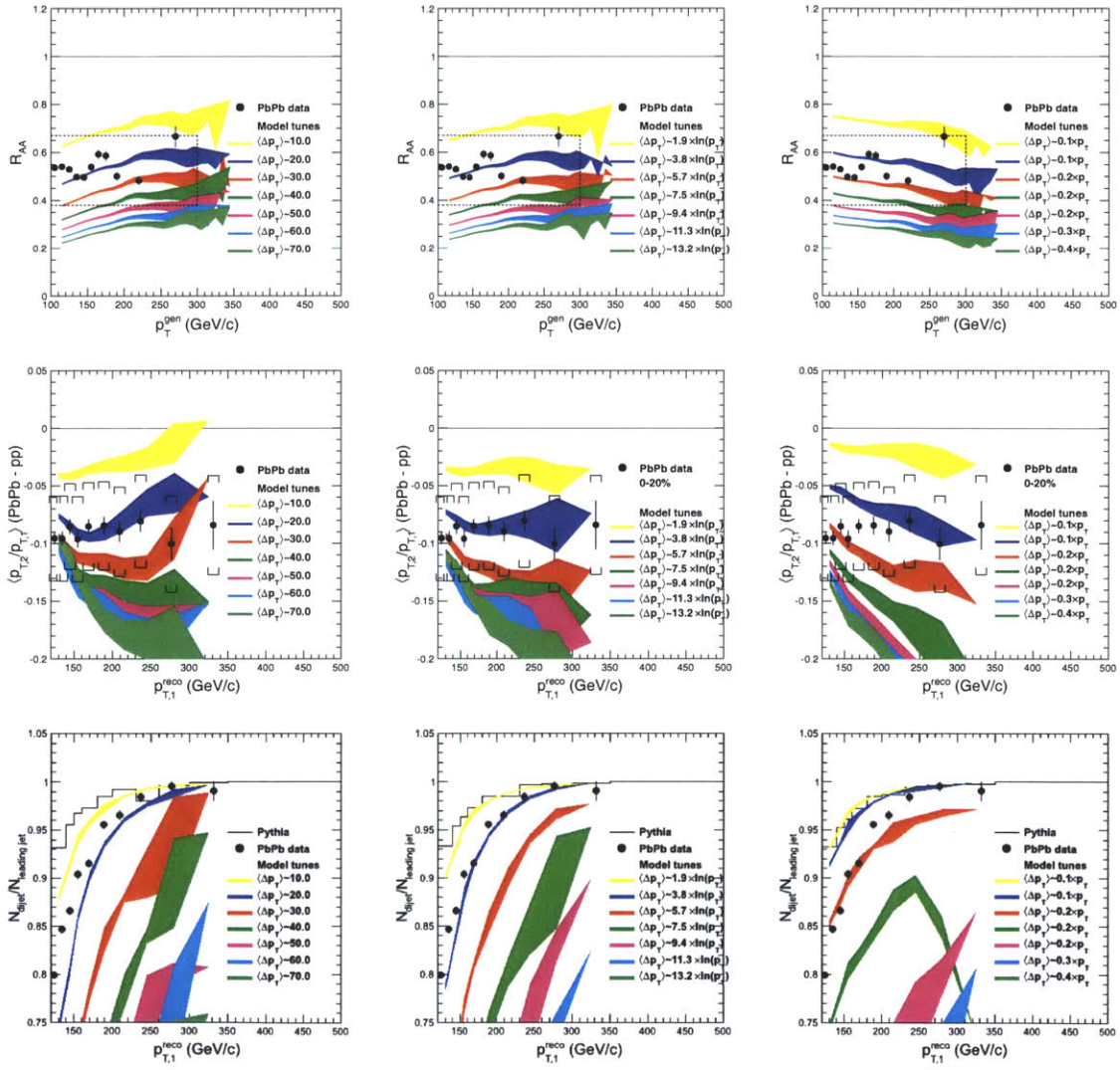

Figure 7-12: L weighted material. The R_{AA} result for PbPb data is interpolated to 0-20% as described in figure 7-2.

In most of the variations of the model, the data is shown to be capable of excluding a large range of medium parameters. One of the models, figure 7-12, succeeds to have

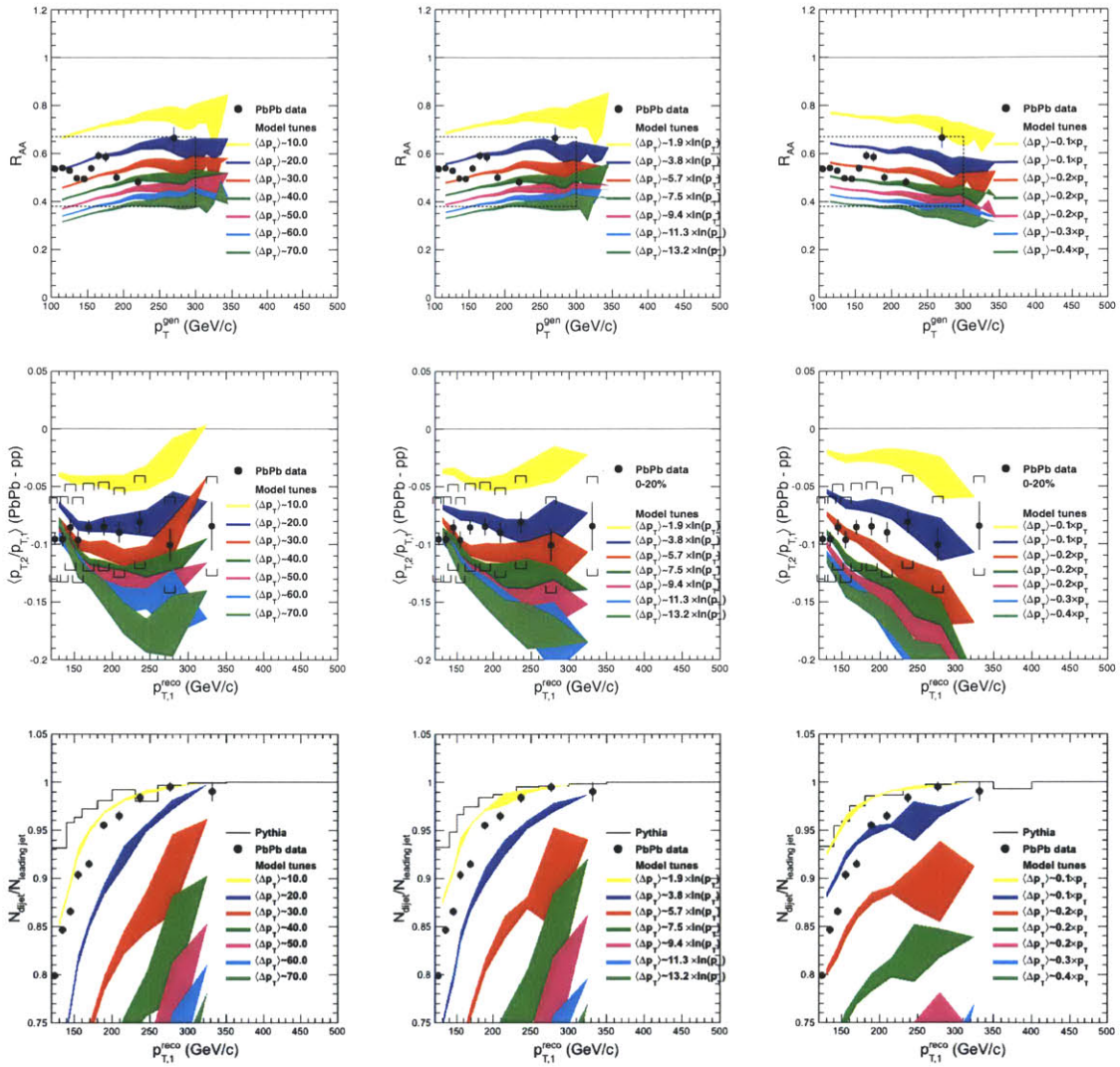

Figure 7-13: L^2 weighted material. The R_{AA} result for PbPb data is interpolated to 0-20% as described in figure 7-2.

a configuration that the results are consistent with data in both the three parts of the measurement. The p_{T}-dependence is not very strongly distinguished when considering the uncertainties in data (although with a hint of a logarithmic, therefore slow, p_{T}-dependence). Here the material is L-weighted, which suggests that the energy-loss correlations may look more like the second panel of figure 7-9. It may be however, a result of a different effect, combined with a different material description, which explains with a similar correlation.

Chapter 8

Conclusions

The data...

The high-energy collisions of heavy nuclei produce a medium that can be studied in the framework of QCD. LHC operations have successfully delivered a large dataset (150 μb^{-1}) of PbPb, along with a dataset (231 nb^{-1}) of pp collisions as reference to the study of medium effects.

We have explored the basic features of dijet events in the PbPb data and simple models. The dijets in PbPb have more imbalanced momenta than in pp, for all selections of leading jet p_T. Accompanying the imbalance, a fraction of subleading jets are lost due to the medium effects. In addition, the energy-loss shifts the jet-p_T spectrum to lower values, resulting in a smaller R_{AA} than unity. These observations combined can probe three parameters of the underlying energy-loss distribution: the mean, variance, and the p_T-dependence.

Dijet imbalance and jet suppression

When an average amount of energy loss is estimated from inclusive jet R_{AA}, one can predict the impact of this energy loss on the imbalance, with the assumption of the energy loss being independent for the two partons. We have shown that such assumption fails to explain inclusive jet R_{AA} and dijet imbalance data simultaneously, and a different mechanism in quenching is needed.

Bjorken had predicted a class of events where the recoil jet gets completely lost [23]. Such events are observed indeed, however, at high enough momentum values, there is never enough energy-loss to absorb the energy completely. The turn-off point for such lost jets helps to constrain model parameters. In addition, the momentum correlations of the observed dijets illustrates the energy-loss more clearly, displaying an enhanced imbalance along the full observed p_{T} range, in excess of 300 GeV/c.

Effects of medium geometry on energy-loss

The amount of enhancement of dijet imbalance, for a certain average energy-loss derived from jet R_{AA}, suggests an anti-correlation of the energy loss between the two jets. Such an anti-correlation can be due to the initial state geometry, making a difference where within the nuclear overlap the hard interaction has occurred. The different geometry models exhibit different energy-loss correlations. These models are tested and shown to be compatible with data on some configurations, in particular with a linear L dependence. The R_{dijet} result, presenting the fraction of matched dijets as a function of p_{T}, is good at constraining the tails of the energy loss distribution, and it excludes some very large values of energy loss for highest-p_{T} jets.

Momentum dependence of quenching

The momentum dependence of the per-length energy-loss appears to be very mild, consistent with most models in theory, however deserves better precision. The fact that the measured momentum itself is subject to energy-loss does not allow the extraction of the average energy-loss value without the model of the full quenching mechanism. Studies of photon-tagged events may probe the initial parton momentum dependence more precisely without this caveat. In addition, better understanding of the jet fragmentation, and geometry-related effects may help constraining the observed momentum dependence.

Measurement of the quenching weights and the path-length dependence

The successful set of models displayed here may be coincidentally returning equivalent results to a combination of effects from a different quenching mechanism in a different medium model. What can be concluded without strong statements on the quenching mechanism or medium evolution is that the dijet imbalance observed has to be explained with anti-correlation of the amount of energy lost by individual partons, and the high energy-loss tails of this anti-correlation are constrained by the data. This may have implications on the medium properties and the amount of material traversed by a parton in more realistic models of expansion. A full-fledged theoretical model should calculate the correlations in the quenching weights, which would be compatible with data if the model results in a similar distribution to middle figure of 7-9.

If the path-length dependence is also modeled realistically, the data may have the capability of differentiating the types of energy-loss. In the simple models discussed above, an emulation of path-length dependence was introduced by an artificial factor of distance, in which case the data was able to distinguish the models by one unit of distance (or time). This factor involves both the dynamics of the energy-loss process, and the medium expansion.

On the experimental side, the extent of relation between quenching and material can be further tested with more detailed study of quenching in relation to the event topology, which can be expected from the LHC experiments in near future.

Bibliography

[1] Siegfried Bethke. Experimental tests of asymptotic freedom. *Prog.Part.Nucl.Phys.*, 58:351–386, 2007.

[2] K Nakamura et al. Review of particle physics. *J. Phys. G*, 37:075021, 2010.

[3] David d'Enterria. *Jet quenching*, volume 23: Relativistic Heavy Ion Physics of *Springer Materials - The Landolt-Börnstein Database*, chapter 6.4. Springer-Verlag, 2010.

[4] Simon Wicks, William Horowitz, Magdalena Djordjevic, and Miklos Gyulassy. Elastic, inelastic, and path length fluctuations in jet tomography. *Nucl.Phys.*, A784:426–442, 2007.

[5] Serguei Chatrchyan et al. Jet momentum dependence of jet quenching in PbPb collisions at $\sqrt{s_{NN}} = 2.76$ TeV. *Phys.Lett.*, B712:176–197, 2012.

[6] Serguei Chatrchyan et al. Measurement of jet fragmentation into charged particles in *pp* and PbPb collisions at $\sqrt{s_{NN}} = 2.76$ TeV. *JHEP*, 1210:087, 2012.

[7] CMS Collaboration. Nuclear modification factor of high transverse momentum jets in pbpb collisions at $\sqrt{s_{NN}}$=2.76 TeV. CMS Physics Analysis Summary CMS-PAS-HIN-12-004, 2012.

[8] Serguei Chatrchyan et al. Studies of jet quenching using isolated-photon+jet correlations in PbPb and *pp* collisions at $\sqrt{s_{NN}} = 2.76$ TeV. *Phys.Lett.*, B718:773–794, 2013.

[9] John Adams et al. Experimental and theoretical challenges in the search for the quark gluon plasma: The STAR collaboration's critical assessment of the evidence from RHIC collisions. *Nucl. Phys. A*, 757:102, 2005.

[10] K. Adcox et al. Formation of dense partonic matter in relativistic nucleus nucleus collisions at RHIC: Experimental evaluation by the PHENIX collaboration. *Nucl. Phys. A*, 757:184, 2005.

[11] I. Arsene et al. Quark-gluon plasma and color glass condensate at RHIC? The perspective from the BRAHMS experiment. *Nucl. Phys. A*, 757:1, 2005.

[12] B. B. Back et al. The PHOBOS perspective on discoveries at RHIC. *Nucl. Phys. A*, 757:28, 2005.

[13] Serguei Chatrchyan et al. Observation and studies of jet quenching in PbPb collisions at nucleon-nucleon center-of-mass energy = 2.76 TeV. *Phys. Rev. C*, 84:024906, 2011.

[14] Georges Aad et al. Observation of a Centrality-Dependent Dijet Asymmetry in Lead-Lead Collisions at sqrt(S(NN))= 2.76 TeV with the ATLAS Detector at the LHC. *Phys. Rev. Lett.*, 105:252303, 2010.

[15] K. Aamodt. Particle-yield modification in jet-like azimuthal di-hadron correlations in Pb-Pb collisions at $\sqrt{s_{NN}} = 2.76$ TeV. Accepted by *Phys. Rev. Lett.*, 2012.

[16] CMS Collaboration. Study of high-pT charged particle suppression in PbPb compared to pp collisions at sqrt(sNN)=2.76 TeV. Submitted to *EPJC*, 2012.

[17] K. Aamodt. Suppression of Charged Particle Production at Large Transverse Momentum in Central Pb–Pb Collisions at $\sqrt{s_{NN}} = 2.76$ TeV. *Phys. Lett. B*, 696:30, 2011.

[18] David J. Gross and Frank Wilczek. Ultraviolet behavior of non-abelian gauge theories. *Phys. Rev. Lett.*, 30:1343–1346, Jun 1973.

[19] D. E. Soper. QCD and Collider Physics. 1997.

[20] W. J. Stirling R. K. Ellis and B. R. Webber. QCD and Collider Physics. 1996.

[21] Andrea Beraudo, Jose Guilherme Milhano, and Urs Achim Wiedemann. Medium-induced color flow softens hadronization. *Phys.Rev.*, C85:031901, 2012.

[22] Urs Achim Wiedemann. Jet Quenching in Heavy Ion Collisions. 2009.

[23] J. D. Bjorken. Energy loss of energetic partons in QGP: possible extinction of high pT jets in hadron-hadron collisions. FERMILAB-PUB-82-059-THY, 1982.

[24] Markus H. Thoma and Miklos Gyulassy. QUARK DAMPING AND ENERGY LOSS IN THE HIGH TEMPERATURE QCD. *Nucl.Phys.*, B351:491–506, 1991.

[25] Eric Braaten and Markus H. Thoma. Energy loss of a heavy quark in the quark-gluon plasma. *Phys. Rev. D*, 44:R2625–R2630, Nov 1991.

[26] L.D. Landau and I.J. Pomeranchuk. *Dokl.Akad.Nauk Ser.Fiz.,92,92.*

[27] Arkady B. Migdal. Bremsstrahlung and pair production in condensed media at high-energies. *Phys.Rev.*, 103:1811–1820, 1956.

[28] Xin-Nian Wang, Miklos Gyulassy, and Michael Plumer. The LPM effect in QCD and radiative energy loss in a quark gluon plasma. *Phys.Rev.*, D51:3436–3446, 1995.

[29] B. G. Zakharov. Fully quantum treatment of the Landau-Pomeranchuk-Migdal effect in QED and QCD. *JETP Lett.*, 63:952–957, 1996.

[30] R. Baier, Yuri L. Dokshitzer, Alfred H. Mueller, S. Peigne, and D. Schiff. Radiative energy loss and p(T) broadening of high-energy partons in nuclei. *Nucl.Phys.*, B484:265–282, 1997.

[31] R. Baier, Yuri L. Dokshitzer, Alfred H. Mueller, and D. Schiff. Medium induced radiative energy loss: Equivalence between the BDMPS and Zakharov formalisms. *Nucl.Phys.*, B531:403–425, 1998.

[32] R. Baier, Yuri L. Dokshitzer, Alfred H. Mueller, and D. Schiff. Radiative energy loss of high-energy partons traversing an expanding QCD plasma. *Phys.Rev.*, C58:1706–1713, 1998.

[33] Carlos A. Salgado and Urs Achim Wiedemann. A Dynamical scaling law for jet tomography. *Phys.Rev.Lett.*, 89:092303, 2002.

[34] A. Dainese, C. Loizides, and G. Paic. Leading-particle suppression in high energy nucleus-nucleus collisions. *Eur.Phys.J.*, C38:461–474, 2005.

[35] M. Asakawa and T. Hatsuda. J/psi and eta_c in the deconfined plasma from lattice qcd. *Phys. Rev. Lett.*, 92:012001, Jan 2004.

[36] Saumen Datta, Frithjof Karsch, Peter Petreczky, and Ines Wetzorke. Behavior of charmonium systems after deconfinement. *Phys. Rev. D*, 69:094507, May 2004.

[37] Jorge Casalderrey-Solana, Hong Liu, David Mateos, Krishna Rajagopal, and Urs Achim Wiedemann. Gauge/String Duality, Hot QCD and Heavy Ion Collisions. 2011.

[38] Edward Witten. Anti-de Sitter space, thermal phase transition, and confinement in gauge theories. *Adv.Theor.Math.Phys.*, 2:505–532, 1998.

[39] Giuseppe Policastro, Dam T. Son, and Andrei O. Starinets. From AdS / CFT correspondence to hydrodynamics. *JHEP*, 0209:043, 2002.

[40] Kengo Maeda, Makoto Natsuume, and Takashi Okamura. Viscosity of gauge theory plasma with a chemical potential from AdS/CFT. *Phys.Rev.*, D73:066013, 2006.

[41] Alex Buchel, James T. Liu, and Andrei O. Starinets. Coupling constant dependence of the shear viscosity in N=4 supersymmetric Yang-Mills theory. *Nucl.Phys.*, B707:56–68, 2005.

[42] Pavel Kovtun, Dam T. Son, and Andrei O. Starinets. Holography and hydrodynamics: Diffusion on stretched horizons. *JHEP*, 0310:064, 2003.

[43] G. Policastro, D.T. Son, and A.O. Starinets. The Shear viscosity of strongly coupled N=4 supersymmetric Yang-Mills plasma. *Phys.Rev.Lett.*, 87:081601, 2001.

[44] Hong Liu, Krishna Rajagopal, and Urs Achim Wiedemann. Calculating the jet quenching parameter from AdS/CFT. *Phys.Rev.Lett.*, 97:182301, 2006.

[45] K.J. Eskola, H. Honkanen, C.A. Salgado, and U.A. Wiedemann. The fragility of high-pt hadron spectra as a hard probe. *Nuclear Physics A*, 747(24):511 – 529, 2005.

[46] B. Alver and G. Roland. Collision geometry fluctuations and triangular flow in heavy-ion collisions. *Phys.Rev.*, C81:054905, 2010.

[47] Thorsten Renk, Hannu Holopainen, Jussi Auvinen, and Kari J. Eskola. Energy Loss in a Fluctuating Hydrodynamical Background. *Phys.Rev.*, C85:044915, 2012.

[48] Enke Wang and Xin-Nian Wang. Jet tomography of dense and nuclear matter. *Phys. Rev. Lett.*, 89:162301, 2002.

[49] CMS Collaboration. CMS physics: Technical Design Report Volume 1: Detector Performance and Software. *CERN-LHCC-2006-001*, 2006.

[50] CMS Collaboration. CMS technical design report, volume II: Physics performance. *J. Phys. G*, 34:995–1579, 2007.

[51] Transverse momentum and pseudorapidity distributions of charged hadrons in pp collisions at sqrt(s) = 0.9 and 2.36 TeV. *JHEP*, 02:041, 2010.

[52] V. Khachatryan et al. Transverse-momentum and pseudorapidity distributions of charged hadrons in pp collisions at $\sqrt{s} = 7$ TeV. *Phys. Rev. Lett.*, 105:022002, 2010.

[53] Torbjorn Sjöstrand, Stephen Mrenna, and Peter Skands. PYTHIA 6.4 Physics and Manual. *JHEP*, 05:026, 2006.

[54] I. P. Lokhtin and A. M. Snigirev. A model of jet quenching in ultrarelativistic heavy ion collisions and high-p_T hadron spectra at RHIC. *Eur. Phys. J. C*, 45:211, 2006.

[55] I. P. Lokhtin. Hydjet event generator. *http://lokhtin.web.cern.ch/lokhtin/hydro/hydjet.html* , 2011.

[56] S. Agostinelli et al. GEANT4–a simulation toolkit. *Nucl. Instrum. and Methods A*, 506:250, 2003.

[57] Matteo Cacciari, Gavin P. Salam, and Gregory Soyez. FastJet User Manual. *Eur.Phys.J.*, C72:1896, 2012.

[58] Matteo Cacciari and Gavin P. Salam. Dispelling the N^3 myth for the k_t jet-finder. *Phys.Lett.*, B641:57–61, 2006.

[59] Matteo Cacciari, Gavin P. Salam, and Gregory Soyez. The anti-k_t jet clustering algorithm. *JHEP*, 04:063, 2008.

[60] Serguei Chatrchyan et al. Determination of Jet Energy Calibration and Transverse Momentum Resolution in CMS. *JINST*, 06:P11002, 2011.

[61] Serguei Chatrchyan et al. Observation of a new boson at a mass of 125 GeV with the CMS experiment at the LHC. *Phys.Lett.*, B716:30–61, 2012.

[62] Serguei Chatrchyan et al. Dependence on pseudorapidity and centrality of charged hadron production in PbPb collisions at a nucleon-nucleon centre-of-mass energy of 2.76 TeV. *JHEP*, 1108:141, 2011.

[63] Serguei Chatrchyan et al. Measurement of the pseudorapidity and centrality dependence of the transverse energy density in PbPb collisions at $\sqrt{s_{NN}} = 2.76$ TeV. *Phys.Rev.Lett.*, 109:152303, 2012.

[64] Serguei Chatrchyan et al. Centrality dependence of dihadron correlations and azimuthal anisotropy harmonics in PbPb collisions at $\sqrt{s_{NN}} = 2.76$ TeV. *Eur.Phys.J.*, C72:2012, 2012.

[65] Serguei Chatrchyan et al. Measurement of the azimuthal anisotropy of neutral pions in PbPb collisions at $\sqrt{s_{NN}} = 2.76$ TeV. *Phys.Rev.Lett.*, 2012.

[66] Serguei Chatrchyan et al. Measurement of the elliptic anisotropy of charged particles produced in PbPb collisions at nucleon-nucleon center-of-mass energy = 2.76 TeV. *Phys.Rev.*, C87:014902, 2013.

[67] B. Alver, M. Baker, C. Loizides, and P. Steinberg. The PHOBOS Glauber Monte Carlo. 2008.

[68] Michael L. Miller, Klaus Reygers, Stephen J. Sanders, and Peter Steinberg. Glauber modeling in high energy nuclear collisions. *Ann. Rev. Nucl. Part. Sci.*, 57:205, 2007.

[69] CMS Collaboration. Identification and filtering of uncharacteristic noise in the CMS hadron calorimeter. *JINST*, 05:T03014, 2010.

[70] J. Casalderrey-Solana, J.G. Milhano, and U. Wiedemann. Jet quenching via jet collimation. *J. Phys. G*, 38:124086, 2011.

[71] ATLAS Collaboration. Observation of a Centrality-Dependent Dijet Asymmetry in Lead-Lead Collisions at $\sqrt{s_{NN}}$= 2.76 TeV with the ATLAS Detector at the LHC. *Phys. Rev. Lett.*, 105:252303, 2010.

[72] Nestor Armesto, Brian Cole, Charles Gale, William A. Horowitz, Peter Jacobs, et al. Comparison of Jet Quenching Formalisms for a Quark-Gluon Plasma 'Brick'. 2011.

[73] Leo Zhou and George S. F. Stephans (private communication).